Analysis of flow-induced performance change of cycloidal rotors: Influence of pitching kinematic and chord-to-radius ratio

Lei Shi, Annie-Claude Bayeul-Lainé, Olivier Coutier-Delgosha

Analysis of flow-induced performance change of cycloidal rotors: Influence of pitching kinematic and chord-to-radius ratio

Lei Shi[1], Annie-Claude Bayeul-Lainé[1], Olivier Coutier-Delgosha[1,2, a)]

[1]Univ. Lille, CNRS, ONERA, Arts et Métiers ParisTech, Centrale Lille, UMR 9014 - LMFL - Laboratoire de Mécanique des Fluides de Lille - Kampé de Feriet, F-59000 Lille, France

[2]Kevin T. Crofton Department of Aerospace and Ocean Engineering, Virginia Tech, Blacksburg, VA 24060, USA

[a)]Author to whom correspondence should be addressed: Olivier.coutier-delgosha@ensam.eu

Abstract

As a new-type propulsive system, cycloidal rotor has been attracting more attention recently. The present work concentrates on the analysis of the performance and internal flow field of a two-bladed cycloidal rotor operating at low Reynolds numbers, with special emphasis on understanding how the flow structure affects the performance at different working conditions. The symmetrical/asymmetrical pitching motions are evaluated initially and the primary results show that the asymmetrical pitching with a mean pitch angle of 5° improves the efficiency of the rotating system. Then, the effect of the chord-to-radius ratio at three different conditions is discussed, which shows that the chord-to-radius ratio of 0.45 is the best value to maximise the performance. The flow pattern, involving the blade-wake interaction, wake-wake interaction, three-vortex-structure on the blade surface, roll-up vortices inside the laminar boundary layer, laminar separation bubble, leading-edge vortex, trailing-edge vortex and flow separation vortex, are discussed in detail for various operating conditions. The study of the performance of a single blade, the forces (lift and drag) distributions, the blade loadings and the near-wall flows on two blades, provide a new understanding of the global performance of the propeller.

Keywords: Cycloidal rotor; Low Reynolds number flow; Pitching kinematic; Chord-to-radius ratio

1. Introduction

Cycloidal motions of blades have a variety of applications to the engineering equipment, such as vertical-axis wind turbines (VAWT), underwater propulsion systems, marine power generation turbines, and micro air vehicles (MAV). The cycloidal propeller is made up of several vertical blades, which combine two motions, namely the rotation around the shaft center and the oscillating motion around a pivot located along the blade chord line. In a rotating cycle, the forces (lift F_L and drag F_D) acting on the blade surface change continuously, whose components in the vertical and horizontal directions provide the lift and propulsive force to the cycloidal propeller, as shown in figure 1. In addition, each blade experiences successively retreating and advancing sides, in which the resultant blade loading and flow structures are extremely different. Some previous works show the complicated internal flows inside a cycloidal propeller [1-2], such as massive flow separation, laminar-turbulence transition, blade-wake and wake-wake interactions, which have a great effect on the performance of the rotating system and every single blade. Thus, it is necessary to have a deep understanding of the flow physics of the cycloidal propeller under various operating conditions.

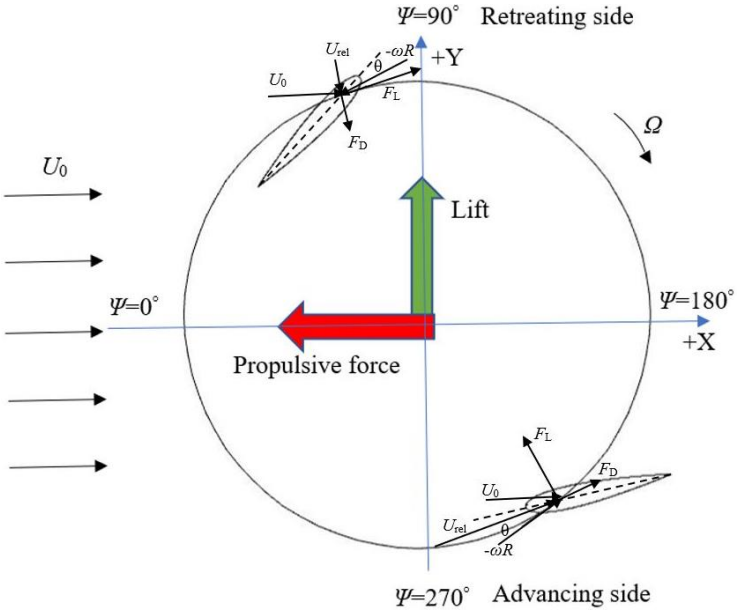

Fig.1 Cycloidal rotor system.

Recently, optimizations of vertical-axis turbines and propellers considering the modifications of geometrical parameters have been conducted numerically and experimentally [3-4]. For a better design of the high-performance cycloidal propeller, several factors are usually considered in these studies, e.g. the chord-to-radius ratio (c/R), the solidity (σ), the blade profile, the pitch-pivot-point location (x/c), the pitching kinematic (symmetrical or asymmetrical pitching) and the blade shape (for three-dimensional flows), are usually taken into consideration. The blade pitching

kinematic is one of the most important parameters, since it has a great impact on the instantaneous blade forces and aerodynamic performance. In the aforementioned works, the cycloidal propeller often operates with symmetrical sinusoidal pitching, which means that each blade has the same pitching angles as it comes across the retreating and advancing sides [5-6]. However, the symmetrical pitching may not lead to the optimal performance, especially in the forward flight. Benedict et al. [4] used computational fluid dynamics (CFD) to investigate the internal flows of a four-bladed cyclorotor and found that the instantaneous blade forces are non-uniform along the rotor in forward flight. Such non-uniform forces may limit the overall performance of the cycloidal rotor system. Then, Benedict et al. [7] performed some experiments to understand the role of the rotor geometry and blade pitching kinematic on the performance of a cycloidal rotor in hover. The results show that higher pitching amplitudes can improve the power loading (thrust per unit power), with an optimal performance obtained at 40 deg. Simultaneously, the asymmetrical pitching with a higher pitch angle at the top of the circular trajectory than that at the bottom produces a better power loading. Walther et al. [8] employed both CFD and particle image velocimetry (PIV) measurements to show the advantage of asymmetrical pitching with higher pitch in the upper half and low pitch in the bottom half. They show that it improves the efficiency of the cycloidal propeller, due to the inherent asymmetrical lift distributions along the blade. Except the reduction of power consumption related to the more uniform azimuthal distribution of blade forces provided by the asymmetrical pitching, Benedict et al. [9] also found that highly unsteady flow features, due to blade-wake and wake-wake interactions, can be alleviated by using the asymmetrical pitching. Additionally, some energy equipment handing liquids also use the variable-pitch blades with asymmetrical pitching and the resultant hydrodynamic performances are enhanced remarkably [10-11].

The chord-to-radius ratio is also a critical parameter to the optimum performance of the cycloidal propeller, but it was seldom investigated previously. Although Hu et al. [12] stated that a moderate chord length is more appropriate for a better performance of the cycloidal propeller, no impact of the rotating radius was reported. However, an increase of R should be beneficial to the efficiency of the system, because of less interaction with vortices shed from the blades. In addition, Xisto et al. [13] employed CFD to study the influence of various parameters on the performance of a variable-pitch VAWT, and observed that a higher torque is obtained at a very low tip speed ratio with larger blade, but the torque decreases significantly with the increase of the tip speed ratio. However, in this study, the chord-to-radius ratio varies by changing the blade chord length only, and the influence of rotating radius is not considered. Optimizing the value of c/R is of importance to improve the

global performance, since this ratio has some influence on the virtual camber/incidence [7], which is an aerodynamic phenomenon found in VAWT blades where the blades undergo an orbital motion and thus experience a curvilinear flow. For a fixed total lift, the lift producing efficiency (lift per unit power) of a cycloidal rotor increases with c/R until the value of 0.67, but the optimum value of c/R for maximal thrust per unit power decreases from 0.67 to 0.55 when the forward speed is increased from 5 to 9m/s, as reported in reference [4]. Then, Benedict et al. [7] clarified that the power loading of the cyclorotor is strongly dependent on c/R and the higher power loading is achieved by the higher c/R. They also conclude that the optimum c/R is around 0.5-0.8, depending on the blade pitching amplitude.

Motivated by the studies mentioned above, the goal of this work is to study the influence of two important parameters, namely the pitching kinematic and the chord-to-radius ratio, on the performance of a two-bladed cycloidal rotor, with special emphasis on the performance variation induced by the flow structures under various conditions. Therefore, various symmetrical/asymmetrical pitching kinematics and values of chord-to-radius ratio are studied in the present work. It believes that analyzing in detail the flow structures at different operating conditions can provide some design recommendations for cycloidal propellers eventually.

2. Numerical setup

2.1 Propeller geometry and operating conditions

The cycloidal propeller consists of two blades with NACA0015 profile. The lift and propulsive force are produced in vertical and horizontal directions, respectively, due to the continuous change of the relative incidence. The initial azimuthal angle ψ starts from the negative X axis along the clockwise direction, while the phase angle Φ changes from the positive Y axis in anti-clockwise direction, which is shown in figure 1. For the symmetrical pitching kinematic, the mean pitch angle θ_0 is equal to 0° and the pitching amplitude θ_A is changed. However, the mean pitch angle θ_0 also varies to investigate the asymmetrical effect of the pitching kinematic. A sketch of relative incidences and forces of two blades with a symmetrical pitching and an asymmetrical pitching are shown in figure 2. The symmetrical pitching means that the blade at $\psi=0^\circ$ and 180° has the same magnitude of the angle-of-attack, while the values of the incidence at these two positions are different for the asymmetrical pitching, as presented in figure 2c (0°-15° indicates the combination of the mean pitch angle and pitching amplitude). Obviously, in figure 2a and 2b, when the blade moves with different pitching kinematics, the forces on two blades are totally different, leading to the different flow structures and blade loadings. The influence of the Reynolds number is studied by modifying the rotation speed and inlet velocity at the

same time, while only the rotation speed is changed to clarify the effect of the advance coefficient λ. With the consideration of both two parameters, involving the blade chord length c and rotating radius R, the rotating speed and rotor radius vary simultaneously, to discuss the impact of c/R for different blade chord lengths. The information about the geometry of the cycloidal propeller and the working conditions are listed in Table 1.

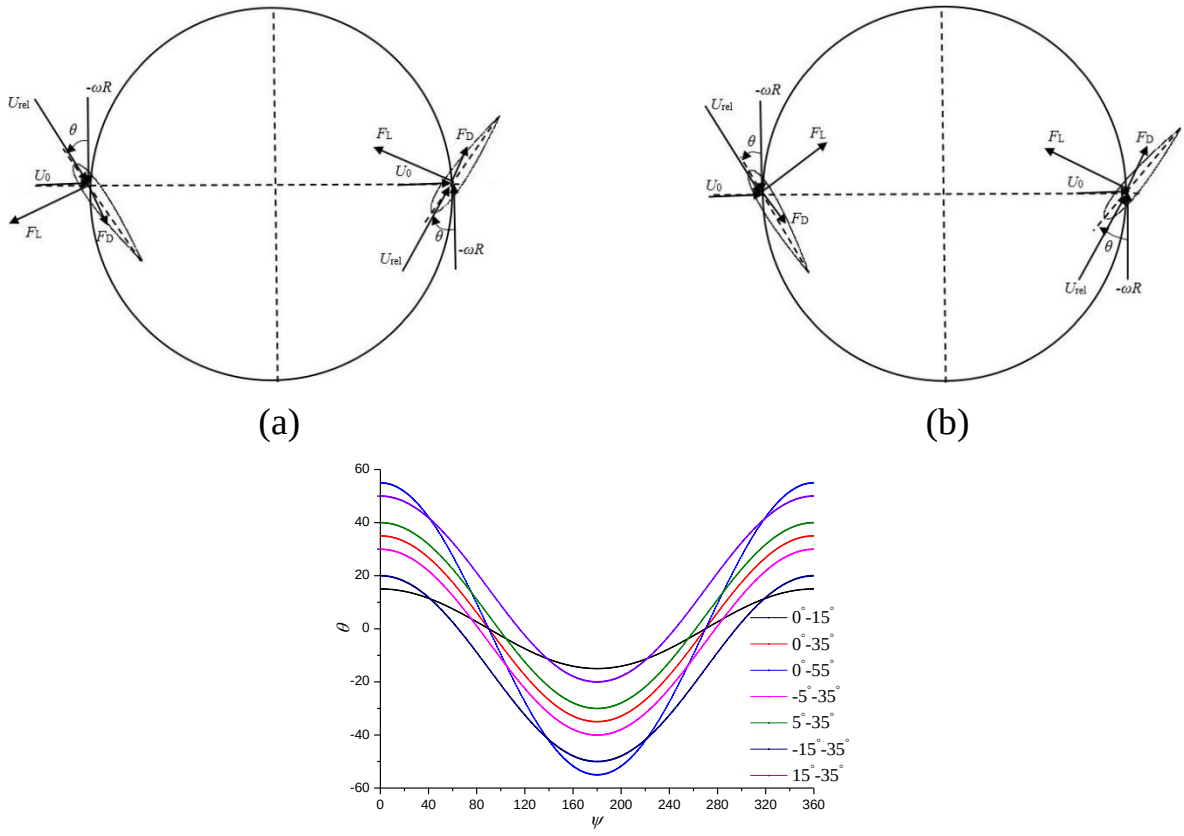

Fig.2 Force sketch and relative incidences. (a) θ=35°sin(ψ+π/2); (b) θ=-5°+35°sin(ψ+π/2); (c) Different pitching kinematics.

Table 1 Main geometrical parameters and working conditions.

Blade profile	NACA0015
Blade number (N_b)	2
Inlet velocity (U_0 (m/s))	3-11
Chord-to-radius ratio (c/R)	0.29-1.12
Pitch-pivot-point (x/c)	25%
Mean pitch angle (θ_0 (°))	$\theta=\theta_0+\theta_A\sin(\psi+\Phi)$ (-15, -10, -5, 5, 10, 15)
Pitching amplitude (θ_A (°))	15, 25, 35,45, 55
Rotating speed (n (r/min))	600-3960
Advanced coefficient (λ)	$\lambda=U_0/\omega R$ (0.33-0.75)
Reynolds number (Re)	$Re=\sqrt{U_0^2+(\omega R)^2}c/\nu$ (1.47×10^4-5.41×10^4)

2.2 Turbulence modelling

The SST $\gamma - \widetilde{Re}_{\theta t}$ four-equation transition model, is adopted here to account for laminar-turbulence transition, as the propeller considered in this work is operating at quite low Reynolds number. The original SST k-ω model combines two basic turbulence models, k-ε model predicting the free-stream flows and k-ω model that is applied to the near-wall flows. The superiority of SST k-ω model is the ability to achieve a good behaviour in adverse pressure gradient and separating flows [14-15]. Two additional transport equations, for the intermittency γ and the transition onset momentum thickness Reynolds number $\widetilde{Re}_{\theta t}$, were included by Menter et al. [16-17], to trigger the onset of flow-separation induced transition. The formulation of this four-equation turbulence model is given by:

$$\frac{\partial}{\partial t}(\rho k) + \frac{\partial}{\partial x_j}\left(\rho u_j k\right) = P_k - D_k + \frac{\partial}{\partial x_j}\left((\mu + \sigma_k \mu_t)\frac{\partial k}{\partial x_j}\right) \tag{1}$$

$$\frac{\partial}{\partial t}(\rho \omega) + \frac{\partial}{\partial x_j}\left(\rho u_j \omega\right) = \alpha \frac{P_k}{\nu_t} - D_\omega + 2(1 - F_1)\frac{\sigma_{\omega 2}}{\omega}\frac{\partial k}{\partial x_j}\frac{\partial \omega}{\partial x_j} + \frac{\partial}{\partial x_j}\left((\mu + \sigma_\omega \mu_t)\frac{\partial \omega}{\partial x_j}\right) \tag{2}$$

$$\mu_t = \frac{a_1 k \rho}{\max(a_1 \omega, SF_2)} \tag{3}$$

$$\frac{\partial}{\partial t}(\rho \gamma) + \frac{\partial}{\partial x_j}\left(\rho u_j \gamma\right) = P_\gamma - E_\gamma + \frac{\partial}{\partial x_j}\left(\left(\mu + \frac{\mu_t}{\sigma_f}\right)\frac{\partial \gamma}{\partial x_j}\right) \tag{4}$$

$$\frac{\partial}{\partial t}\left(\rho \widetilde{Re}_{\theta t}\right) + \frac{\partial}{\partial x_j}\left(\rho u_j \widetilde{Re}_{\theta t}\right) = P_{\theta t} + \frac{\partial}{\partial x_j}\left(\sigma_{\theta t}(\mu + \mu_t)\frac{\partial \widetilde{Re}_{\theta t}}{\partial x_j}\right) \tag{5}$$

Then, the effective intermittency γ_{eff} is used to modify the production and destruction terms in k equation, which is shown as follows

$$\tilde{P}_k = \gamma_{eff} P_k;\ \tilde{D}_k = min\left(max\left(\gamma_{eff}, 0.1\right), 1.0\right) D_k \tag{6}$$

where ρ is the density of the working fluid, k is the turbulent kinematic energy, ω is the turbulence specific dissipation rate, P_k and D_k are the production and destruction terms in k equation, D_ω is the destruction term in ω equation, μ_t is the turbulence dynamic viscosity, F_1 and F_2 are two functions related to the distance to the wall, S is the shear strain rate. In the transition model, P_γ and E_γ are the production and destruction terms in γ equation, while $P_{\theta t}$ is the production term in $\widetilde{Re}_{\theta t}$ equation. The detailed correlations and magnitudes of some constants can be found in references [14, 16-17]. This model is quite robust because the intermittency has no direct relationship with the momentum equations. Additionally, it has already been applied to many engineering flows successfully [18-20].

2.3 *Computational configuration and meshing*

From the propeller rotating center, the two-dimensional rectangular computational domain extends 10*c* upstream and 30*c* downstream, where *c* is the chord length. The distance from the rotating center to the top and bottom walls is 10*c*. In figure 3, a hybrid mesh is used, involving trimmed cells in the free-stream region and prism layer cells near the wall. The sliding mesh method is employed to connect four different sub-domains, namely (i) two small rotating circles (SRC) that contain the blades and rotate according to each blade movement; (ii) a large circle (LRC) that rotates at the rotation speed of the propeller; (iii) the external domain. The mesh is refined in the three rotating parts and in the wake region to capture the details of the unsteady vortical flows. Furthermore, to capture the transition accurately, the meshes near the two blade surfaces are also refined along the streamwise direction. The total number of cells is close to 0.7 million. Some more details about the mesh are given in Table 2. The influence of the mesh resolution on the numerical results was discussed in our previous work [21] in the same configuration and the present setup was eventually validated, so it is used hereafter in the present paper.

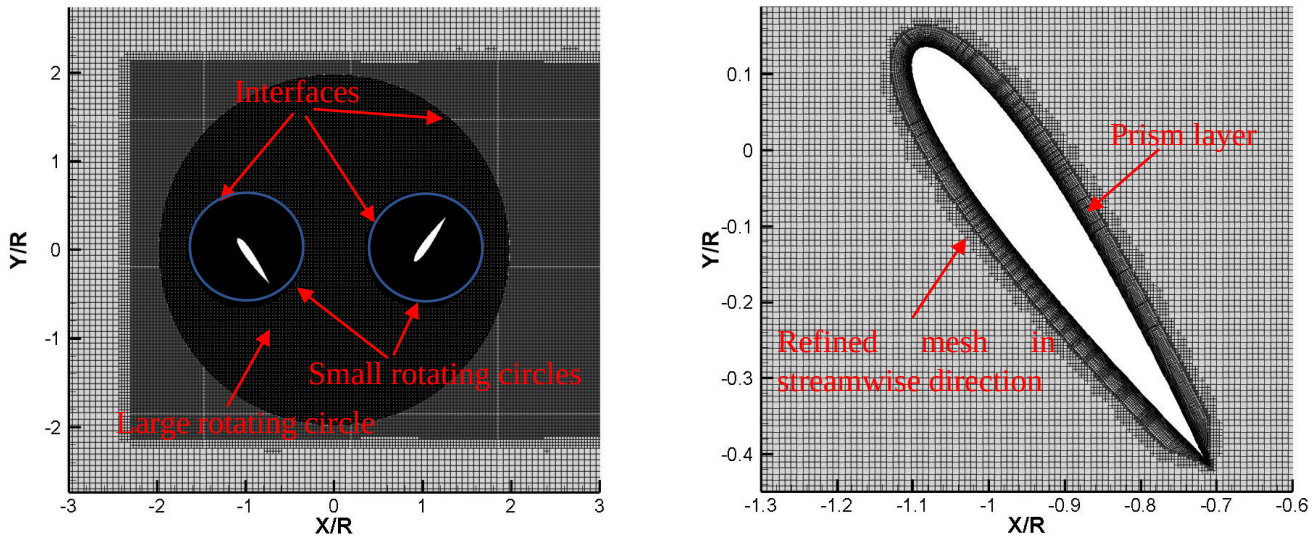

(a) (b)

Fig.3 Mesh distribution. (a) Computational domain; (b) Mesh near the airfoil surface.

Table 2 Information of the mesh distribution

Target size of the mesh in LRC (m)	Minimum size of the mesh in LRC (m)	Target size of the mesh in SRC (m)	Minimum size of the mesh in SRC (m)	Distance of the first layer to the wall (m)	Number of the prism layer	Thickness of the prism layer (m)
6×10^{-7}	6×10^{-7}	2×10^{-7}	2×10^{-7}	3.4×10^{-8}	65	2×10^{-3}

2.4 Numerical Setup

The computations are performed with the code STARCCM +, which is based on the finite volume method to calculate the transport of the physical quantities on a discretized mesh. For the boundary conditions, a constant inlet velocity and a fixed outlet pressure are applied. The top and bottom walls are set as symmetrical planes to avoid any wall effect. A no-slip wall condition is applied to the airfoil surface. The all y^+ wall treatment is used, and the maximal y^+ does not exceed 0.5 at any position in a revolution. The influence of the time-step, the level of convergence, and the inlet boundary conditions (turbulence intensity and eddy viscosity ratio), were discussed in our previous work [21] and the conclusions are used here to select these different parameters.

3. Results and discussion

3.1 Influence of the pitching kinematic

The asymmetrical pitching is tested by changing the mean pitch angle θ_0, and the results are compared to the ones obtained with symmetrical pitching kinematics. When the blades operate with symmetrical pitching, the effects of inlet velocity and rotating speed are presented firstly by plotting the performance curves in figure 4, including the time-averaged lift, propulsive force, and power coefficients, as well as the calculated efficiency. In these test cases, the blade chord length is 0.0495m and the chord-to-radius ratio is 0.65. The pitching amplitude is kept constant and equal to 35°. The non-dimensional lift, propulsive force, power coefficients and efficiency are defined as follows: $C_L = \frac{F_L}{0.5*\rho*U_0^2*c}$, $C_{PF} = \frac{F_{PF}}{0.5*\rho*U_0^2*c}$, $C_{Power} = \frac{P}{0.5*\rho*U_0^3*c}$ and $\eta = \frac{F_{PF}*U_0}{P}$ (where F_L is the lift, F_{PF} is the propulsive force and P is the power). With the increase of λ at constant inlet velocity, the lift, propulsive force and power coefficients decrease significantly, and the efficiency slightly improves initially and then completely drops, which means that the combination of inlet velocity and rotation speed is crucial to obtain an optimized performance. When λ varies from 0.47 to 0.56 by increasing both the inlet velocity and the rotating speed, the efficiency of the cycloidal rotor system improves remarkably, from 28.82% to 41.63%. In addition, at low inlet velocity, although the propulsive force at low advance coefficient is large, the efficiency is still relatively low because of the large power required. Simultaneously, it is also observed that the lift coefficient has some difference under small λ condition, especially for the cases with low inlet velocity. Six points at the best efficiency, including λ=0.47 for U_0=3m/s, λ=0.50 for U_0=4m/s, λ=0.52 for U_0=5m/s, λ=0.54 for U_0=6m/s, λ=0.55 for U_0=7m/s and λ=0.56 for

U_0=8m/s, are selected to study the influence of the pitching kinematic on the performance of the propeller and the flow structures around the blades.

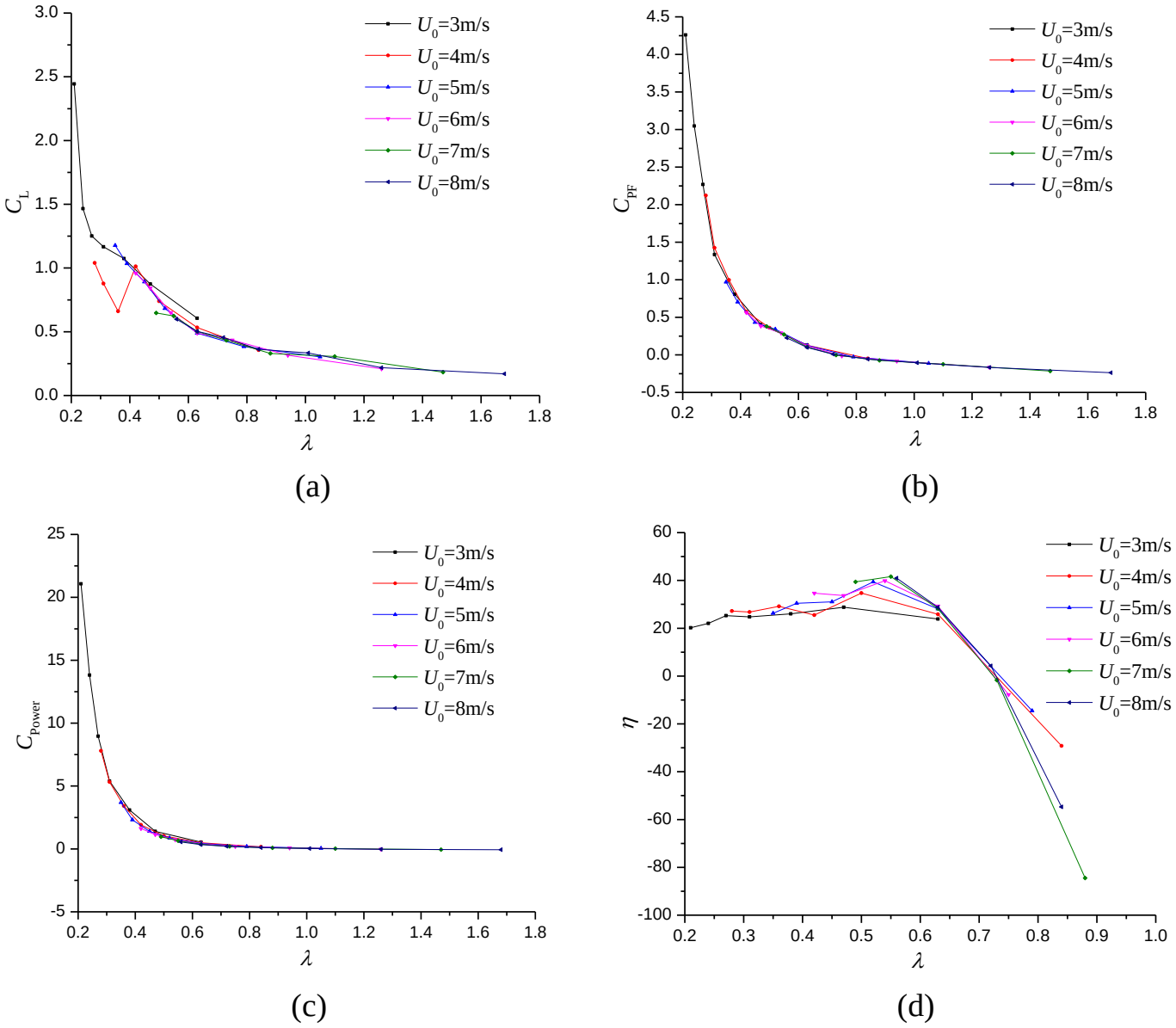

Fig.4 Performance curves at different λ. (a) Lift coefficient; (b) Propulsive force coefficient; (c) Power coefficient; (d) Efficiency.

The distributions of spanwise vorticity obtained in cases of symmetrical and asymmetrical pitching kinematics are displayed in figure 5 at ψ=0°. The asymmetrical pitching is controlled by changing the mean pitch angle, and the pitching amplitude remains unchanged with a value of 35°. The inlet velocity is U_0=5m/s, and the corresponding advance coefficient is 0.52. For the symmetrical pitching, when the pitching amplitude is increased (figures 5a to 5c), vortices shed in the wake of blade A have a stronger interaction with blade B. Additionally, at a pitching amplitude of 15°, it is clear that wake B interacts with wake A. At high pitching amplitude, there is also an interaction between blade B and wake B, which indicates that there is a

transition from wake A-wake B to wake B-blade B, and finally wake A-blade B interactions. Besides, the massive flow separation is visible on the left side of blade A when the pitching amplitude is 55°, which certainly greatly impacts the blade loading. When the mean pitch angle is equal to 5° (the amplitude being the same), the global flow pattern remains similar (see figures 5b and 5d), but the flow starts to separate at the leading edge of blade A, on its left side. With a mean pitch angle of -5°, blade B has a large risk of interaction with the vortices shed in the wake of blade A. Moreover, on the right side of blade A, there is a substantial flow separation. Finally, as the mean pitch angle increases to 15° or -15°, wake A is more likely to interact with blade B and there is also an obvious interaction between the leading edge and the trail vortices of blade B. Globally, the flow structures over the two blades are much different in these different configurations. For example, some flow separation is detected on the left side of blade A in figure 5f, while it is on the right side of the blade in figure 5g, where it also occurs on blade B. Thus, it can be concluded that the complicated flow field within a cycloidal rotor, involving different kinds of blade-wake, wake-wake interactions and massive flow separation over the two blades, depends considerably on the pitching kinematics, especially for the symmetrical pitching with large amplitude and asymmetrical pitching with large mean pitch angle.

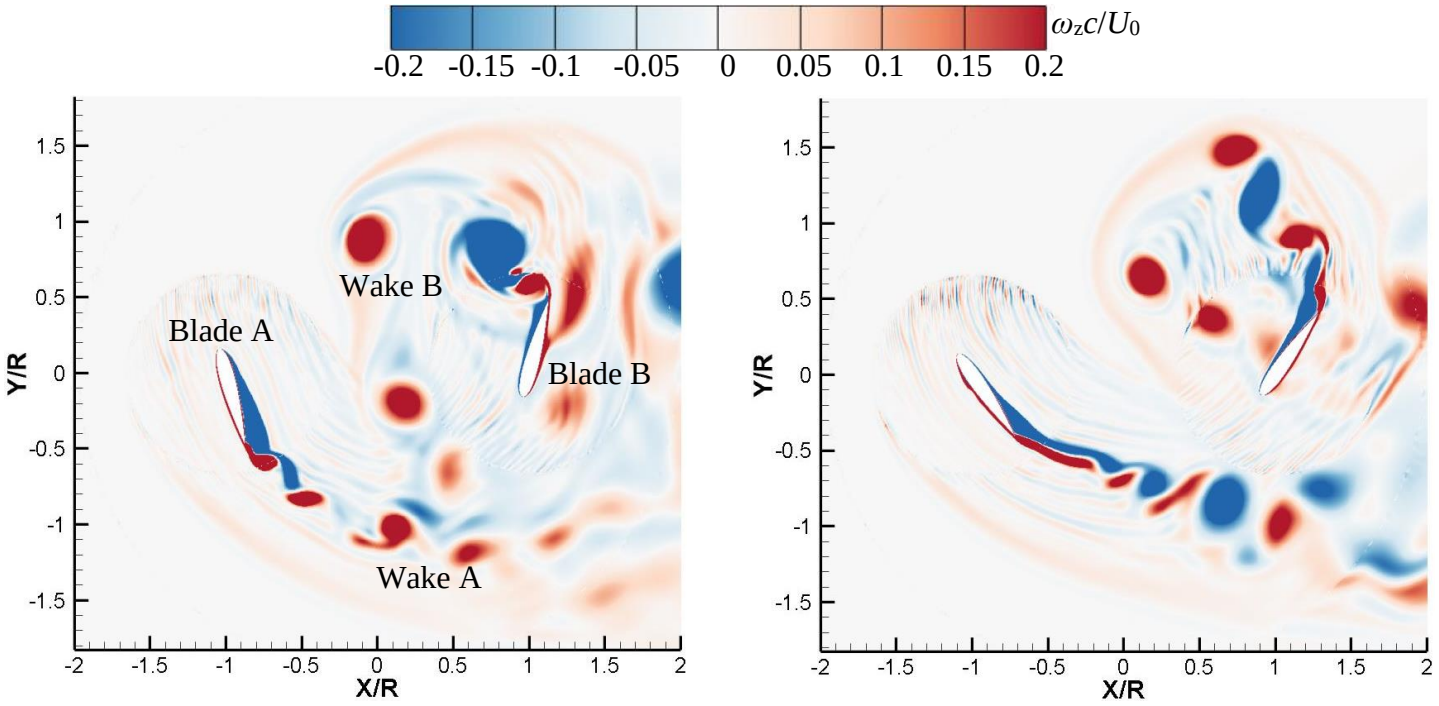

(a) (b)

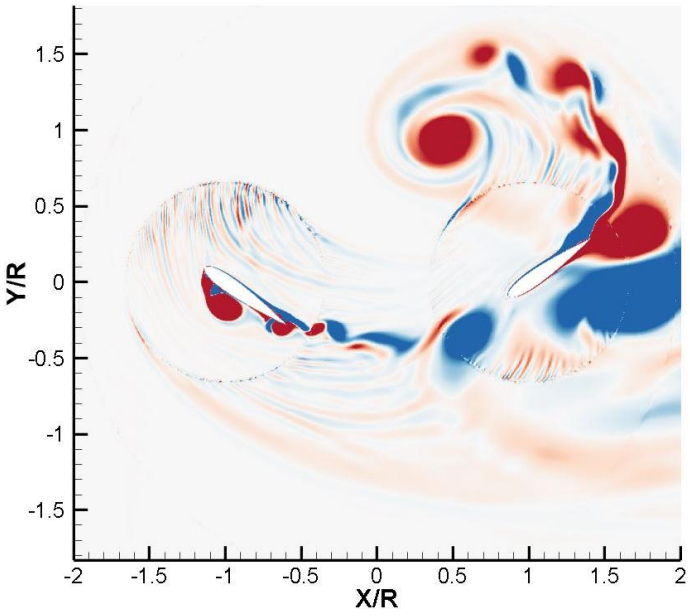
Y/R
X/R
1.5
1
0.5
0
-0.5
-1
-1.5
-2
-1.5
-1
-0.5
0
0.5
1
1.5
2

(c)

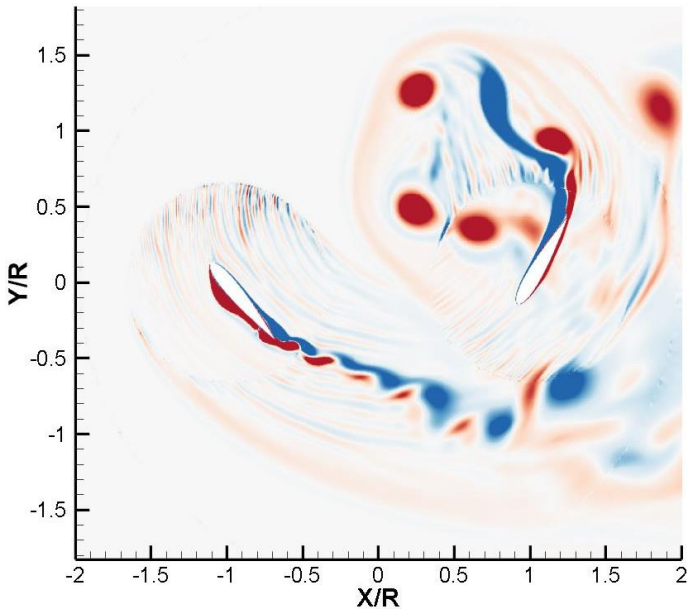
Y/R
X/R
1.5
1
0.5
0
-0.5
-1
-1.5
-2
-1.5
-1
-0.5
0
0.5
1
1.5
2

(d)

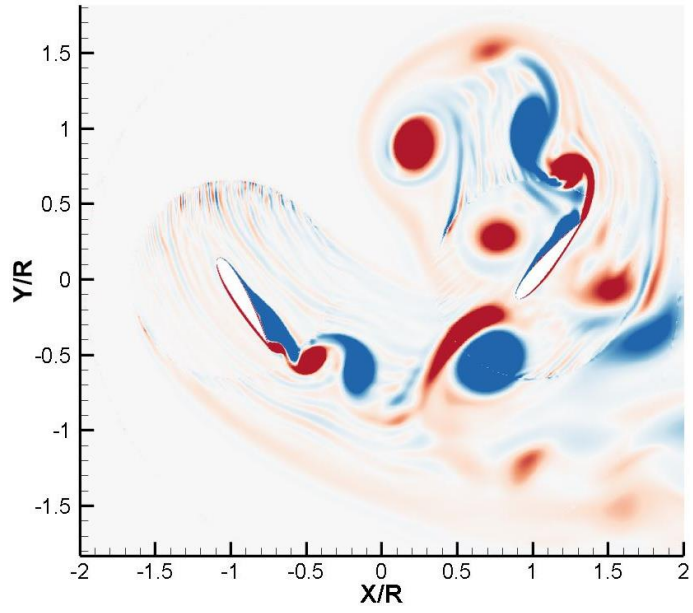
Y/R
X/R
1.5
1
0.5
0
-0.5
-1
-1.5
-2
-1.5
-1
-0.5
0
0.5
1
1.5
2

(e)

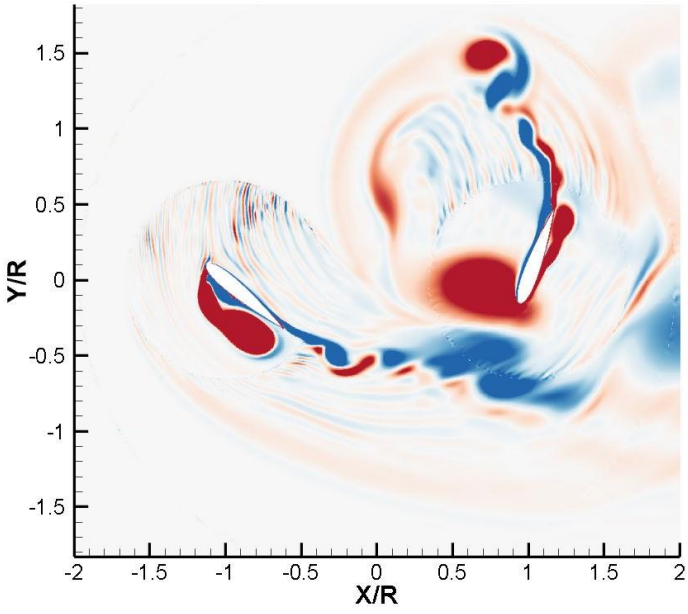
Y/R
X/R
1.5
1
0.5
0
-0.5
-1
-1.5
-2
-1.5
-1
-0.5
0
0.5
1
1.5
2

(f)

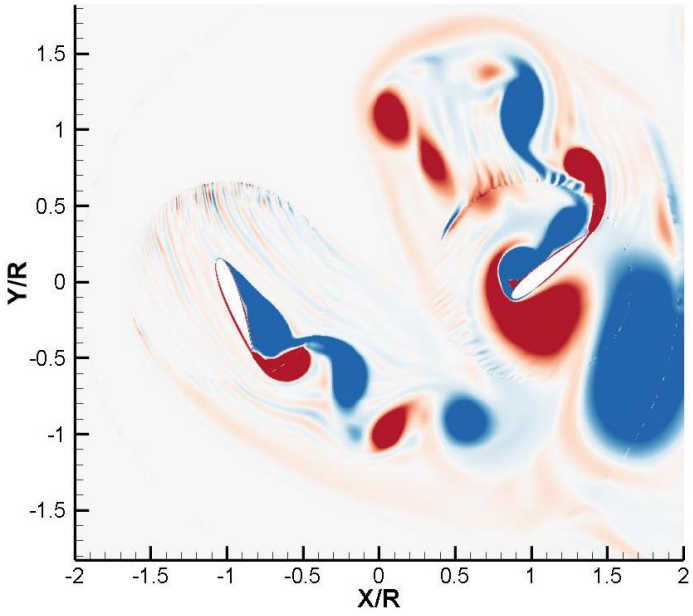

(g)

Fig.5 Flow structures for different pitching kinematics. (a) θ=15°sin(ψ+π/2); (b) θ=35° sin(ψ+π/2); (c) θ=55°sin(ψ+π/2); (d) θ=5°+35°sin(ψ+π/2); (e) θ=-5°+35°sin(ψ+π/2); (f) θ=15° +35° sin(ψ+π/2); (g) θ=-15°+35°sin(ψ+π/2).

In figure 6, the performance curves are plotted at the best efficiency conditions shown in figure 4d, for different pitching kinematics. For the symmetrical pitching, the lift coefficient exhibits no significant change at different λ when the pitching amplitude does not exceed the value of 35°. For the pitching amplitude between 35° and 55°, the lift coefficient increases dramatically when λ is larger than 0.5. When the mean pitch angle is negative, the lift coefficient has an evident increase, while the trend is opposite in cases with the positive mean pitch angle. It can be observed that the symmetrical pitching with amplitudes of 45° and 55° produce the largest propulsive force coefficient, which increases significantly with λ. Conversely, pitching amplitudes lower than 25° generate the lowest propulsive force coefficient, which even decrease more at large λ. At fixed amplitude, the propulsive force coefficient obtained with a positive mean pitch angle increases slowly with λ while it shows the opposite trend for a negative mean pitch angle. Figure 6c shows that the symmetrical pitching with large amplitude and the asymmetrical pitching with large negative mean pitch angles are more power-consuming than other cases, which is related to the energy loss induced by the more complex internal flow structures. At the same λ, though the propulsive force coefficient predicted by the symmetrical pitching with large amplitude is much larger, the efficiency remains similar, due to the large power. The asymmetrical pitching with negative mean pitch angle shows the worst performance in term of the efficiency, compared with the cases with a positive mean pitch angle. Thus, it can be concluded that the asymmetrical pitching with a positive mean pitch angle of 5° leads to the best global performance.

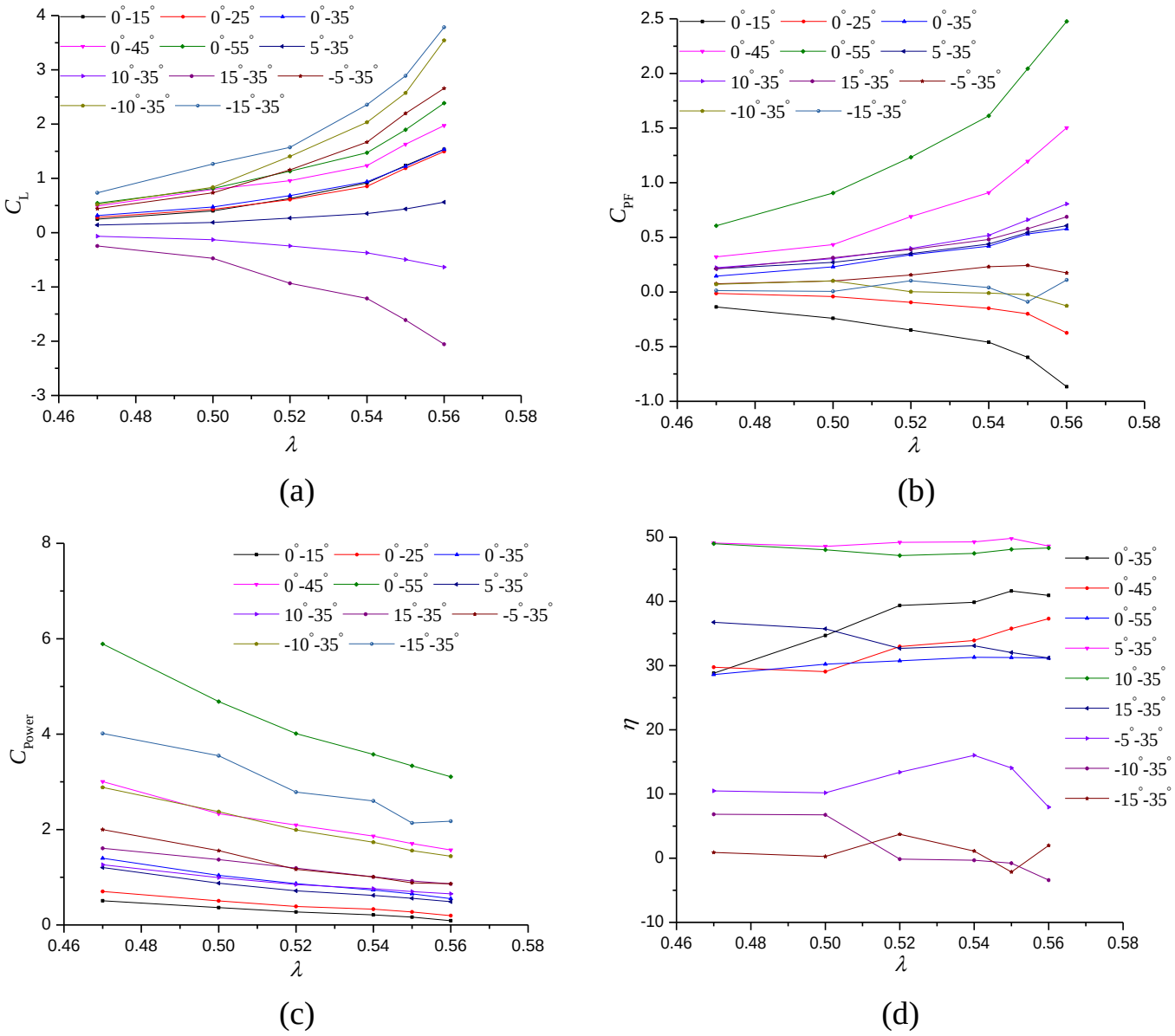

Fig.6 Performance curves at different λ for various pitching kinematics. (a) Lift coefficient; (b) Propulsive force coefficient; (c) Power coefficient; (d) Efficiency.

Two cases with symmetrical pitching and three cases with asymmetrical pitching at λ=0.52, are calculated to investigate the performance of both the propeller and a single blade during one rotation, as shown in figure 7. It is found that the symmetrical pitching with an amplitude of 55° produces the largest lift and propulsive force coefficients. Relatively high values of lift coefficients are obtained by the asymmetrical pitching with negative mean pitch angle, followed by the symmetrical pitching with amplitude of 35°. Evidently, the cases with a positive mean pitch angle generate the lowest lift coefficient, but a higher propulsive force coefficient, as shown in figure 7b. Based on the performance evolution of the single blade, it can be seen that the difference of vertical force coefficient production for different cases becomes larger gradually when the azimuthal angle exceeds 160°, which is closely associated with the distribution of relative incidence shown in figure 2c.

Simultaneously, the differences in the propulsive force coefficient are observed during almost all the cycle. Consequently, two azimuthal angles of 35° and 123°, coupled with two positions at ψ=35° and 160°, are analyzed in more detail to explain the difference of vertical force and propulsive force coefficients, respectively, for five pitching kinematics. At the same time, the locations of 15°, 75° and 147°, represented by the dash lines in figure 7b, are employed to describe the large variation of propulsive force coefficient for the symmetrical pitching with amplitude of 55°.

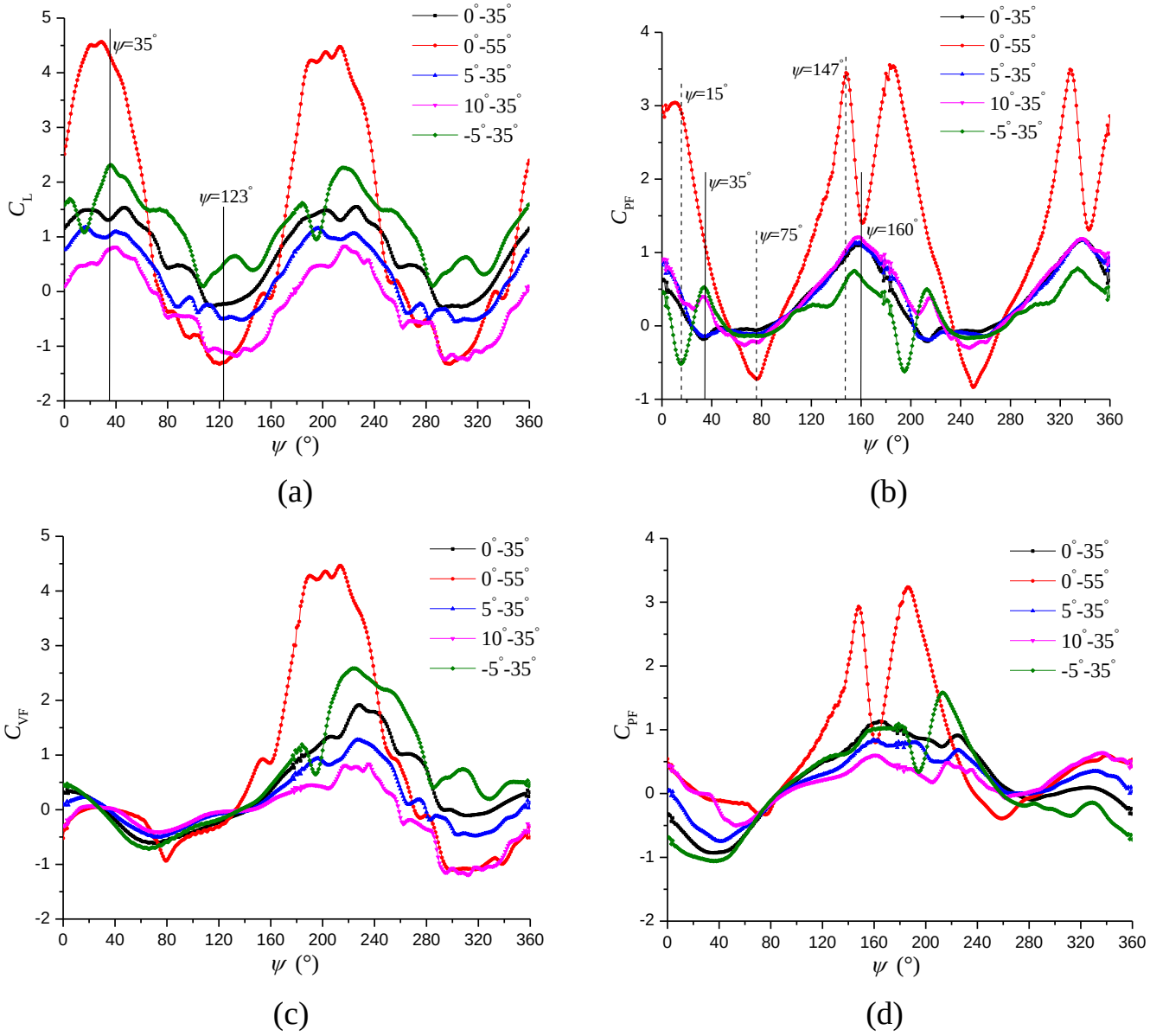

Fig.7 Performance curves for various pitching kinematics in a revolution. (a) Lift coefficient of the rotating system; (b) Propulsive force coefficient of the rotating system; (c) Lift coefficient of a single blade; (d) Propulsive force coefficient of a single blade.

The pressure distributions and flow filed at ψ=35° are displayed in figure 8 for different cases. As a supplement, the forces (lift and drag) and pressure coefficients of two blades are also shown to describe the force difference. For blade A (left blade),

three distinctive vortex structures are attached on the left surface when the pitching amplitude is 55°, which was also observed by Choudhuri and Knight [22] on a pitching airfoil at Re=1×10^4. Recently, Tseng and Hu [23] applied Lagrangian coherent structures (LCS) to a pitching airfoil operating at Re=4.5×10^3 and captured the co-existence of the leading-edge vortex (LEV), vortex A and B. They clarified that the generation of vortex B is due to the existence of vortex A which separates the connection between the shear layer and the LEV. Moreover, vortex A rotating in the opposite direction compared with vortex B and LEV, is mainly formed by the reverse flow from the other side and the fluid flow around the outer edge of LEV. In figure 8d, a series of roll-up vortices emerge in the laminar boundary layer. On a pitching airfoil, Negi et al. [24] found that these vortices are the main sources of laminar boundary layer instability when LSB is absent. In addition, it is reasonable that the transition model is easily subjected to the disturbances. When the positive mean pitch angle is small, vortex B occupies a large part of blade surface and LEV has already shed into the wake. However, as the mean pitch angle increases to 10°, vortex B is at the development stage and the LEV still remains near the trailing edge. For the case with a mean pitch angle of -5°, only a small scale is visible on the left side. Based on the velocity figures, it seems that the flow structures on the two sides of blade A depend on the position of the stagnation point due to the relative angle-of-attack. For an instance, in figure 8e, the stagnation point shifts towards the right side, leading to a relatively weak flow separation, compared with the case in figure 8d. However, the flow separation on the left side is stronger. Although the flow over blade A is more complex, the vertical force shown in figure 7c for different cases are almost the same. This is related to the balance of lift and drag components, presented by the force analysis in figure 8a.

On the suction side of blade B (right blade) in figure 8j, there is a large amount of vortex, like on the left side of blade A, resulting in the extremely low pressure. Because the lift of the rotating system is mainly produced by blade B, the vertical force provided by symmetrical pitching with large amplitude has the largest value. Meanwhile, due to the relatively small pressure difference in figure 8c for the case with mean pitch angle of 10°, the lift of the rotating system is the smallest. When the mean pitch angle is negative, a laminar separation bubble (LSB) is detected near the leading edge.

Then, the propulsive force at this location also exhibits much difference in various cases. Blade A generates a negative propulsive force while a positive propulsive force is produced by blade B, shown in figure 7d and 8a. For the case with a mean pitch angle of -5°, blade A has the largest pressure difference, resulting in a large negative propulsive force. Simultaneously, the positive propulsive force provided by blade B is also large due to the large pressure difference in figure 8c.

Therefore, the propulsive force of the rotating system has a relatively large magnitude. Similarly, for the symmetrical pitching with an amplitude of 35°, because of the small lift generated by blade B, the positive propulsive force is smaller than the negative propulsive force produced by blade A, so the total propulsive force has the lowest value. In general, it can be concluded that the lift of the rotating system is determined by blade B while both blade A and B are responsible for the propulsive force at ψ=35°, which is closely associated with the pressure difference of two blades.

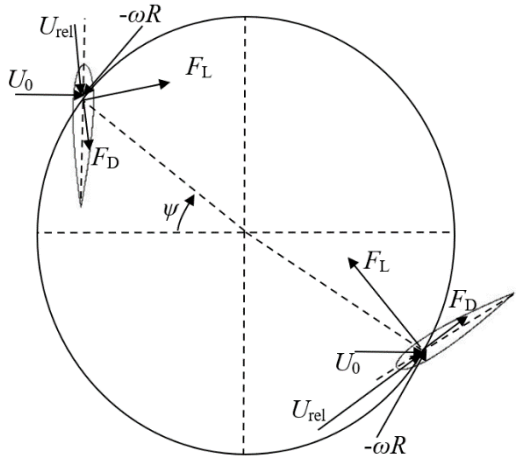

(a)

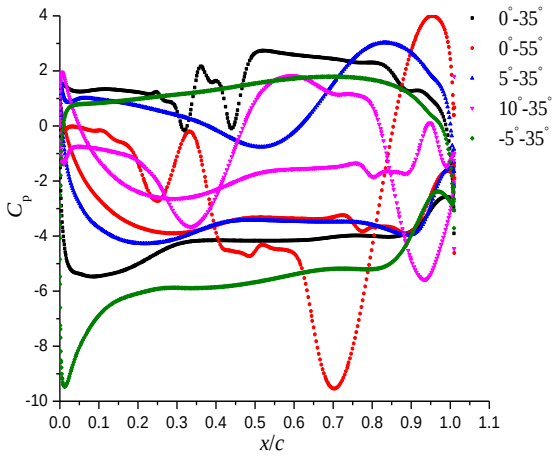

(b)

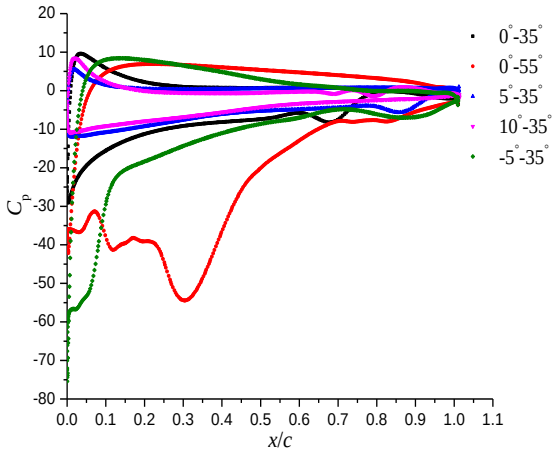

(c)

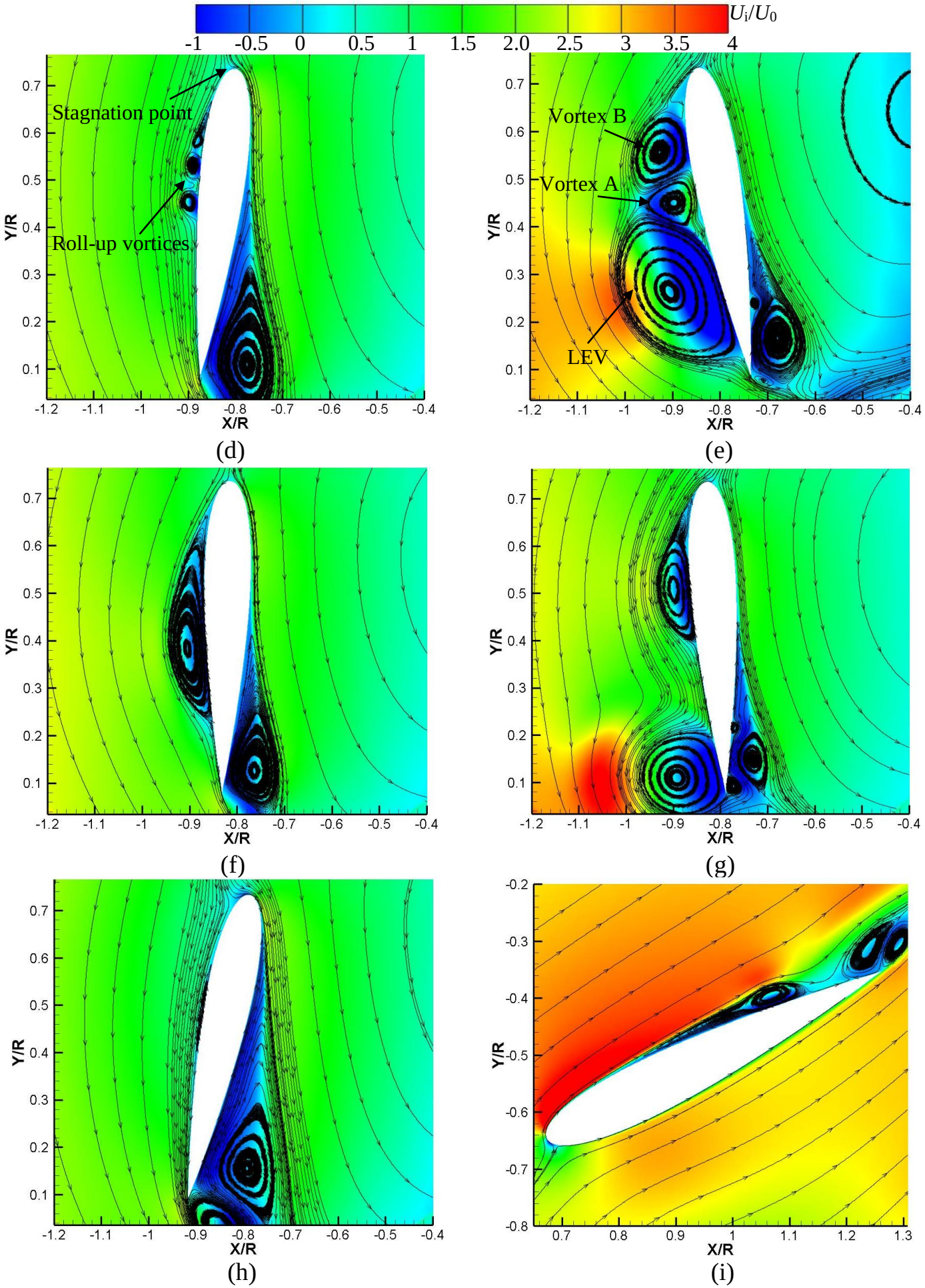
U_i/U_0
-1 -0.5 0 0.5 1 1.5 2.0 2.5 3 3.5 4
Stagnation point
Roll-up vortices
Vortex B
Vortex A
LEV
Y/R
X/R
(d)
(e)
(f)
(g)
(h)
(i)

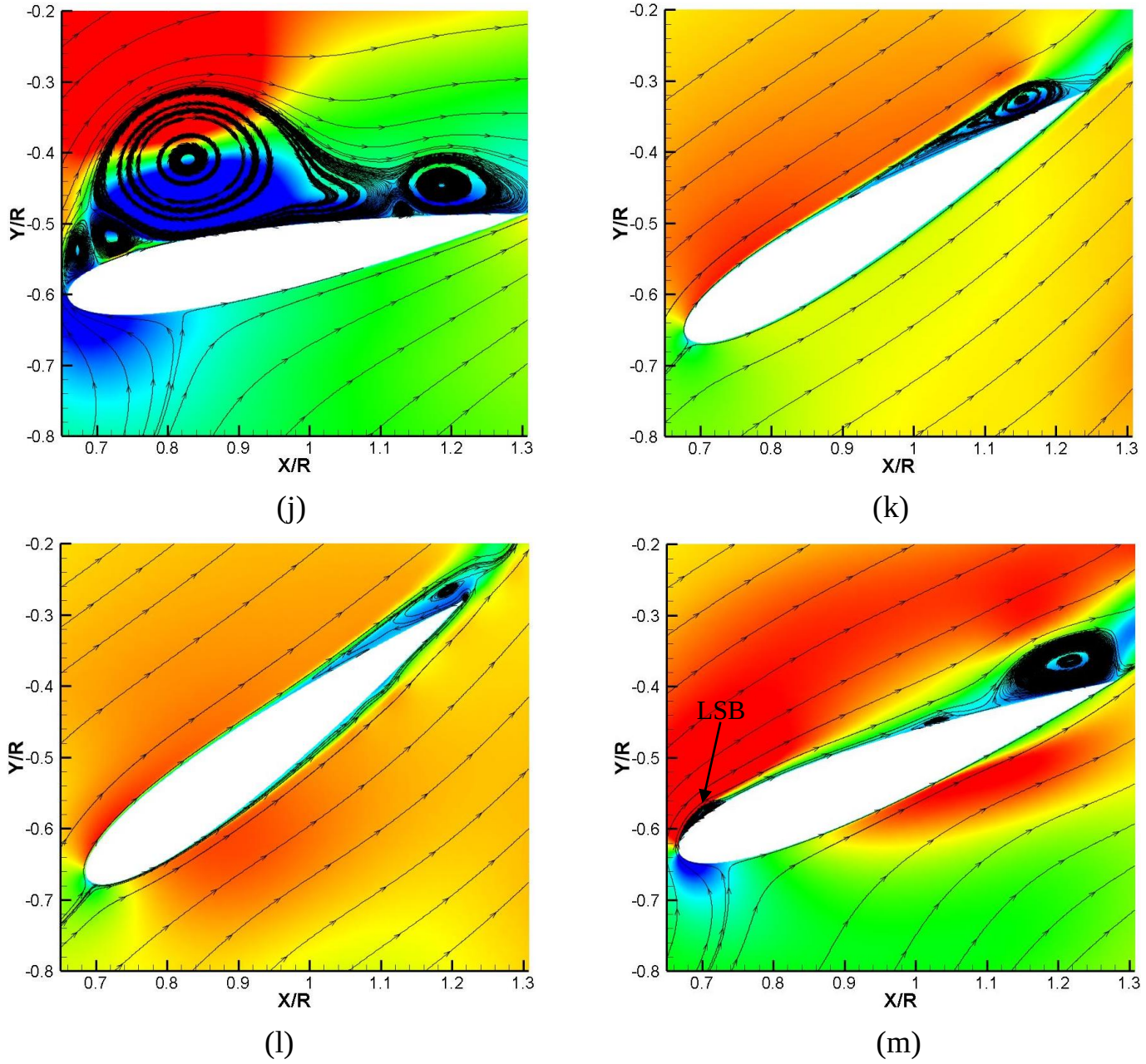

Fig.8 Flow structures for various pitching kinematics at ψ=35°. (a) Sketch of force; (b) Pressure distribution of blade A; (c) Pressure distribution of blade B; (d) and (i) 0°-35°; (e) and (j) 0°-55°; (f) and (k) 5°-35°; (g) and (l) 10°-35°; (h) and (m) -5°-35°.

Then, figure 9 shows the flow field over the surfaces of two blades at ψ=123°, when the lift of the rotating system is dropping as shown in figure 7a. At this position, the blade A is experiencing the retreating side, and the flow separation mainly emerges on the suction side at the trailing edge, where the trailing edge vortex (TEV) interacts with the LEV, especially for the case in figure 9d. For the symmetrical pitching with an amplitude of 55°, the flow is relatively smooth on the suction side, but the pressure is sufficiently low due to the large relative incidence. When the mean pitch angle is 10°, a large-scale vortex remains near the trailing edge on the pressure side, resulting in the pressure drop visible in figure 9b. According to the force sketch

in figure 9a, the lift component is larger than the drag component, especially for the symmetrical pitching with an amplitude of 55°, which is producing the large blade loading, resulting in the negative vertical force of blade A shown in figure 7c.

The lift of blade B has not the same direction for various pitching kinematics. For example, for the case in figure 9m, due to the presence of the LEV on the upper surface, the resultant lift of blade B is upward (the opposite direction in figure 9a). However, when the blade operates with the symmetrical pitching with an amplitude of 55° or an asymmetrical pitching with positive mean pitch angles, the lift of blade B is downward, as shown in figure 9a, creating the negative vertical force. When the mean pitch angle is 10°, the large pressure difference in figure 9c leads to the generation of a large lift on blade B, so the vertical force in figure 7c has a large negative value. It can be seen that the lift direction of blade B has a close relationship with the stagnation point location. When the stagnation point shifts towards the upper surface, the flow separation occurs on the lower surface, resulting in the downward lift. Finally, it can be concluded that the lift difference of the rotating system for various cases is generally caused by the lift direction of blade B because of the stagnation point location.

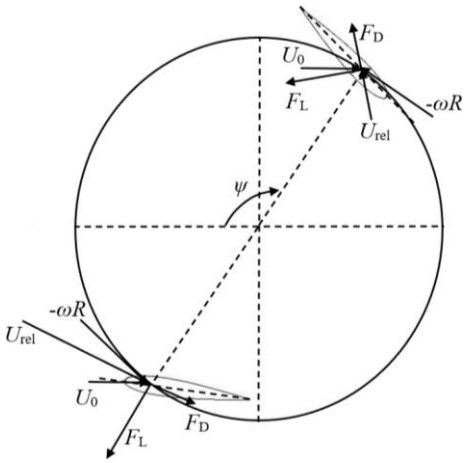

(a)

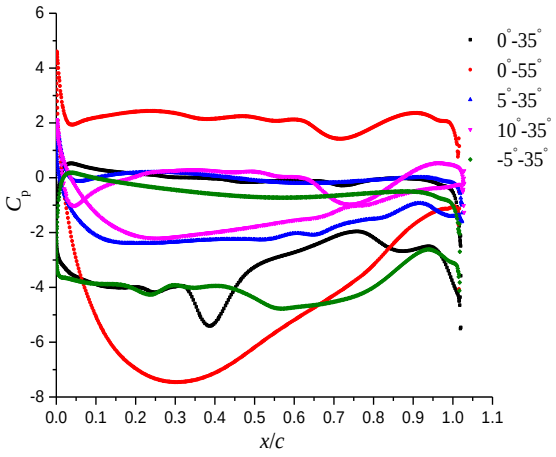

(b)

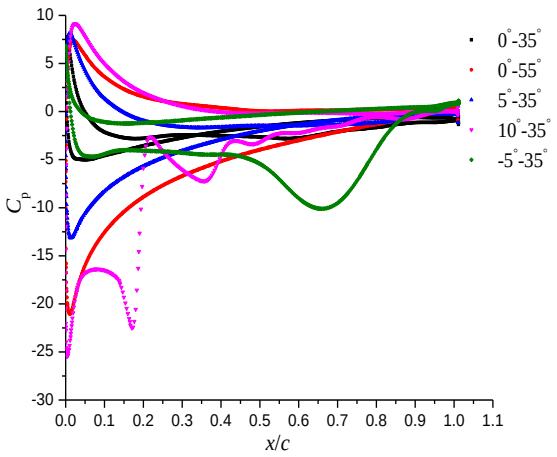

(c)

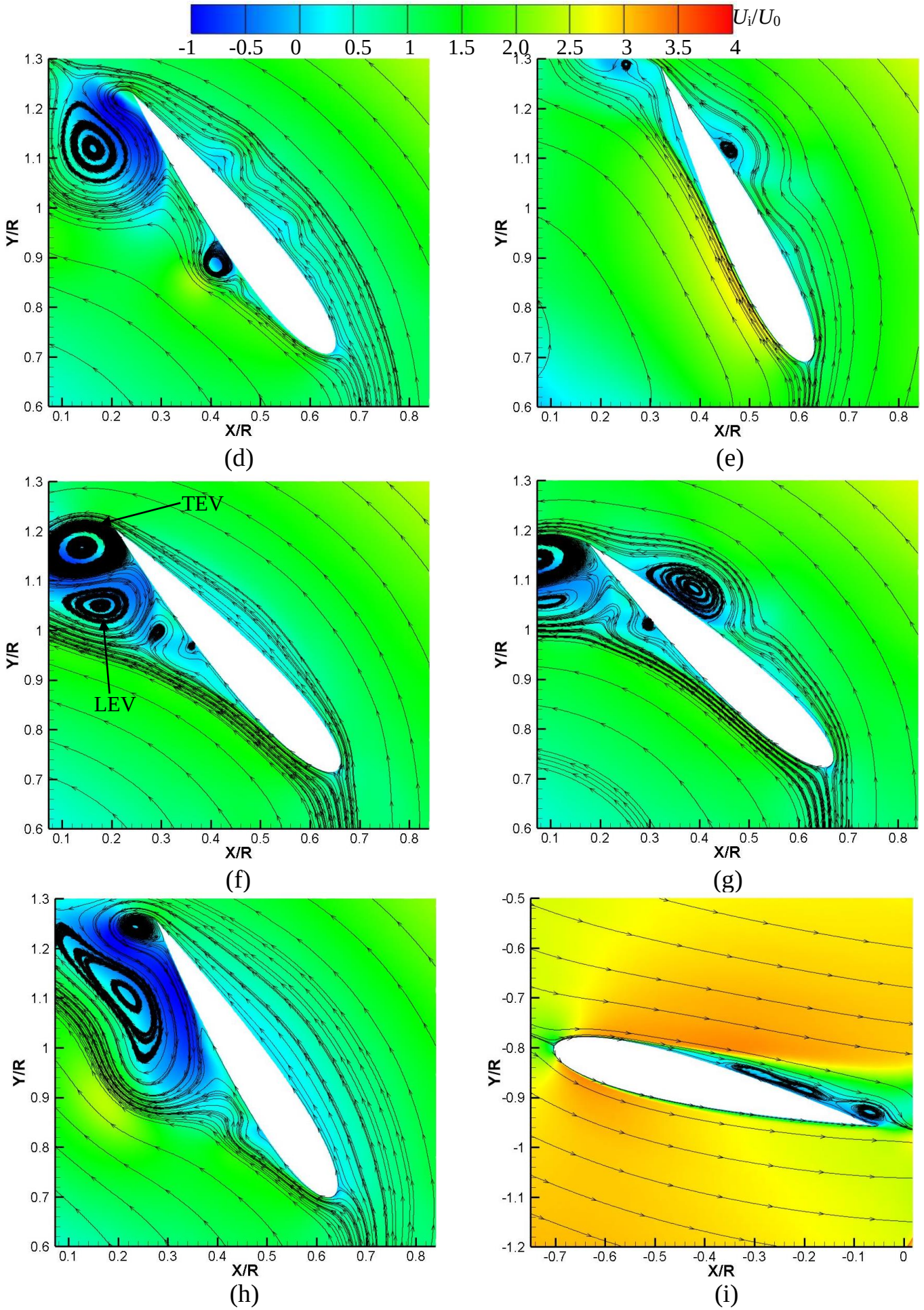

(d) (e)

(f) (g)

(h) (i)

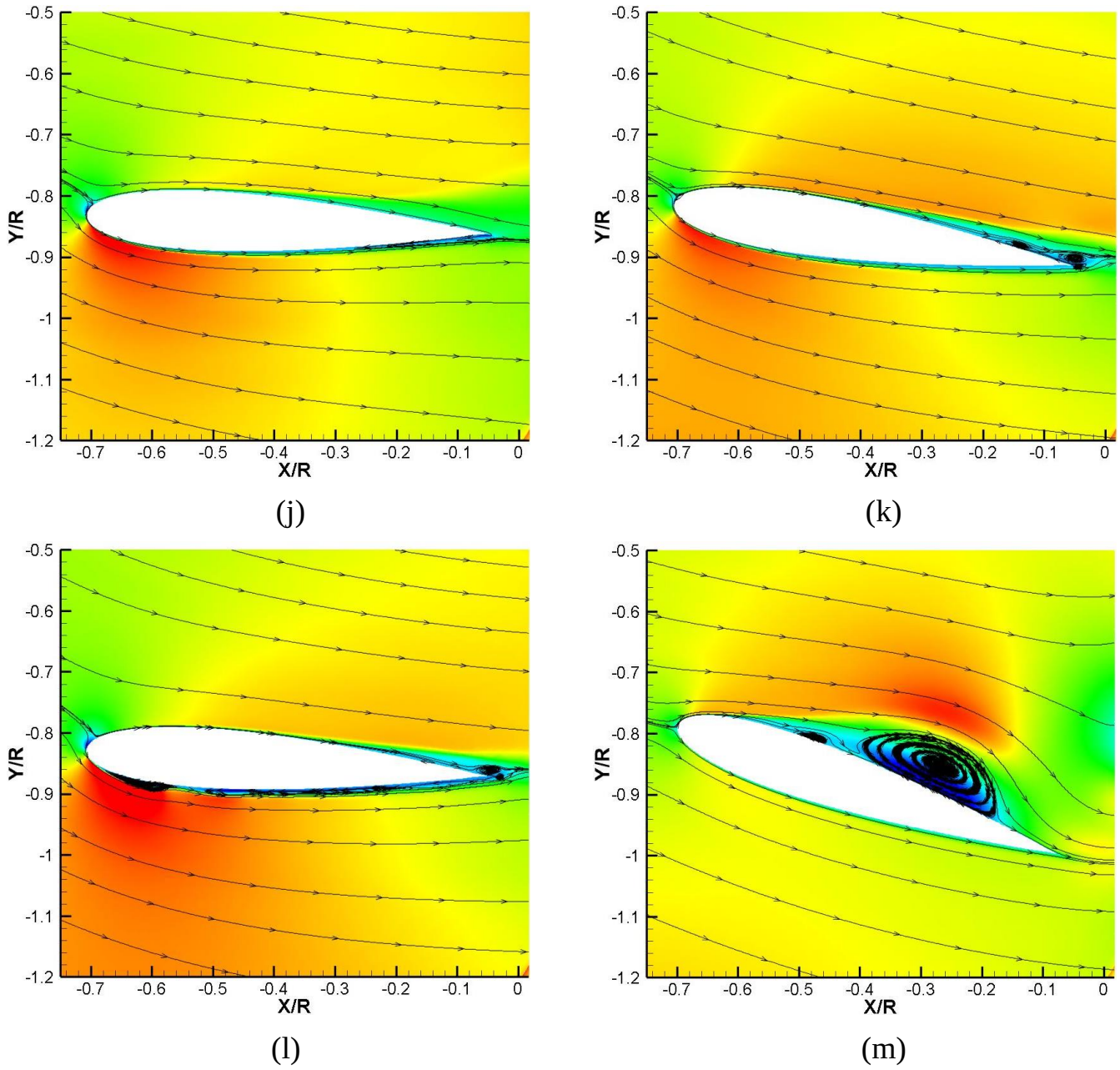

Fig.9 Flow structures for various pitching kinematics at ψ=123°. (a) Sketch of force; (b) Pressure distribution of blade A; (c) Pressure distribution of blade B; (d) and (i) 0°-35°; (e) and (j) 0°-55°; (f) and (k) 5°-35°; (g) and (l) 10°-35°; (h) and (m) -5°-35°.

At ψ=160°, in figure 7b, the propulsive force shows large differences between the symmetrical pitching with an amplitude of 55° and the asymmetrical pitching with a negative mean pitch angle. Thus, the flows over the two blade surfaces are displayed in figure 10. The separation flow only appears on the suction side of blade A when the blade has the symmetrical pitching. With the increase of the pitching amplitude, the flow separation is more obvious in figure 10e due to the relatively large incidence. From the pressure distribution in figure 10b, it seems that the pressure on both sides for the symmetrical pitching with large amplitude differ from that for other cases, as a consequence of the incidence and stagnation point location.

At this position, the propulsive force of blade A is positive because of the upward lift, but its value is relatively small for the case with mean pitch angle of 10°, as shown in figure 10b.

Then, because the stagnation point is moving towards the upper side, the vortex structures mentioned in figure 8 occur on the lower surface for the symmetrical pitching with large amplitude and the asymmetrical pitching with positive mean pitch angles. Therefore, the lower pressure on the suction side produces the downward lift, creating the positive propulsive force of blade B, which is shown in figure 10a. Due to the large pressure difference in figure 10c, the propulsive force of the rotating system for symmetrical pitching with large amplitude and asymmetrical pitching with large positive mean pitch angle, has the largest magnitude. But for asymmetrical pitching with negative mean pitch angle, the flow separation is on the upper side and the resultant lift is upward, leading to the generation of negative propulsive force. Therefore, although the blade A can produce the relatively large positive propulsive force, the total propulsive force for the rotating system is the smallest. In general, the total propulsive force is determined by the two blades, especially for blade B, because the lift direction is different for various pitching kinematics, depending on the angle of attack, which changes the stagnation point and flow structures significantly.

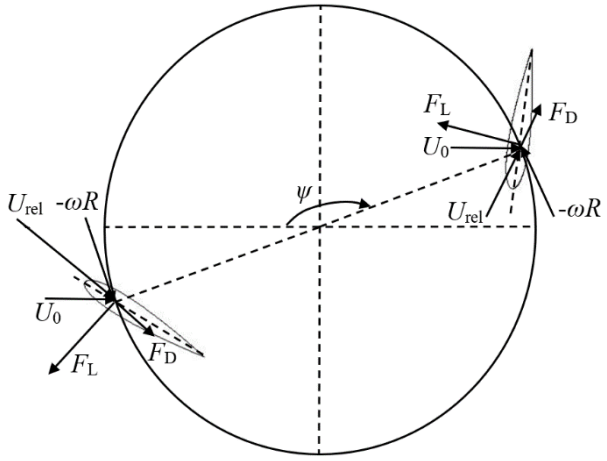

(a)

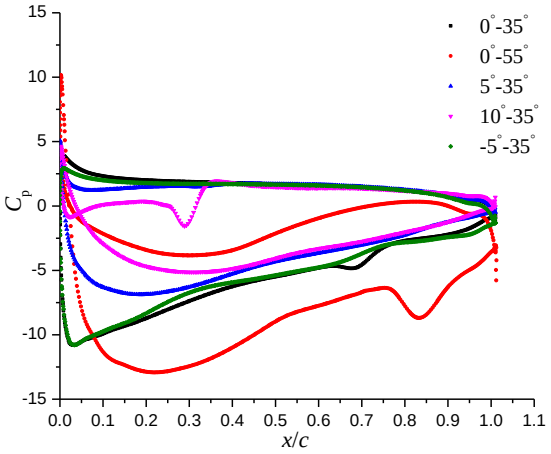

(b)

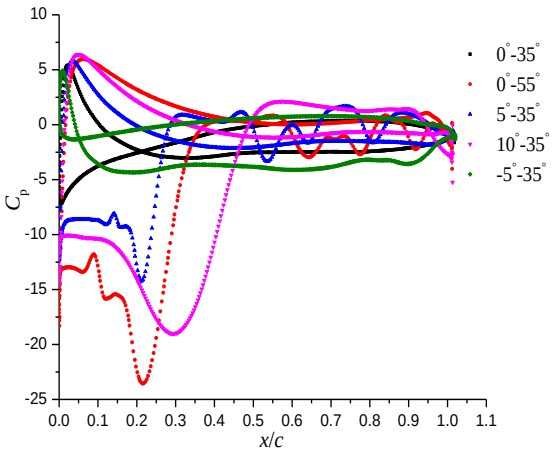

(c)

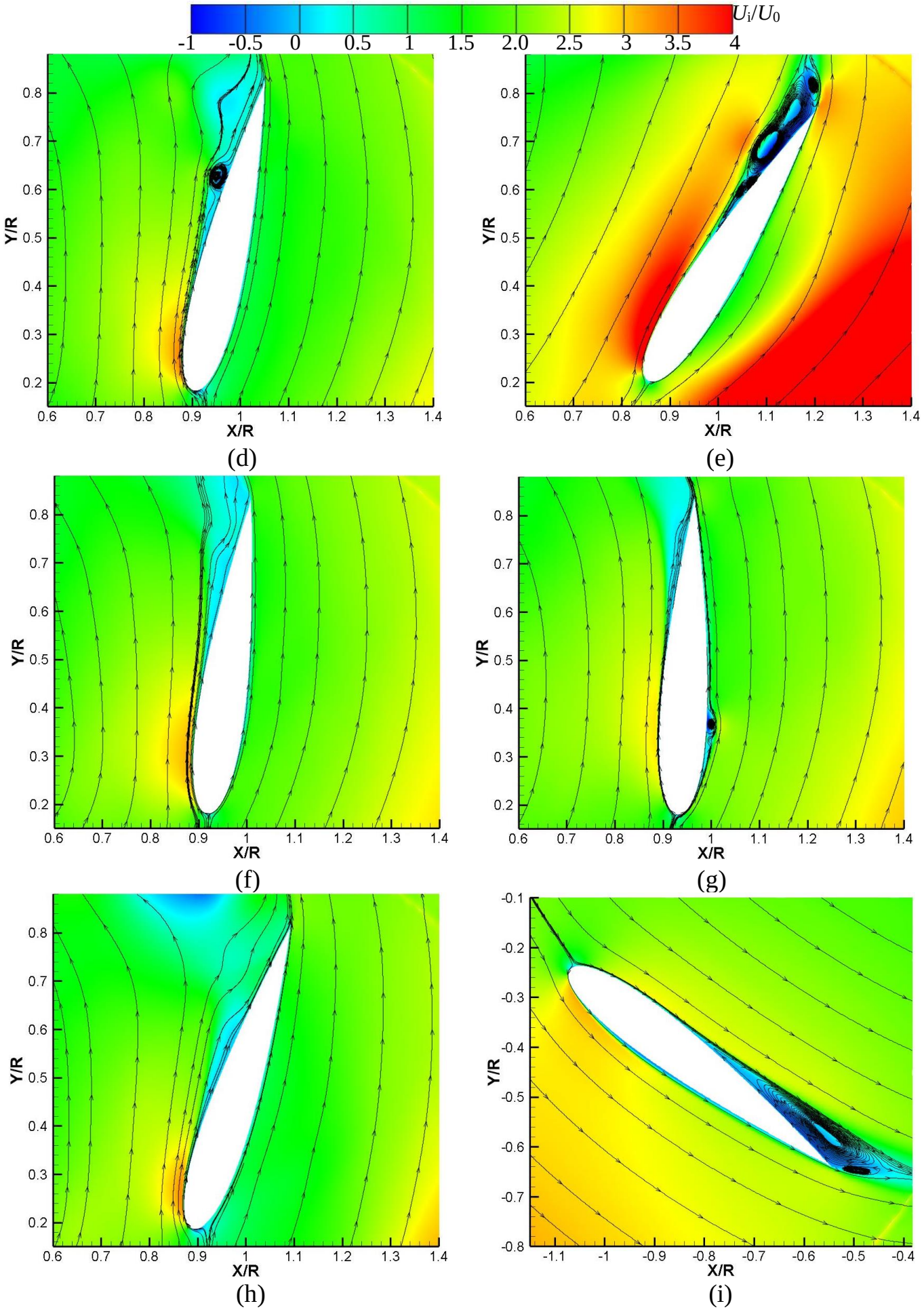
U_i/U_0
-1 -0.5 0 0.5 1 1.5 2.0 2.5 3 3.5 4
Y/R
X/R
(d)
(e)
(f)
(g)
(h)
(i)

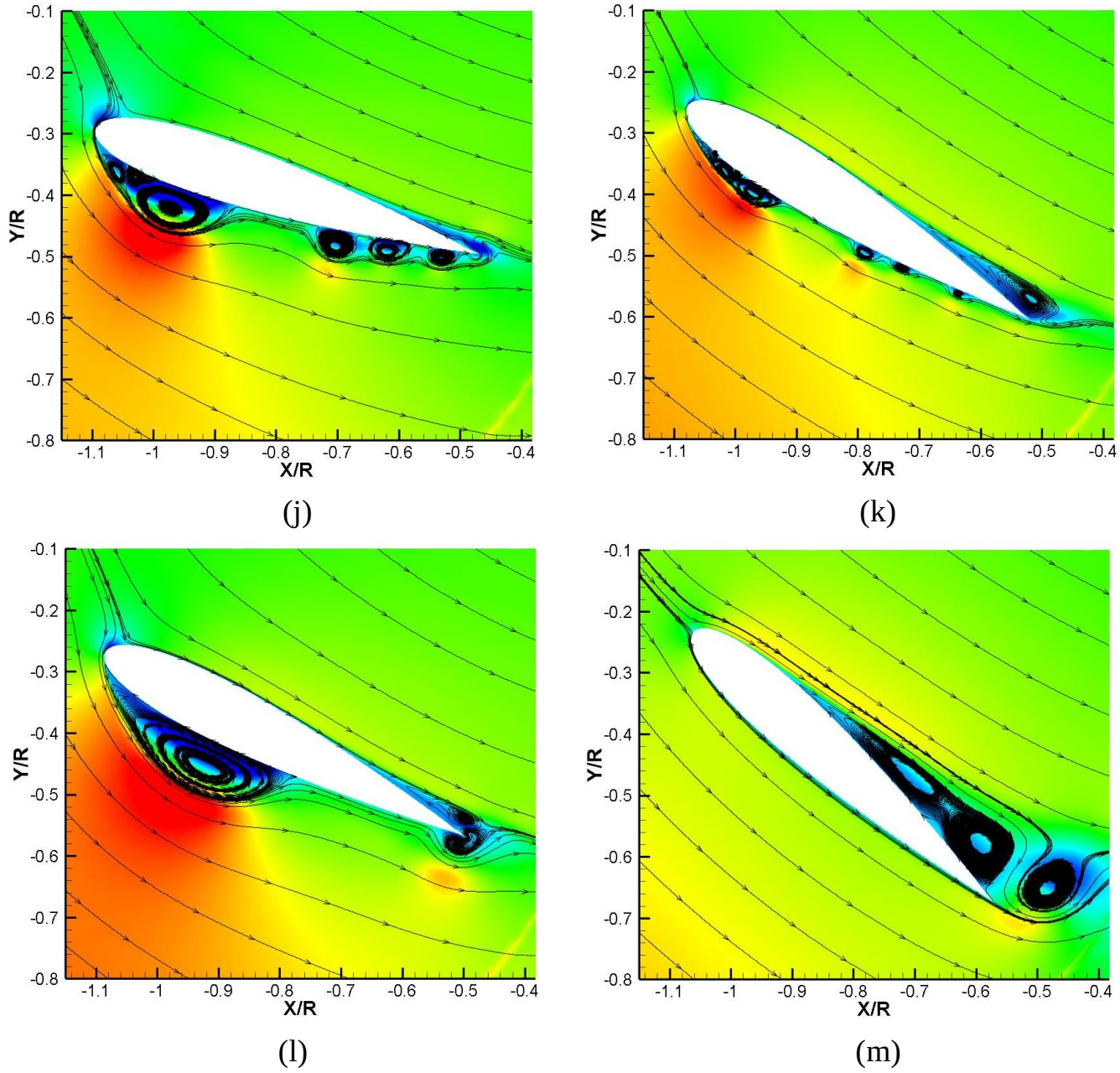

Fig.10 Flow structures for various pitching kinematics at ψ=160°. (a) Sketch of force; (b) Pressure distribution of blade A; (c) Pressure distribution of blade B; (d) and (i) 0°-35°; (e) and (j) 0°-55°; (f) and (k) 5°-35°; (g) and (l) 10°-35°; (h) and (m) -5°-35°.

Figure 11 shows the flow structures for the symmetrical pitching with an amplitude of 55° at three azimuthal angles, namely 15°, 75° and 147°, to clarify why the total propulsive force has large variations at these positions. At ψ=15°, the pressure difference on blade B is much larger than that on blade A, as shown in figures 11a and 11b. On the left side of blade A, three kinds of vortex nearly cover the large part of the surface, but the low pressure on the aft part recovers obviously. Furthermore, the LSB, triggering the transition, is located near the leading edge of blade B and then the flow separation occurs near the trailing edge. At this instant,

due to the large pressure difference of blade B, the positive propulsive force of the rotating system has the maximal value.

As ψ increases to 75°, on both sides of blade A, the massive flow separation is evident. The component of lift produces a negative propulsive force, but its magnitude is relatively small due to the blade loading in figure 11a. Meanwhile, the blade B can still produce the upward lift owing to the pressure drop on the trailing edge of upper surface, leading to the negative propulsive force. Consequently, the rotating system has the peak of negative propulsive force.

Finally, at ψ=147°, the rotating system has the positive peak of propulsive force, as a consequence of the large positive propulsive force generated by blade A because of the large blade loading in figure 11a, which is quite similar to the situation at ψ=160°. At the same time, blade B creates a downward lift, which can produce the positive propulsive force. However, the loading is smaller on blade B than on blade A, so the positive propulsive force of blade B is much smaller.

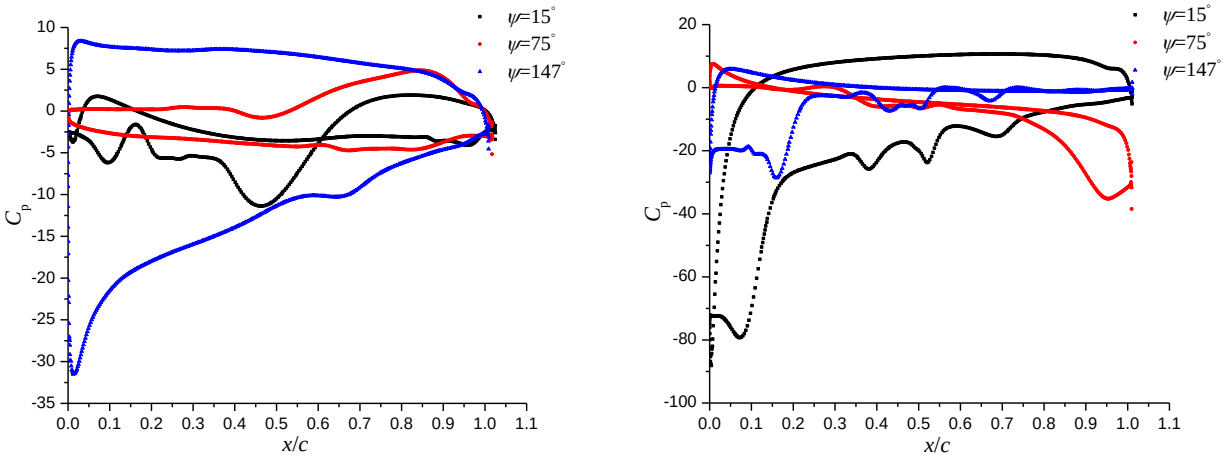

(a) (b)

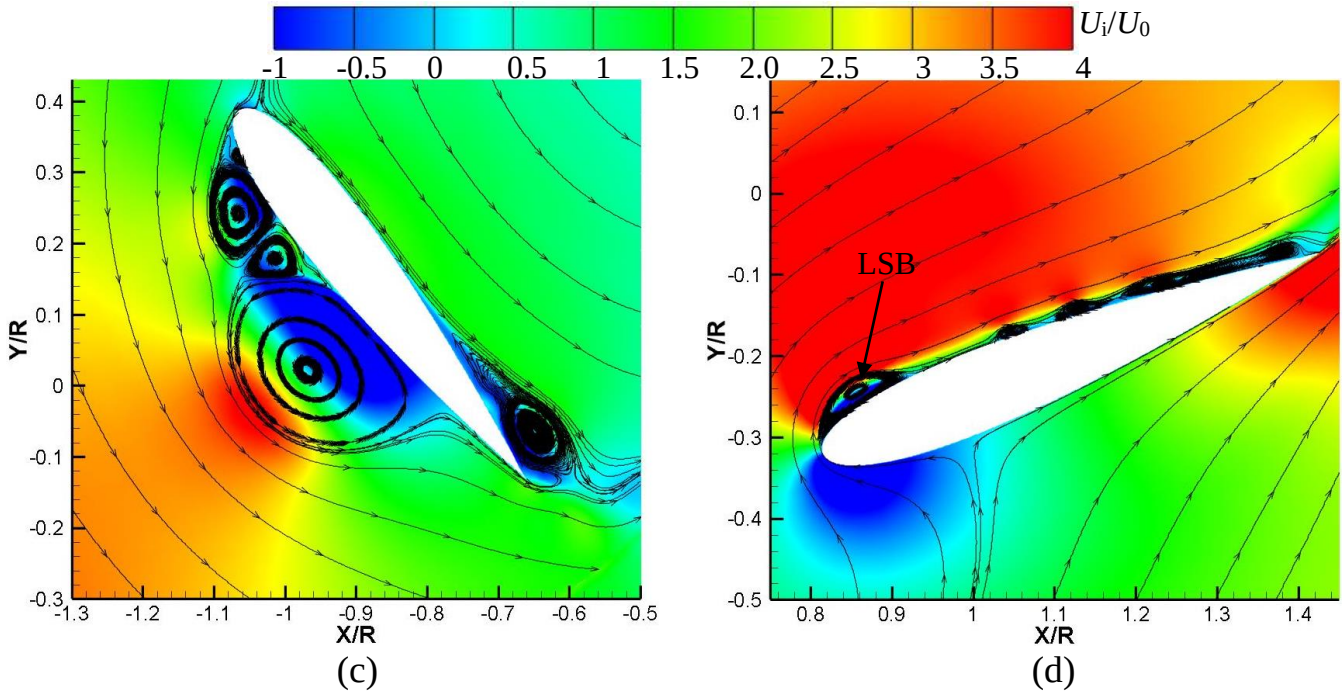

(c) (d)

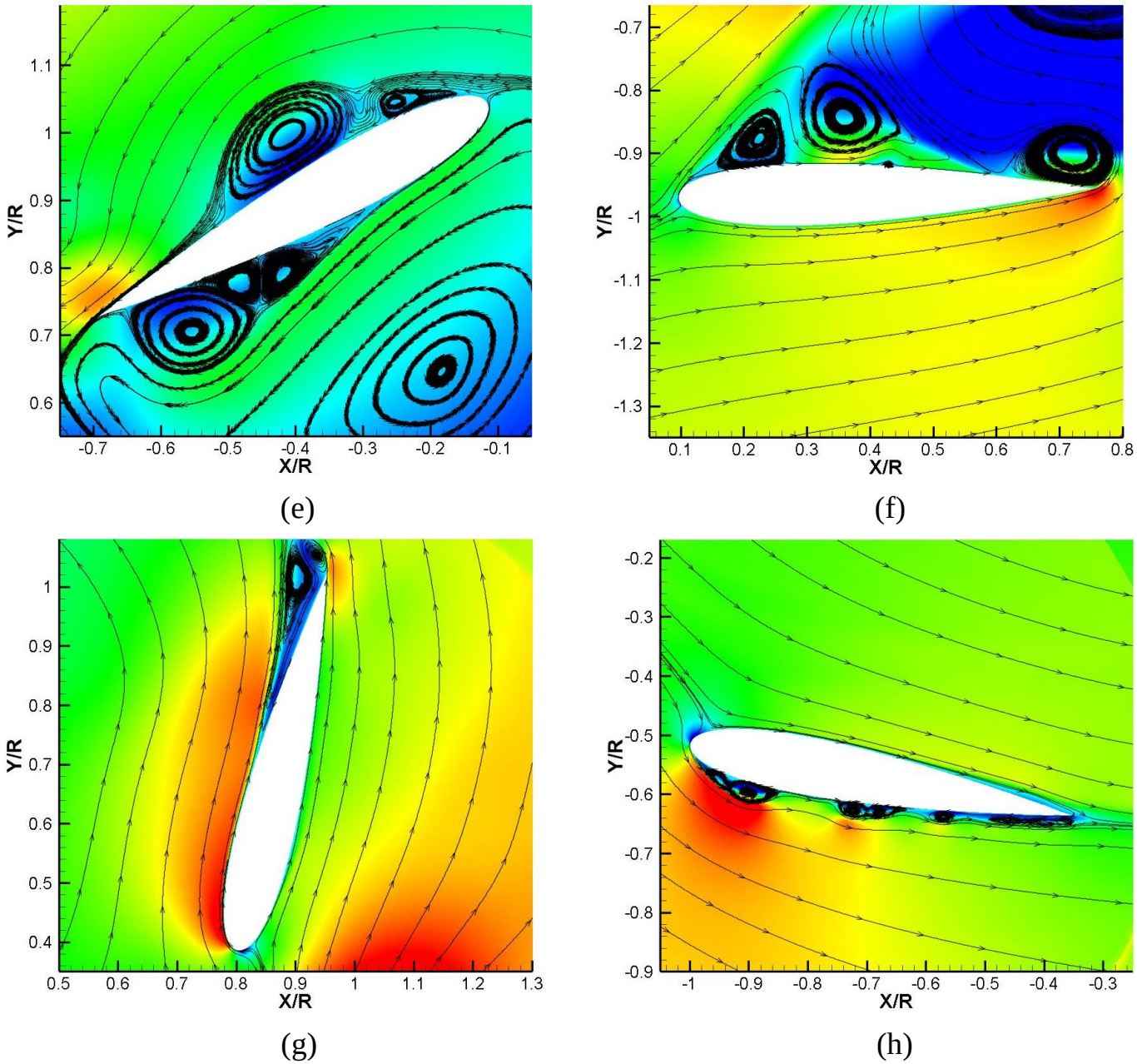

Fig.11 Flow structures of two blades for symmetrical pitching with amplitude of 55° at different ψ. (a) Pressure distribution of blade A; (b) Pressure distribution of blade B; (c) and (d) ψ=15°; (e) and (f) ψ=75°; (g) and (h) ψ=147°.

3.2 Influence of the chord-to-radius ratio

3.2.1 At same advance coefficient λ and Reynolds number Re

The blade chord-to-radius ratio is one of the critical parameters that can affect the performance of both the cycloidal rotor system and the single blade. Most previous studies only consider one of them, which is not appropriate for a better design of some high-performance propulsive devices. In the present work, both of these two parameters, namely the blade chord length *c* and rotor radius *R*, are considered. With a fixed blade chord, both the rotating speed and the rotor radius are

changed, to vary the chord-to-radius ratio while keeping the advance coefficient and the Reynolds number unchanged. Then, the influence of the blade chord length is evaluated at the same λ and Re. In figure 12, it seems that with the increase of c/R until the value below 0.65, the lift coefficient of the rotating system increases, which is almost the same for different blade chord lengths. After that, it has a rapid rise for c=0.0495m. The propulsive force coefficient obtained with different blade chords is quite similar, characterized by the curves that have a rise from c/R=0.30 to 0.45 initially and an obvious drop after that. Then, the power coefficient increases firstly and then has a slight decrease, and finally increases again significantly at relatively large c/R, which is due to the more complicated flow structures when the two blades are quite close caused by the decrease of R. As a result, the best efficiency is around c/R=0.45, but the magnitude increases with the blade chord length. As c/R increases, due to the increase of the power and decrease of the propulsive force, the efficiency of the rotating system decreases obviously. Generally, a too small or too large rotor radius is not beneficial to the global performance, so an appropriate value of c/R is necessary to achieve the high efficiency.

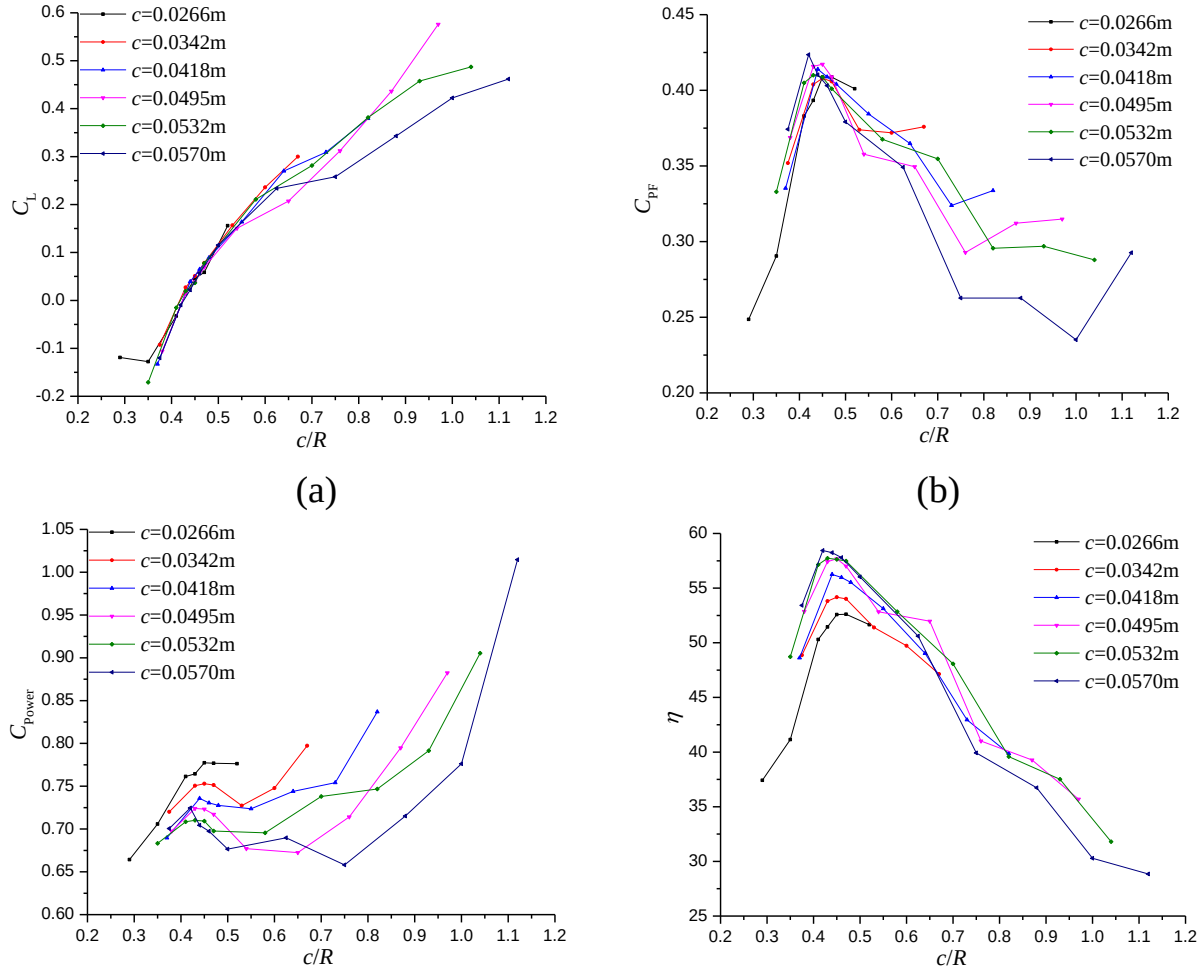

Fig.12 Performance curves at λ=0.52 and Re=2.46×10^4. (a) Lift coefficient; (b) Propulsive force coefficient; (c) Power coefficient; (d) Efficiency.

Three cases with c/R=0.375, 0.45 and 0.60, at λ=0.52 and Re=2.46×10^4, are selected to study the detailed flow structures and their influence on the performance of the rotating system and the single blade. The forces of the cycloidal rotor and single blade are plotted in figure 13, for a fixed blade chord length equal to 0.0342m. The results show that the lift coefficient of the rotating system increases with c/R, while the propulsive force coefficient predicted by the case with c/R=0.45 is the largest, as a result of the large propulsive force coefficient produced from ψ=10° to 90° and ψ=190° to 270°. Moreover, in figure 13c and 13d, it can be seen that the vertical force coefficient of cases with c/R=0.375 and 0.45 is nearly the same in a rotating cycle, but has much difference compared with the case with c/R=0.6. Similarly, except the region of ψ=0°-90°, the propulsive force coefficient obtained by the case with c/R=0.6 has significant difference compared with other two cases. Thus, two specific blade positions at ψ=45° and 142°, corresponding to the positive and negative peaks of the lift coefficient, are adopted to analyze the internal flows. Additionally, regarding the difference of propulsive force coefficient, the flow structures obtained in the cases c/R=0.375 and 0.45 at ψ=180° and in the case c/R=0.60 at 160° (presented by the dash line), are investigated in detail.

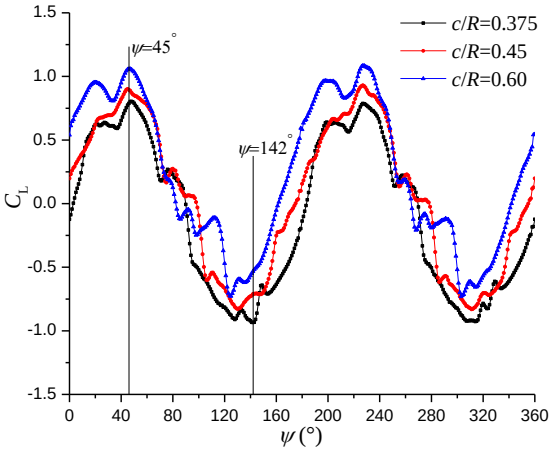

(a)

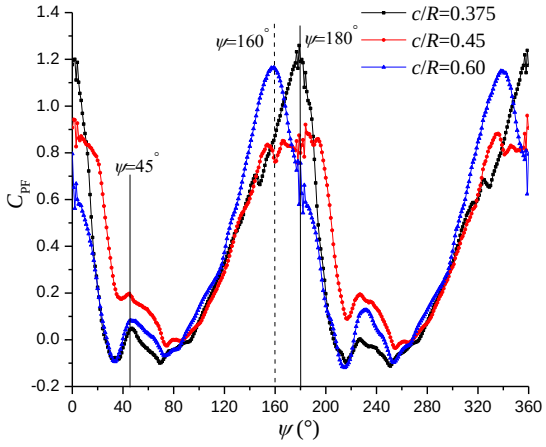

(b)

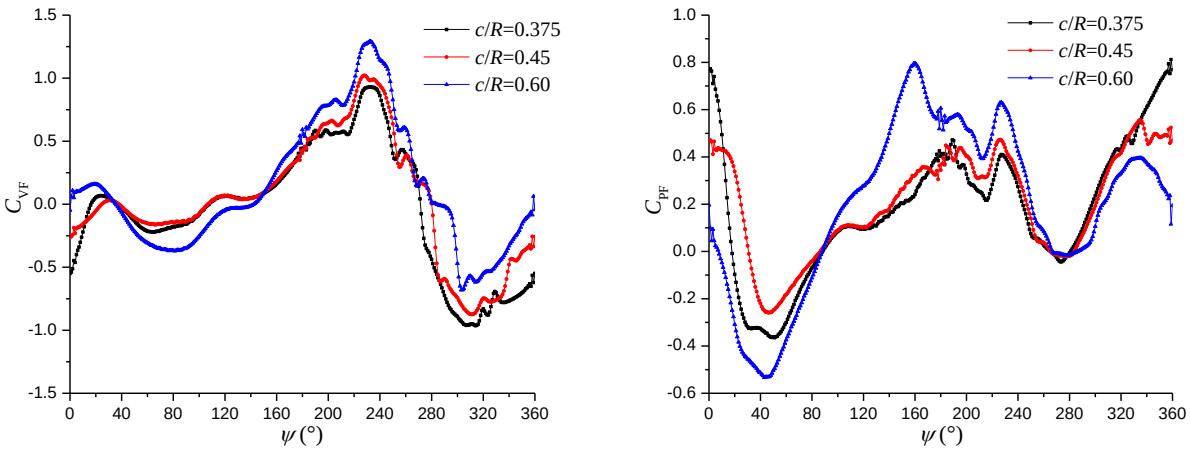

Fig.13 Performance curves for various *c*/*R* in a revolution. (a) Lift coefficient of the rotating system; (b) Propulsive force coefficient of the rotating system; (c) Lift coefficient of single blade; (d) Propulsive force coefficient of single blade.

In figure 14, with the combination of global flow morphology, pressure distributions and relative velocity contours on the two blades, the lift differences at ψ=45° are explained for various *c*/*R*. At this moment, wake A interacts with blade B, which is more obvious with the increase of *c*/*R* because of the narrow distance between the two blades. Similarly, wake B also has large possibility to contact with itself. In general, as *c*/*R* increases, the vortex flow is more violent because it does not have enough time to dissipate for two close blades. According to the pressure distribution in figure 14d, it can be seen that due to the vortex attachment on the left side of blade A, the blade loading for three cases have a remarkable difference. However, the vertical force produced by blade A is almost the same, which is caused by the balance of the lift and drag components, as shown in figure 13c. Therefore, blade B becomes the main contributor to the global lift for the rotating system. It should be mentioned that the pressure on the suction side changes considerably if the rotating speed changes, which is equivalent to the change of pitching rate. Kim et al. [25] reported that the reduced frequency of the pitching airfoil is the main factor determining the unsteady boundary layer under low Reynolds number condition. The stagnation point location changes the pressure distribution on both two sides for the case *c*/*R*=0.60, which is shown in figure 14e. The resultant large pressure difference leads to the large lift generated by blade B, leading to the large lift of the rotating system.

The propulsive force created by blade A and B varies a lot in the three cases. The components of both lift and drag of blade A produce a negative propulsive force, especially for the case *c*/*R*=0.60, due to the large pressure difference visible in figure 14d. Then, blade B produces the upward lift, leading to the generation of a positive propulsive force. The largest propulsive force of blade B results from the largest

pressure difference shown in figure 14e. By the combination of two blades, the case with c/R=0.45 shows the best performance regarding the positive propulsive force.

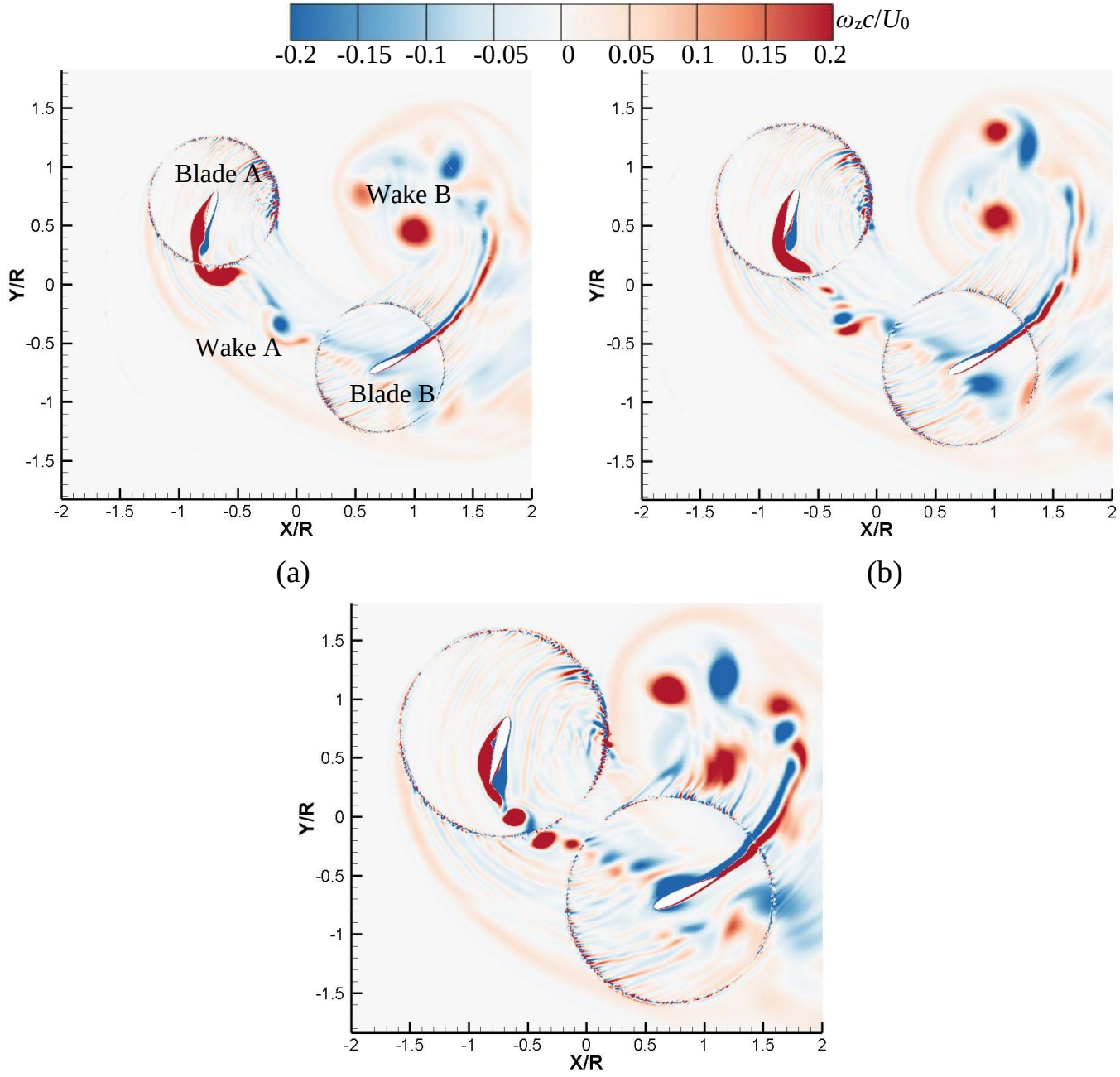

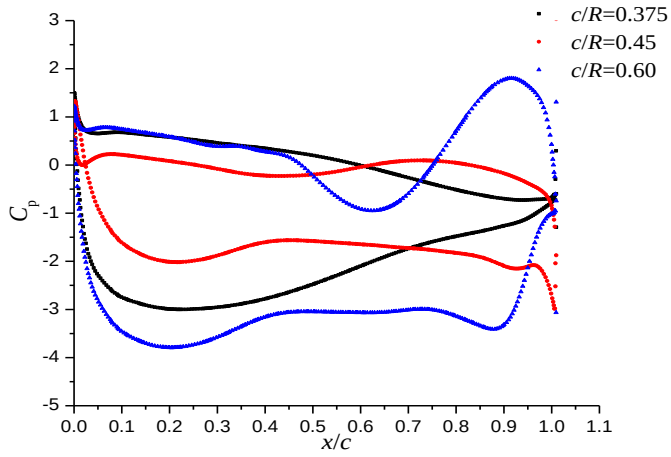
c/R=0.375
c/R=0.45
c/R=0.60
Cp
x/c

(d)

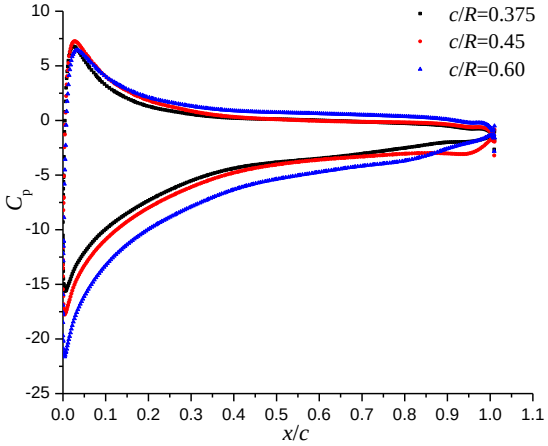
c/R=0.375
c/R=0.45
c/R=0.60
Cp
x/c

(e)

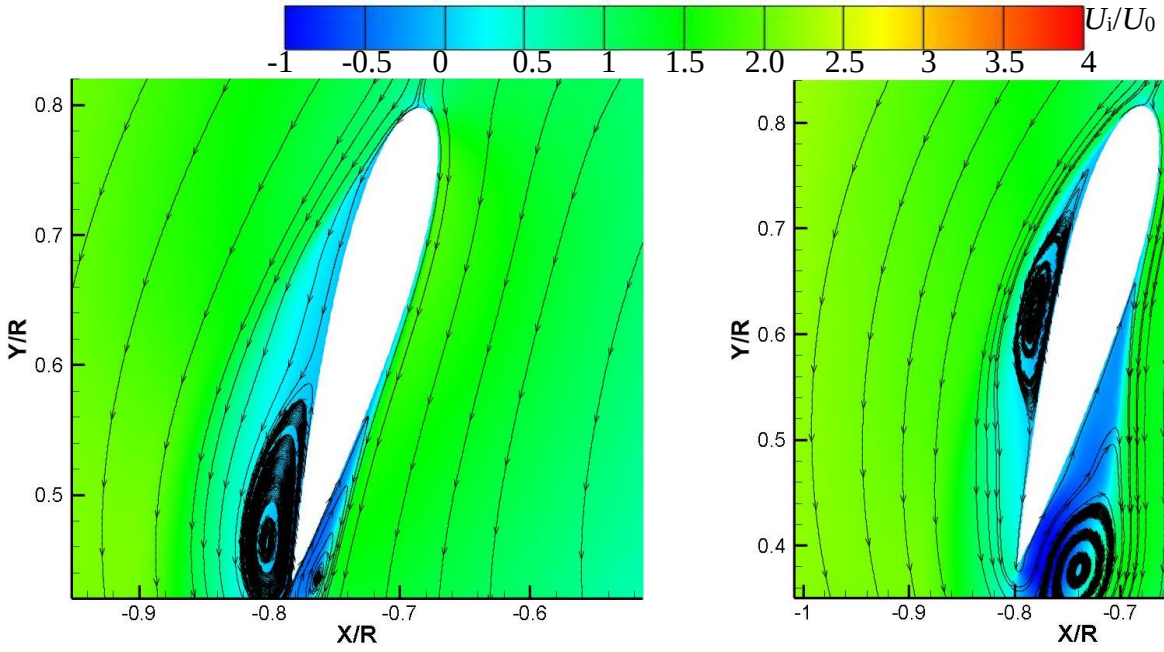
Ui/U0
Y/R
X/R

(f)

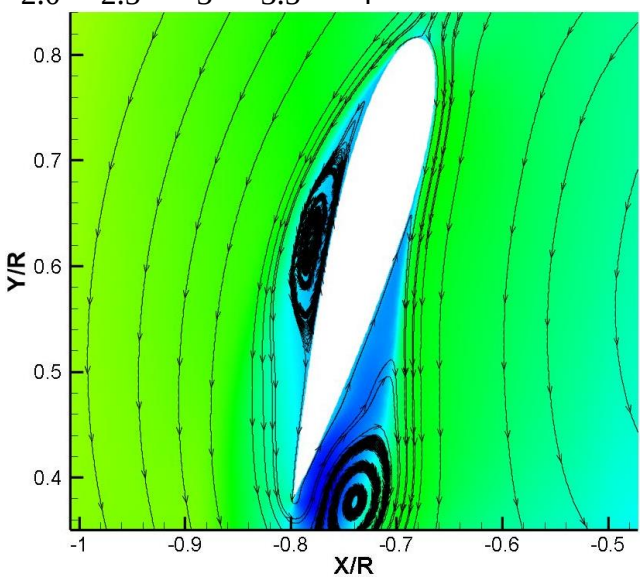
Y/R
X/R

(g)

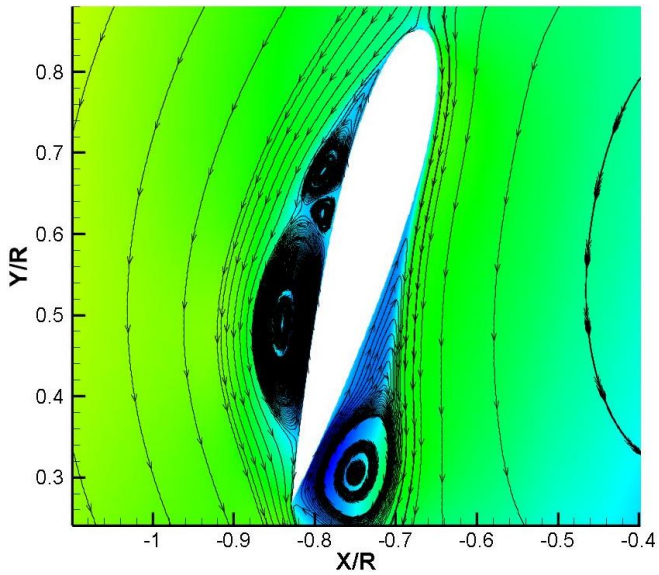
Y/R
X/R

(h)

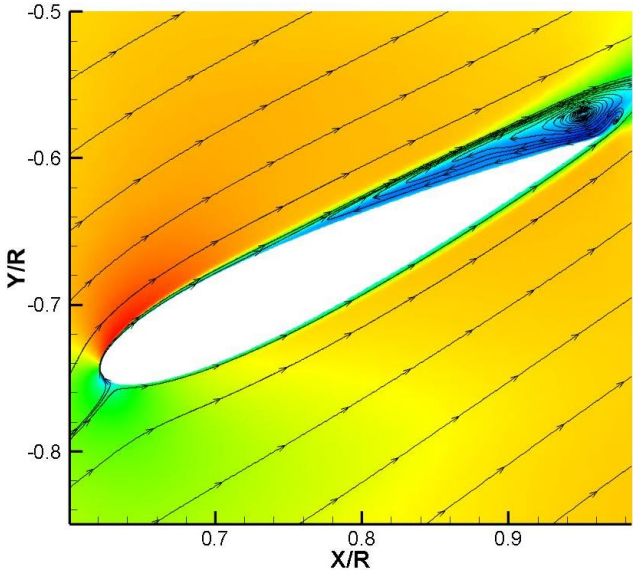
Y/R
X/R

(i)

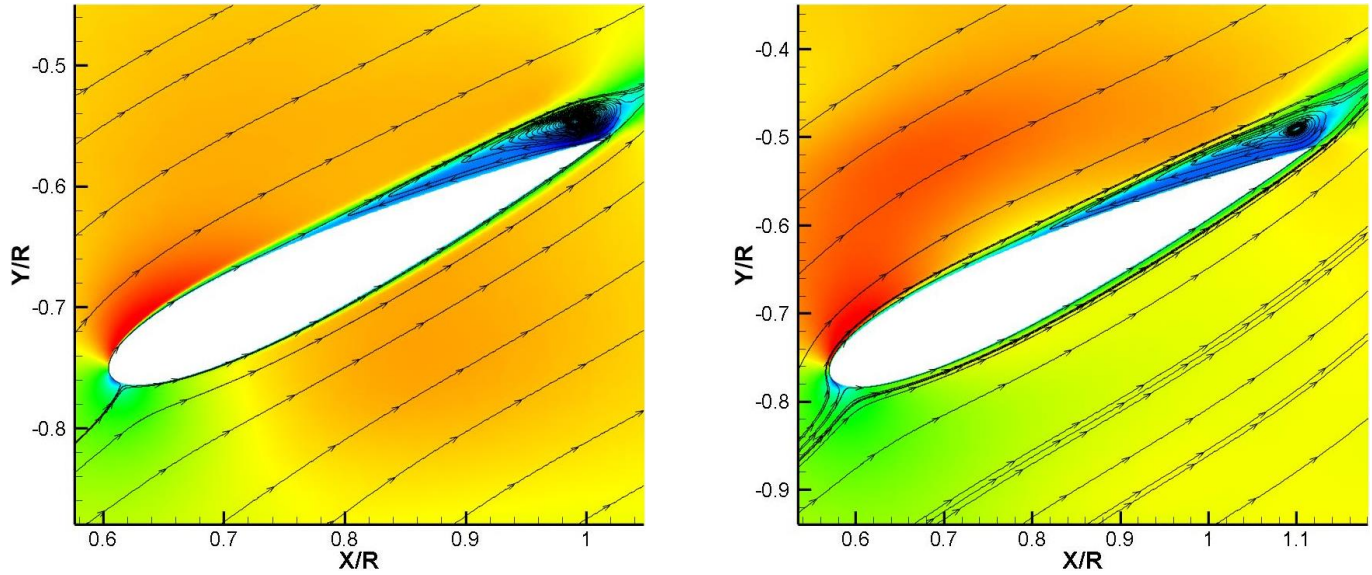

(j) (k)

Fig.14 Flow structures for various c/R at ψ=45°. (a) Global flow structure for c/R=0.375; (b) Global flow structure for c/R=0.45; (c) Global flow structure for c/R=0.60; (d) Pressure distribution of blade A; (e) Pressure distribution of blade B; (f) and (i) c/R=0.375; (g) and (j) c/R=0.45; (h) and (k) c/R=0.60.

As ψ increases up to 142°, the lift coefficient of the rotating system experiences a negative peak. The global flow structures for different cases are relatively smooth, but the wake shedding from blade A will likely interact with wake B when c/R is large (see figure 15c). The flows on two sides of blade A are quite smooth, and only small-scale vortices are observed on the pressure side. But the pressure difference on blade A in the case c/R=0.60 is very large, causing a large negative vertical force on blade A, which is shown in figure 13c. Then, blade B is the main contributor to the total lift. On suction side of blade B, the three-vortex-structure and other scales are attached, which has a great impact on the pressure distribution. At this instant, blade B generates the downward lift, resulting in the negative lift of the rotating system. Meanwhile, because of the large pressure difference in the case c/R=0.375 (figure 15e), blade B has the largest negative vertical force compared with the other cases, causing the production of the largest negative lift of the rotating system. By comparing the two blades, it is concluded that blade B still generates most of the lift for the rotating system.

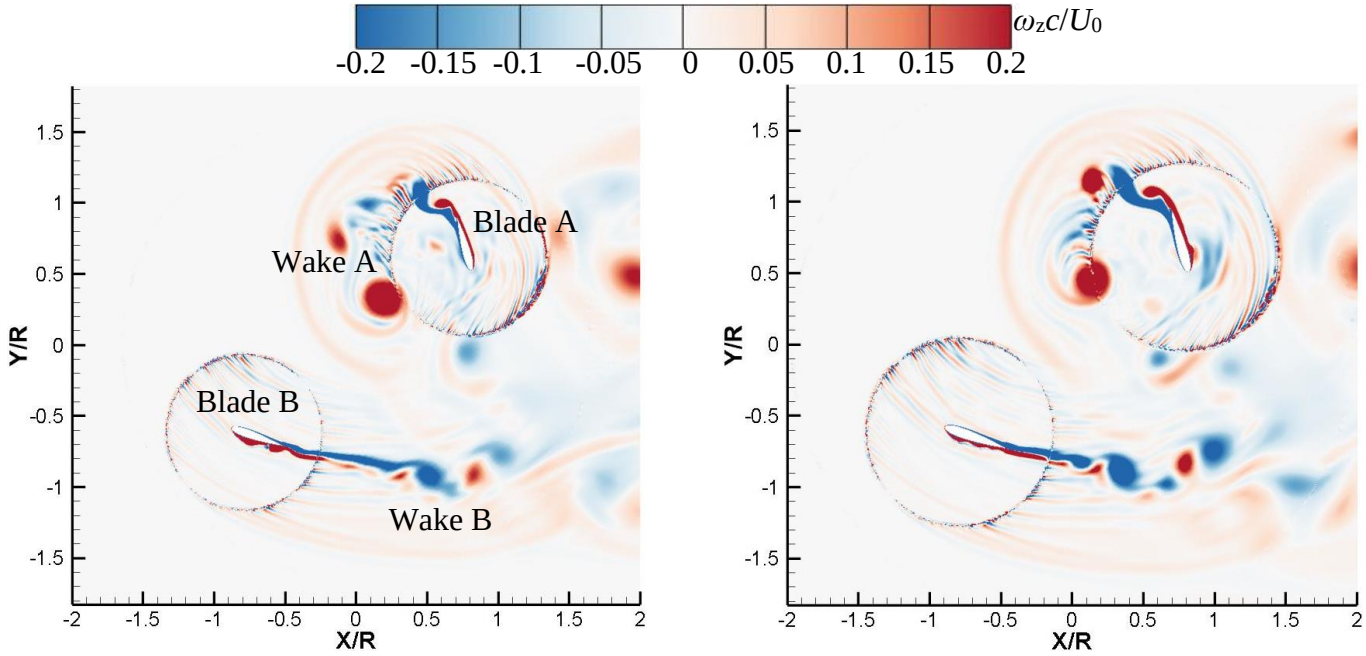
$\omega_z c/U_0$
-0.2 -0.15 -0.1 -0.05 0 0.05 0.1 0.15 0.2
Blade A
Wake A
Blade B
Wake B
Y/R
X/R

(a) (b)

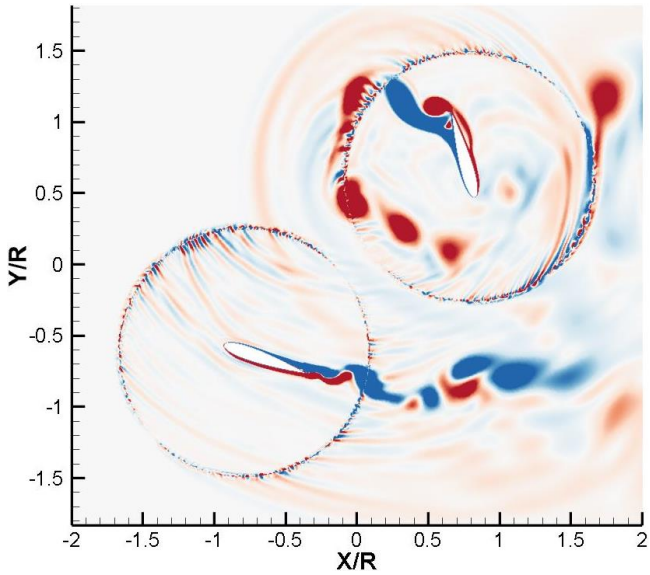
Y/R
X/R

(c)

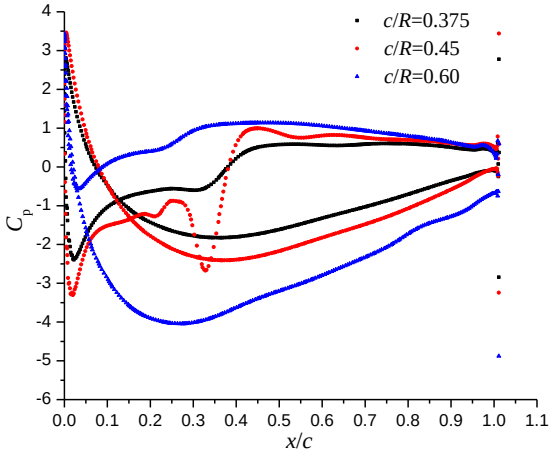
c/R=0.375
c/R=0.45
c/R=0.60
C_p
x/c

(d)

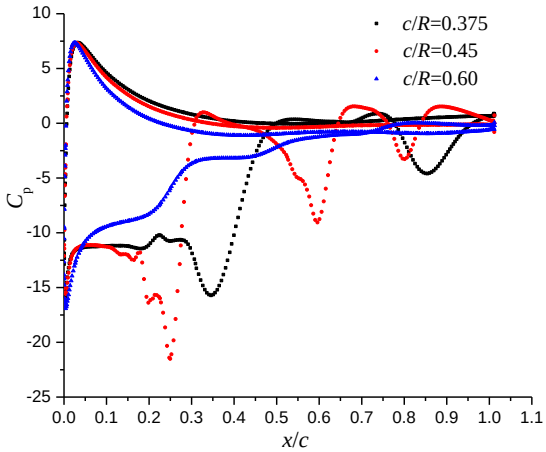
c/R=0.375
c/R=0.45
c/R=0.60
C_p
x/c

(e)

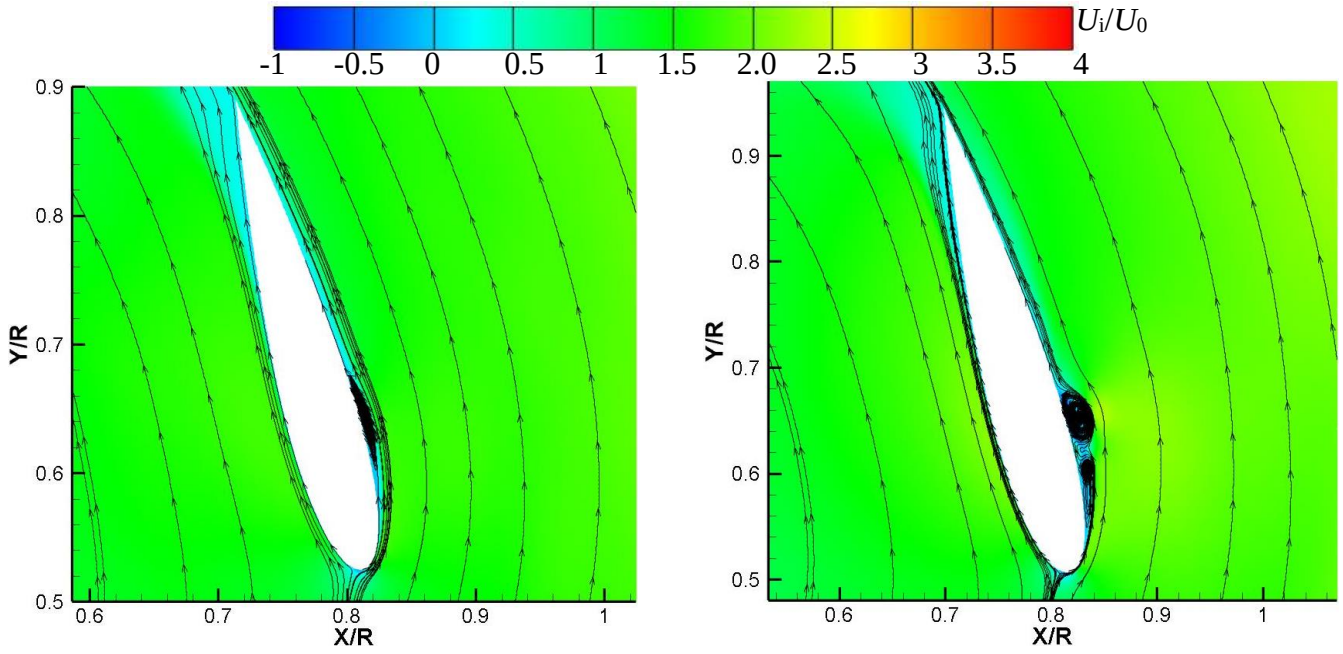
U_i/U_0
-1 -0.5 0 0.5 1 1.5 2.0 2.5 3 3.5 4
Y/R
X/R
0.5 0.6 0.7 0.8 0.9 1
0.5 0.6 0.7 0.8 0.9

(f) (g)

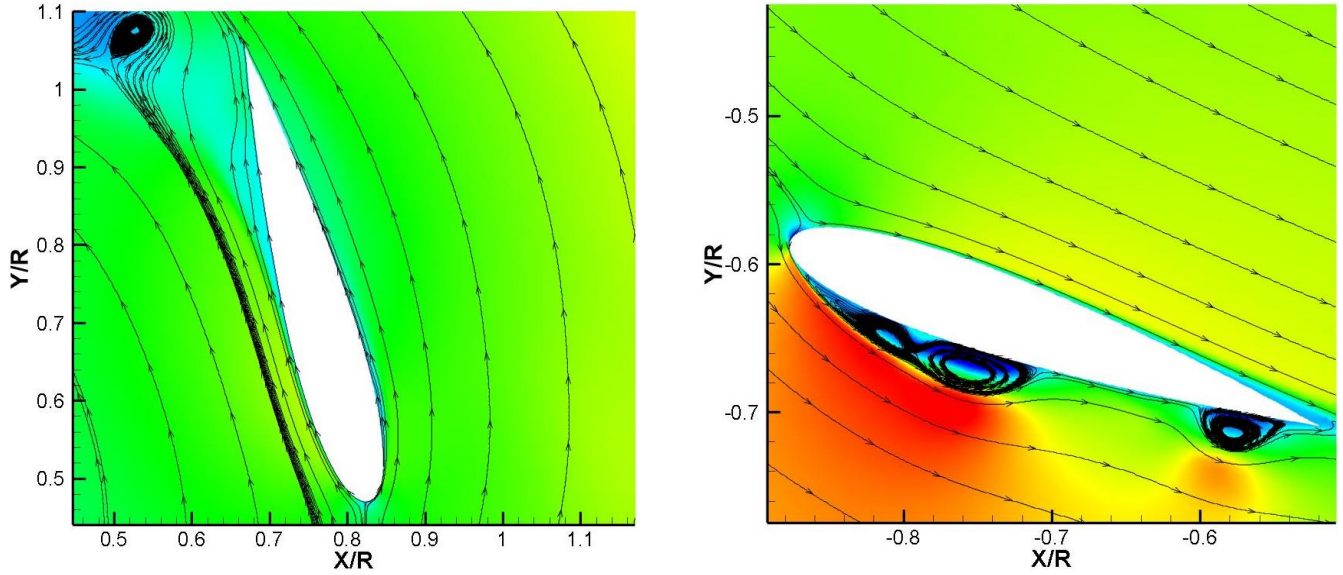
Y/R
X/R
0.5 0.6 0.7 0.8 0.9 1 1.1
0.5 0.6 0.7 0.8 0.9 1 1.1
-0.5 -0.6 -0.7
-0.8 -0.7 -0.6

(h) (i)

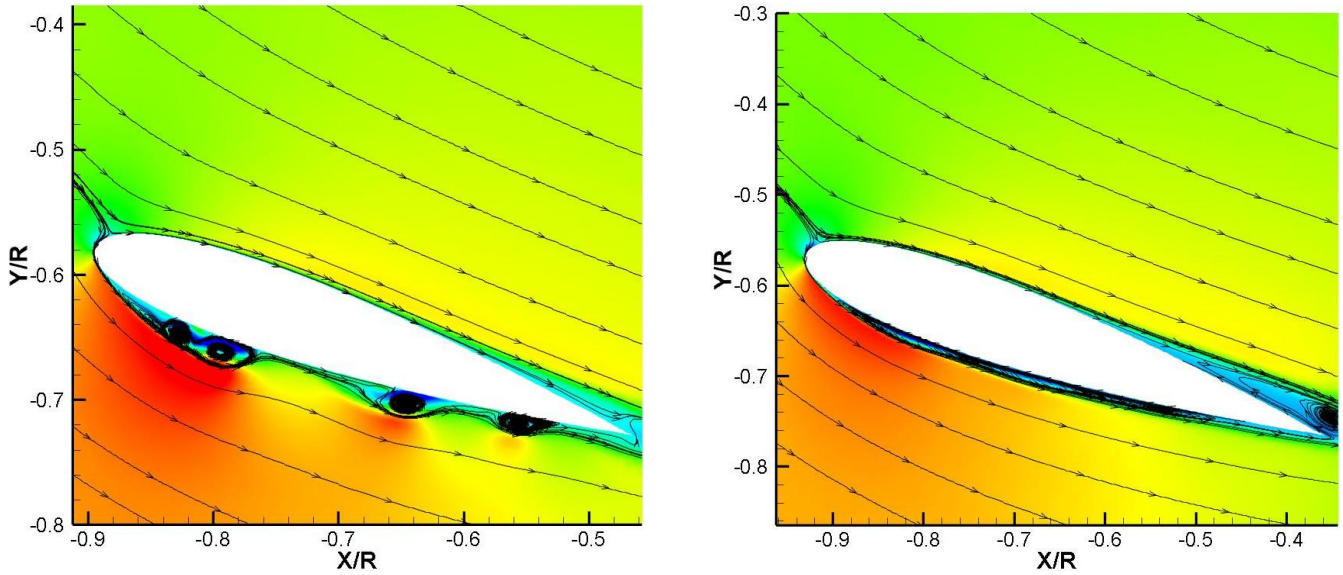

(j) (k)

Fig.15 Flow structures for various c/R at ψ=142°. (a) Global flow structure for c/R=0.375; (b) Global flow structure for c/R=0.45; (c) Global flow structure for c/R=0.60; (d) Pressure distribution of blade A; (e) Pressure distribution of blade B; (f) and (i) c/R=0.375; (g) and (j) c/R=0.45; (h) and (k) c/R=0.60.

In figure 16, the flow structures at positions ψ=160° (case c/R=0.6) and ψ=180° (cases c/R=0.375 and 0.45) are presented. Globally, the flows obtained with c/R=0.375 and 0.45 are extremely similar, as well as the pressure distribution and near-wall flow around blade A. However, the flow structures for the case c/R=0.60 differ from the other two cases, due to the different azimuthal angles. In figure 16c, wake A has already contacted with the leading edge of blade A and the wake B is more intense. Blade A generates the upward lift, which can produce the positive propulsive force, but its magnitude is quite similar in cases c/R=0.375 and 0.45, due to the pressure distribution in figure 16d. However, the attached vortex on the suction side of blade B has a great impact on the pressure, especially for the case c/R=0.375, leading to the larger propulsive force of the rotating system, compared with the case c/R=0.45. Thus, for these two cases, blade B is still dominant due to the influence of the large-scale vortex attached on the suction side.

For the case c/R=0.60 at ψ=160°, the high lift of the rotating system is mainly created by blade A, due to the large blade loading (figure 16d). Here, blade A is almost vertical, so the lift can provide the positive propulsive force. In addition, blade B can also produce the positive propulsive force as a consequence of the downward lift, but its magnitude is smaller than that the one given by blade A, as shown in 13d. For the single blade performance, the existence of the three-vortex -structure near the airfoil leading edge results in the low pressure and then the significant pressure recovery is observed after the reattachment. Afterwards, several small-size vortices bring about the pressure fluctuations, as shown figure 16e and 16k.

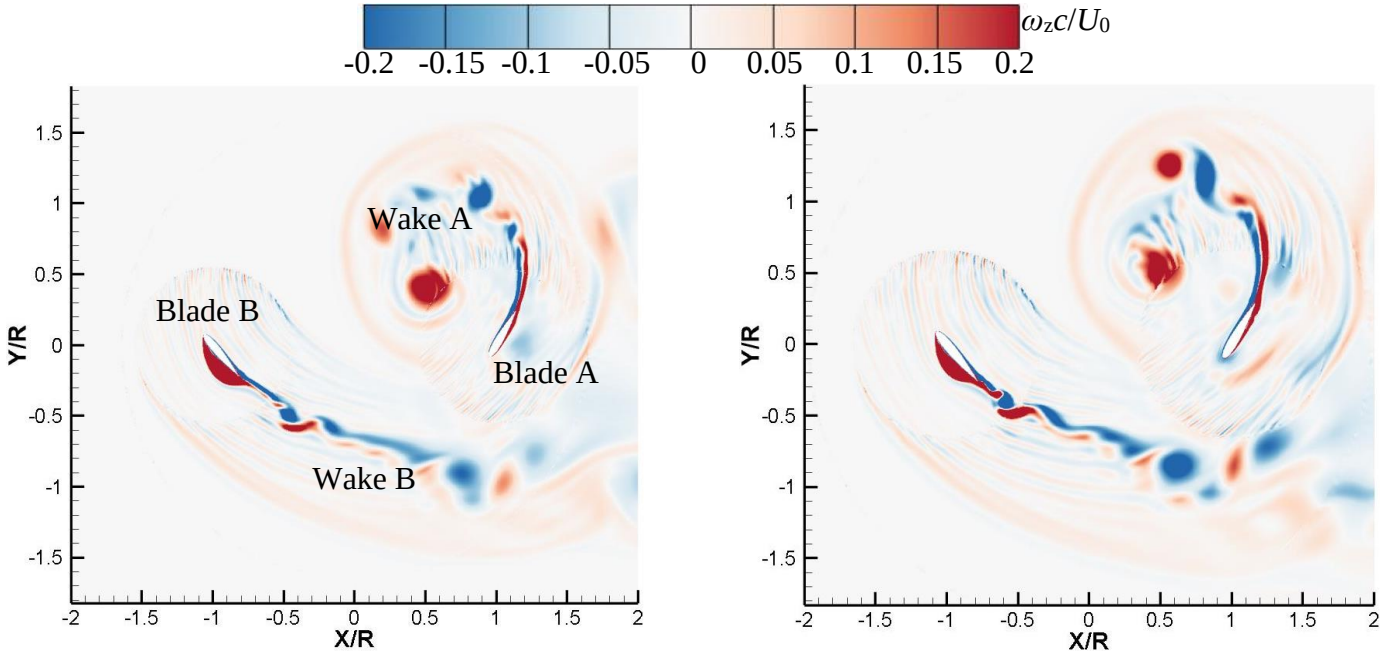
$\omega_z c/U_0$
-0.2 -0.15 -0.1 -0.05 0 0.05 0.1 0.15 0.2
Wake A
Blade B
Blade A
Wake B
Y/R
X/R

(a) (b)

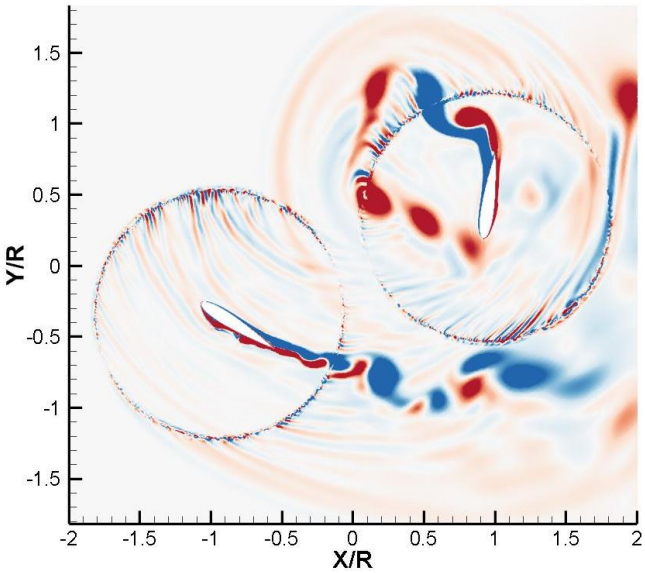
Y/R
X/R

(c)

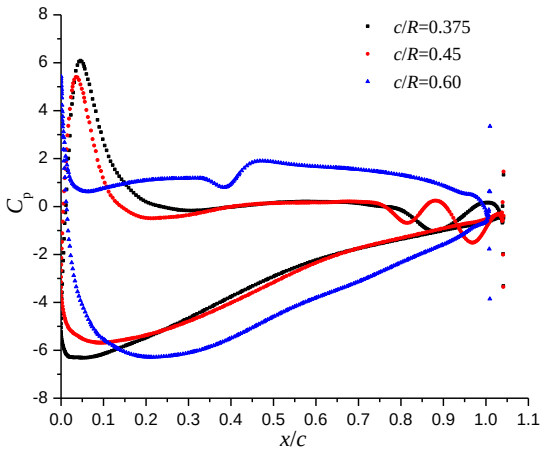
c/R=0.375
c/R=0.45
c/R=0.60
C_p
x/c

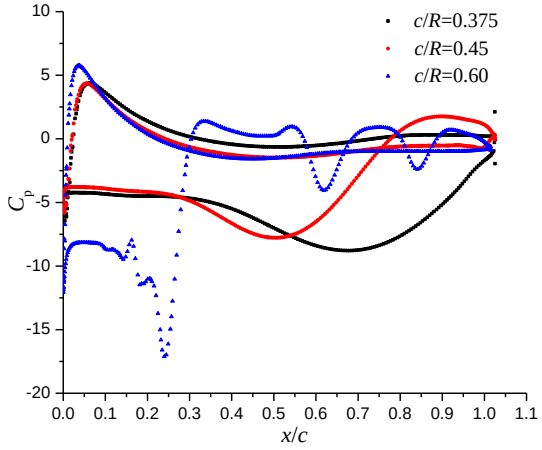
c/R=0.375
c/R=0.45
c/R=0.60
C_p
x/c

(d) (e)

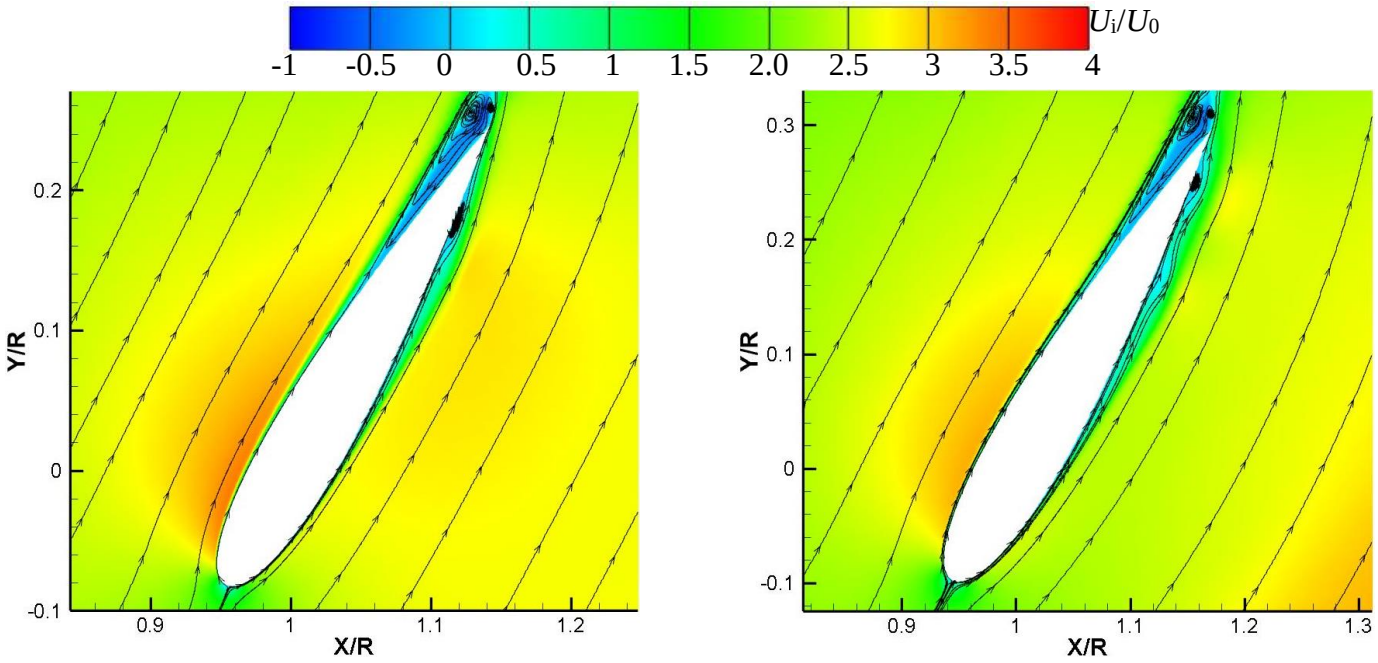
U_i/U_0
-1 -0.5 0 0.5 1 1.5 2.0 2.5 3 3.5 4
Y/R
X/R
0.2 0.1 0 -0.1
0.9 1 1.1 1.2
0.3 0.2 0.1 0 -0.1
0.9 1 1.1 1.2 1.3

(f) (g)

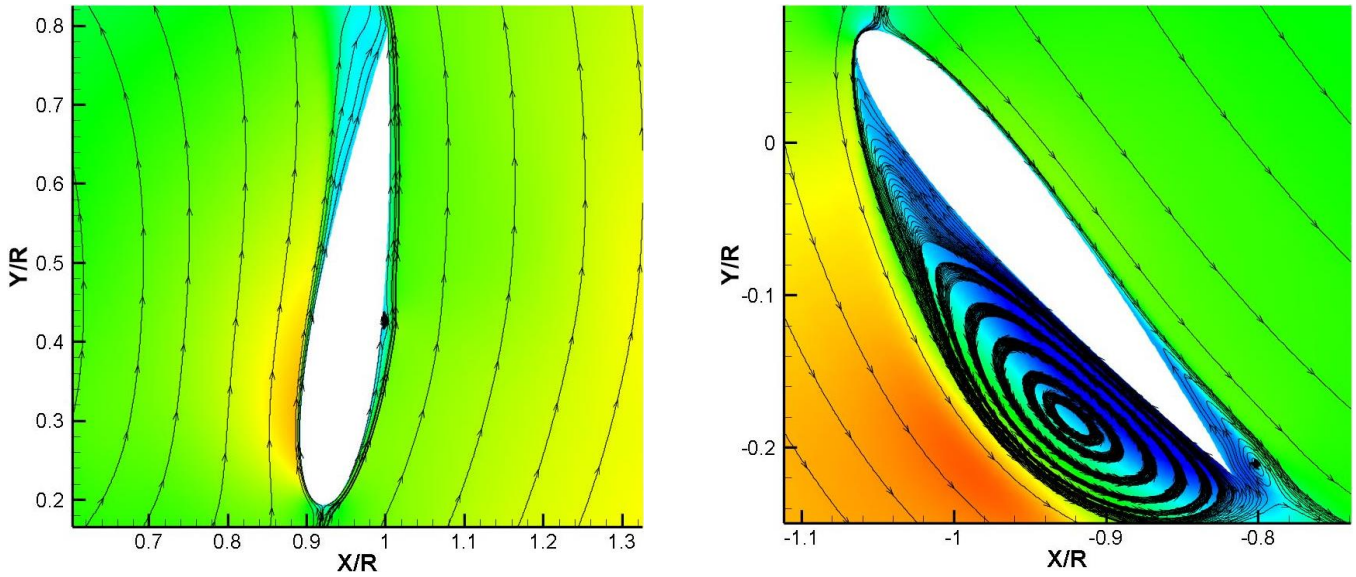
Y/R
X/R
0.8 0.7 0.6 0.5 0.4 0.3 0.2
0.7 0.8 0.9 1 1.1 1.2 1.3
0 -0.1 -0.2
-1.1 -1 -0.9 -0.8

(h) (i)

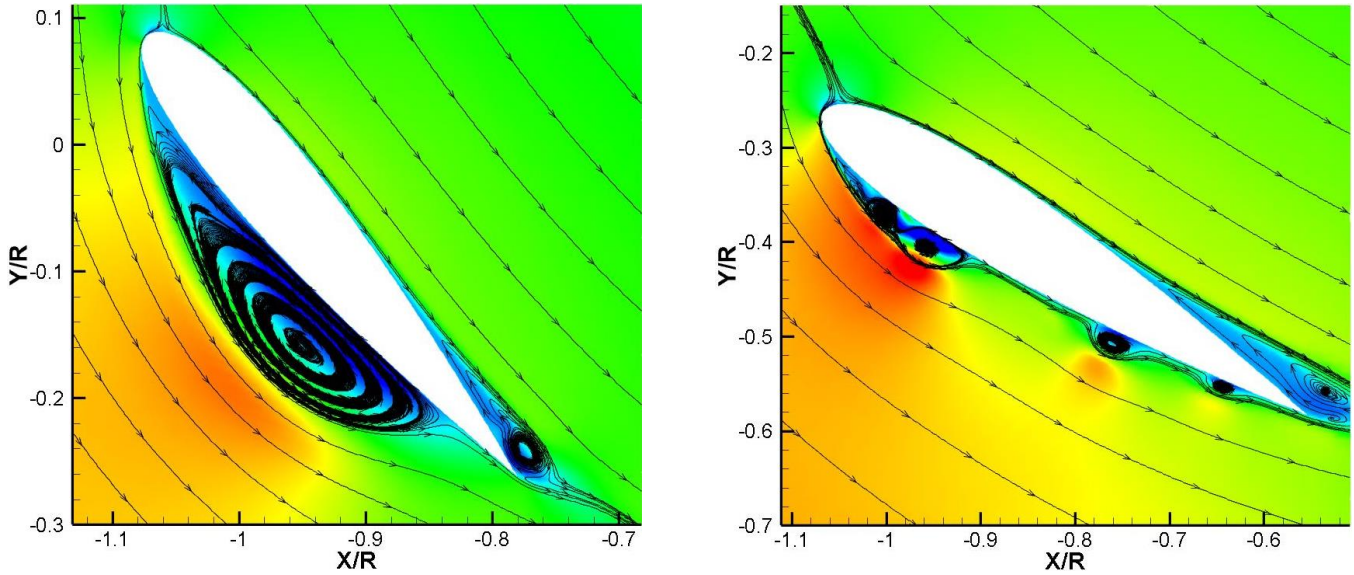

(j) (k)

Fig.16 Flow structures for various c/R at ψ=160° and 180°. (a) Global flow structure for c/R=0.375; (b) Global flow structure for c/R=0.45; (c) Global flow structure for c/R=0.60; (d) Pressure distribution of blade A; (e) Pressure distribution of blade B; (f) and (i) c/R=0.375; (g) and (j) c/R=0.45; (h) and (k) c/R=0.60.

3.2.2 Influence of the Reynolds number Re

The influence of the Reynolds number on the global performance is investigated at λ=0.52 by changing the inlet velocity and rotating speed. Figure 17 presents the performance curves at various *Re* for different c/R. When c/R is constant, the lift coefficient increases slowly with *Re*, while it is more obvious at a fixed *Re* as c/R increases. For the distribution of propulsive force coefficient, it seems that the highest values are obtained in cases with c/R=0.43, 0.45 and 0.47, especially at extremely low Reynolds number. The power coefficient in the case c/R=0.67 has the largest magnitude, leading to the lowest efficiency (figure 17d). Then, the power coefficient for the cases c/R=0.43, 0.45 and 0.47 decreases significantly with the Reynolds number. Consequently, the efficiency increases obviously with *Re* because of the slight decrease of the propulsive force coefficient.

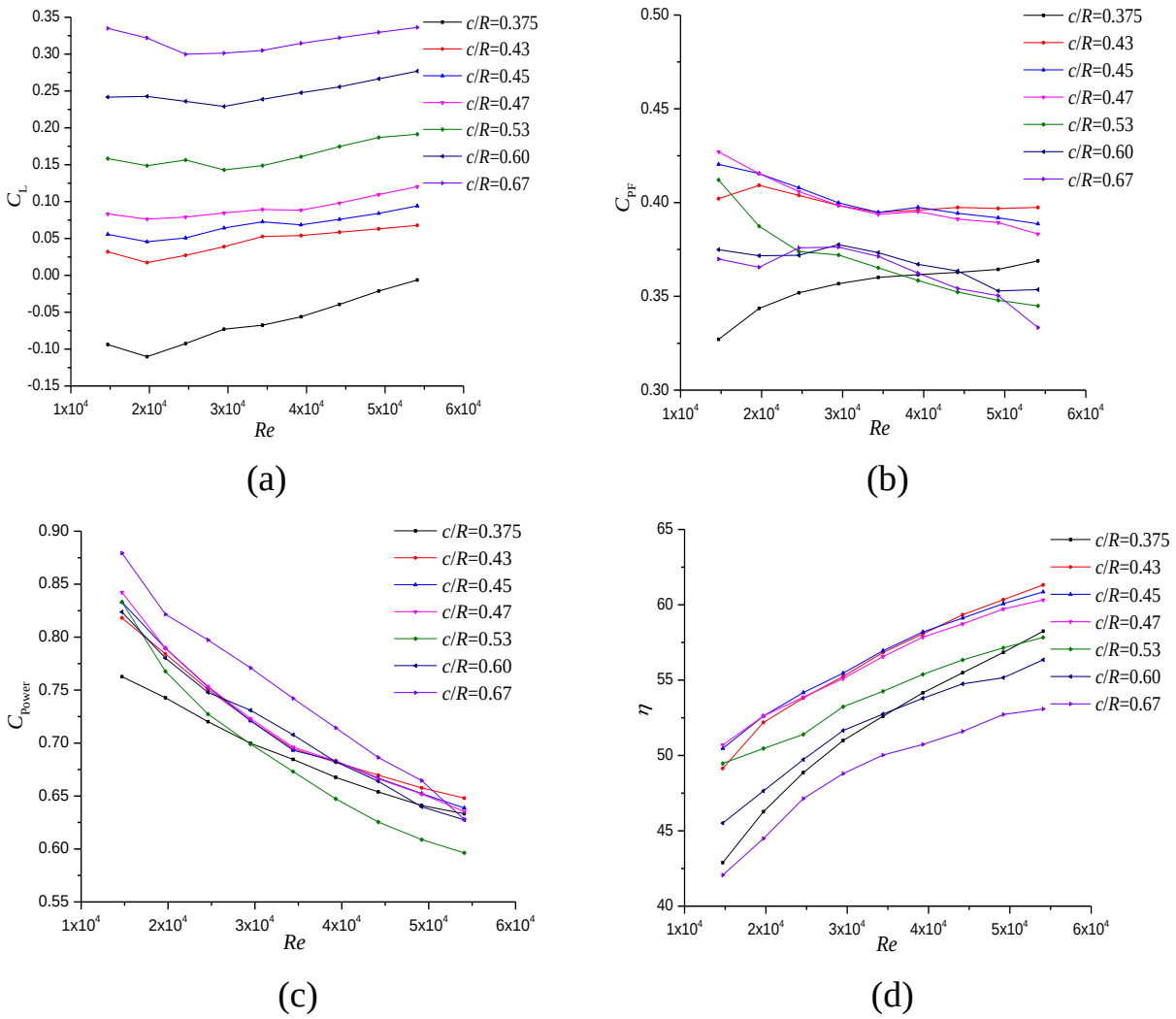

Fig.17 Performance curves at different *Re*. (a) Lift coefficient; (b) Propulsive force coefficient; (c) Power coefficient; (d) Efficiency.

In figure 18, three cases with c/R=0.45, at different Reynolds numbers, are selected to demonstrate the force difference generated by both the rotating system and the single blade. It can be seen that there is not much difference of lift coefficient between three cases during a cycle, but the propulsive force coefficient shows some differences at some positions. Evidently, the performance of the cycloidal rotor and single blade obtained at low *Re* is very different from the two other cases. Therefore, the lift coefficient at ψ=110° and the propulsive force coefficient at ψ=35° and 180°, are adopted to perform a deeper analysis of the flow structures.

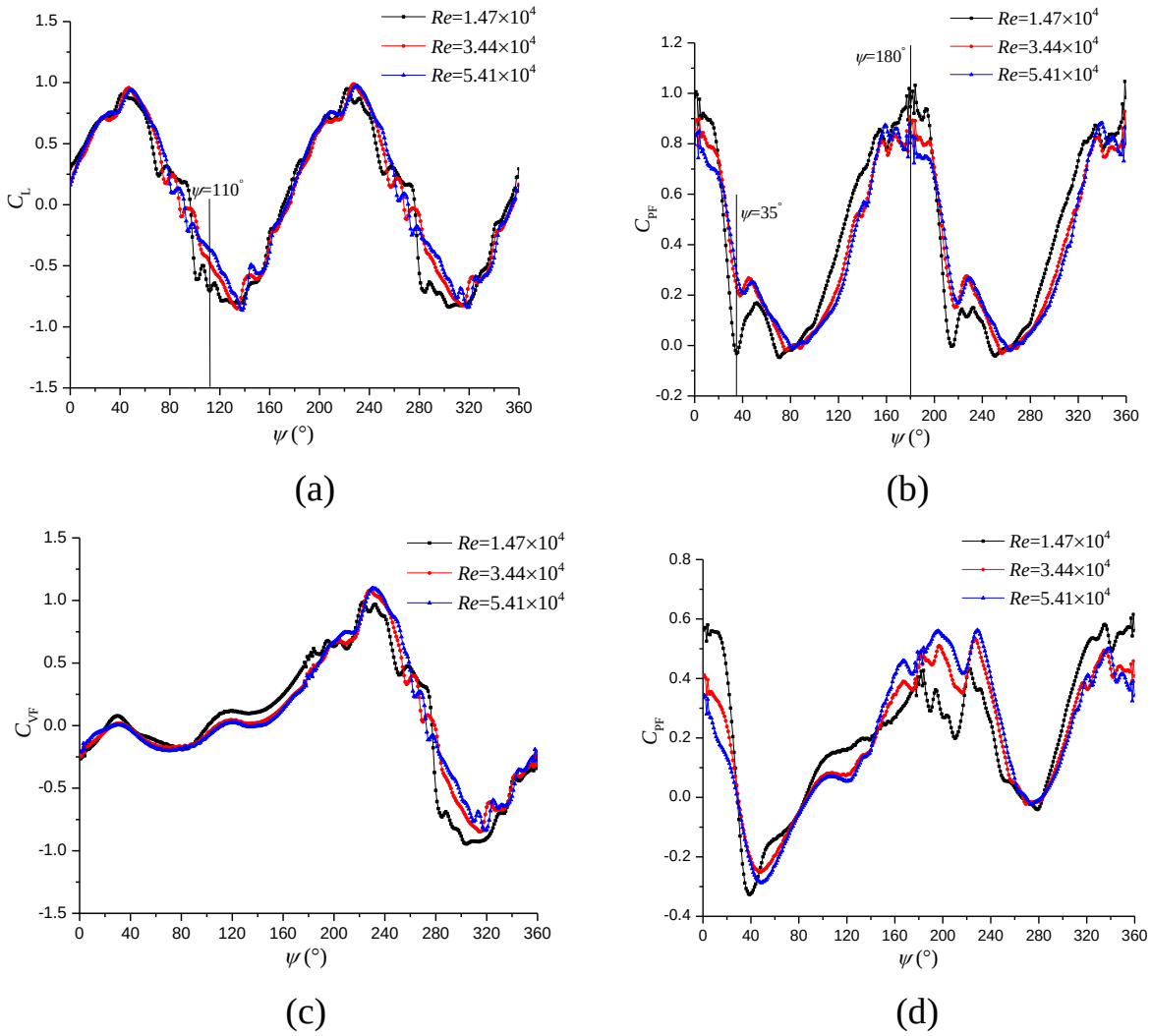

Fig.18 Performance curves at different *Re* in a revolution. (a) Lift coefficient of the rotating system; (b) Propulsive force coefficient of the rotating system; (c) Lift coefficient of single blade; (d) Propulsive force coefficient of single blade.

Figure 19 shows the flow structures at ψ=110° for cases at different *Re*. Inside the cycloidal rotor, the most noticeable event is the wake A-wake B interaction, which is stronger at high *Re*. The complicated vortical flows at large *Re* is responsible for the higher power consumption observed in figure 17 (the actual value of the power increases with *Re*). Then, at this position, the vertical force of blade A is very small, because of the small pressure difference (figure 19d) and the balance between the lift and drag components in the vertical direction. The flow on blade A is relatively smooth and the flow separation only occurs at the trailing edge on the suction side. Thus, it indicates that the lift of the rotating system is mainly generated by blade B because of the downward lift, especially for the case Re=1.47×10^4, due to the large pressure difference induced by the stagnation point location in figure 19e.

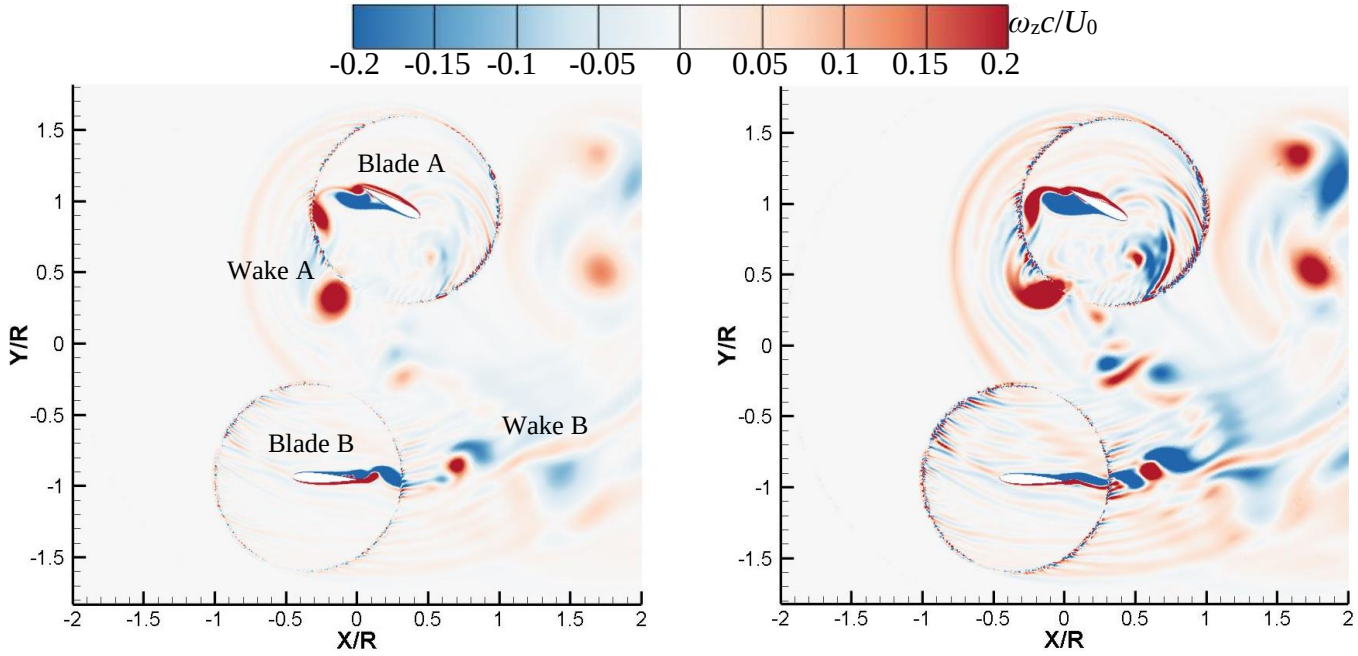
$\omega_z c/U_0$
-0.2 -0.15 -0.1 -0.05 0 0.05 0.1 0.15 0.2
Blade A
Wake A
Blade B
Wake B
Y/R
X/R

(a) (b)

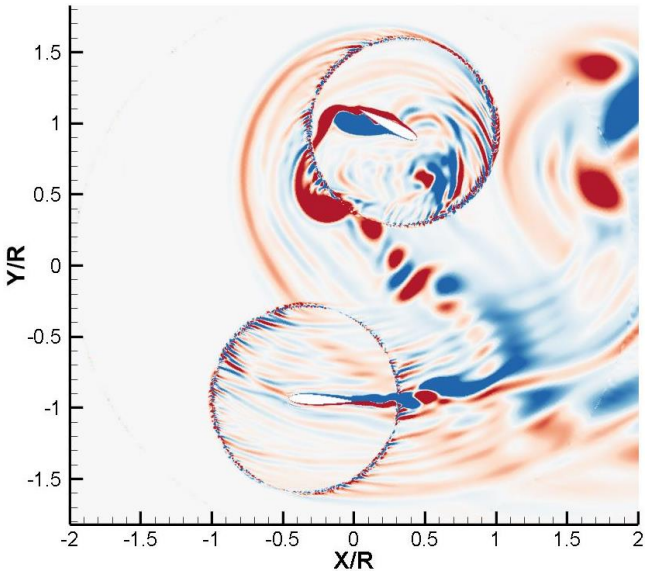
Y/R
X/R

(c)

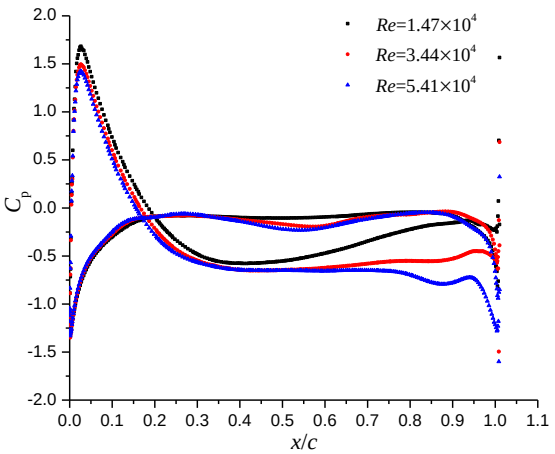
Re=1.47×10^4
Re=3.44×10^4
Re=5.41×10^4
C_p
x/c

(d)

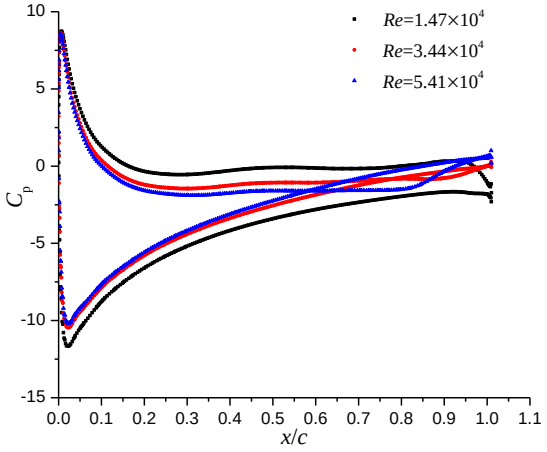
Re=1.47×10^4
Re=3.44×10^4
Re=5.41×10^4
C_p
x/c

(e)

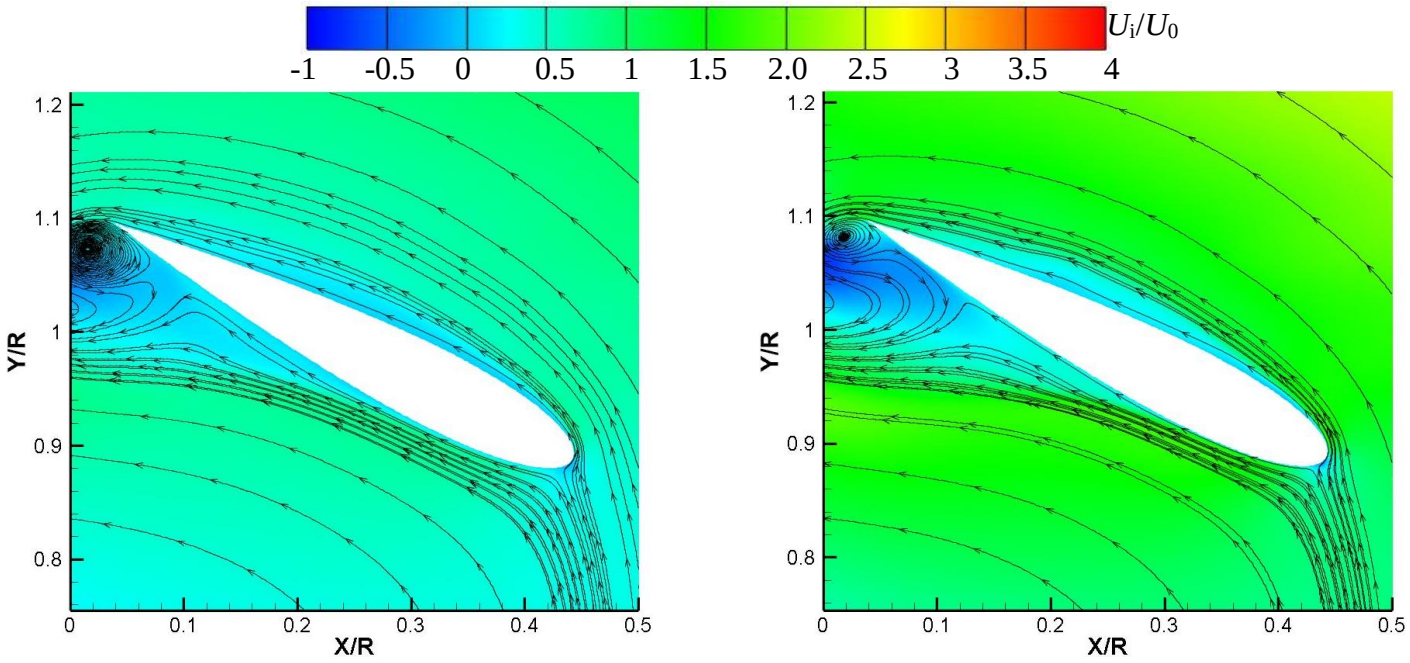

(f) (g)

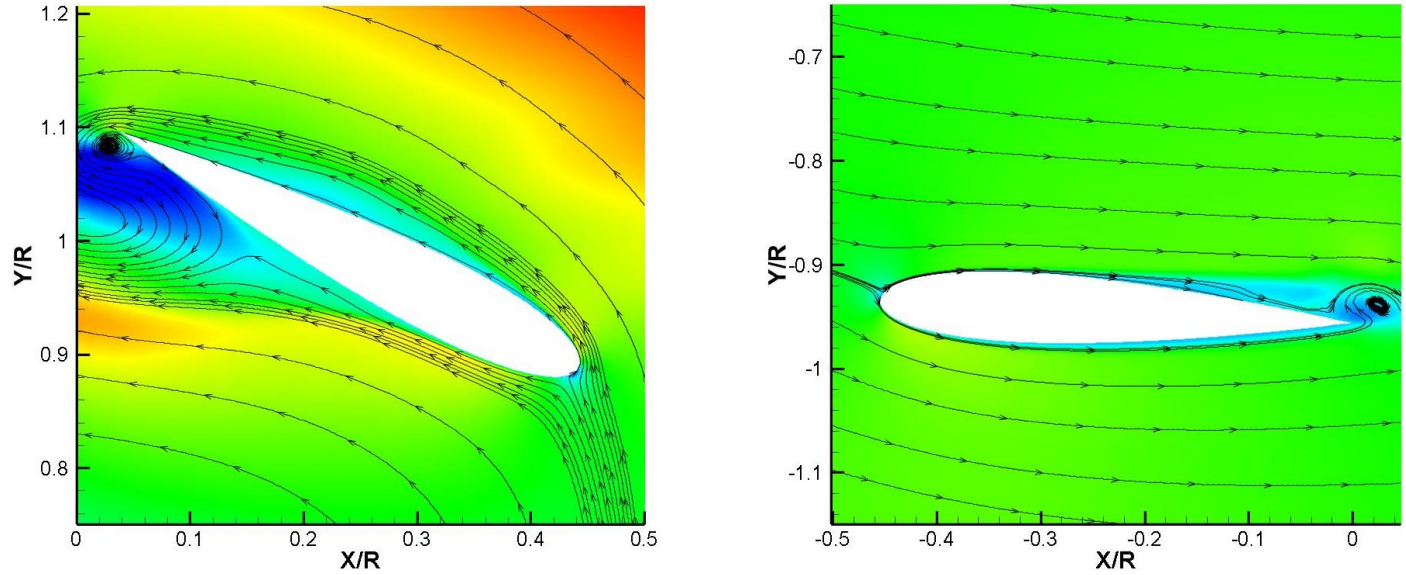

(h) (i)

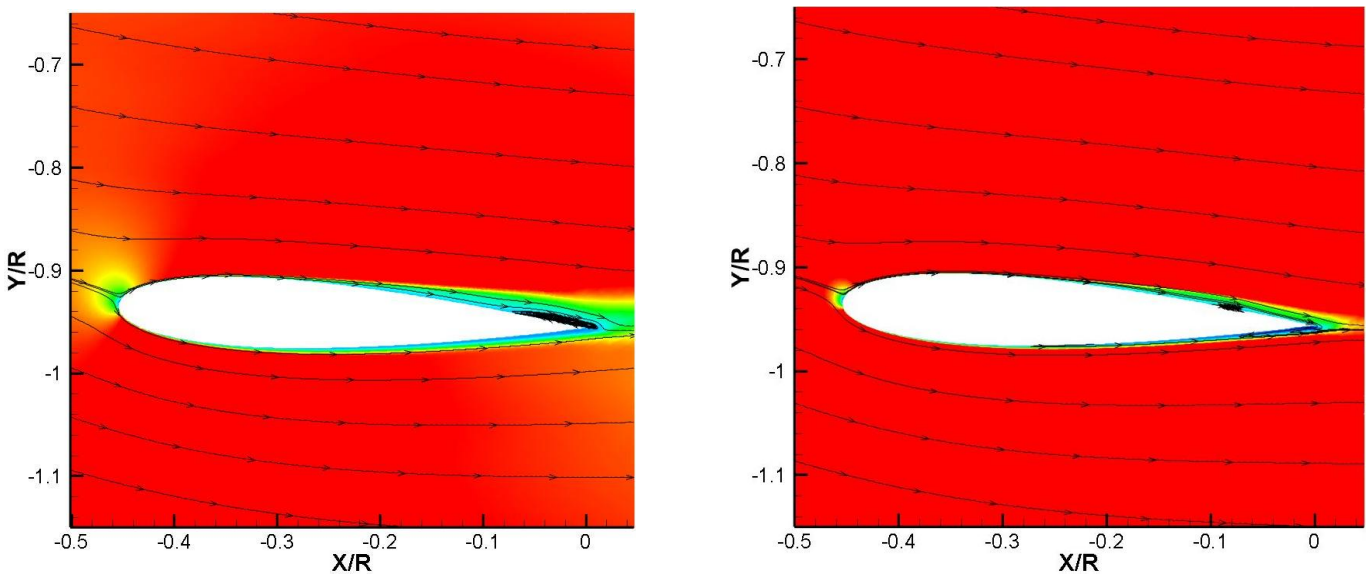

(j) (k)

Fig.19 Flow structures for various *Re* at ψ=110°. (a) Global flow structure at *Re*=1.47×10^4; (b) Global flow structure at *Re*=3.44×10^4; (c) Global flow structure at *Re*=5.41×10^4; (d) Pressure distribution of blade A; (e) Pressure distribution of blade B; (f) and (i) *Re*=1.47×10^4; (g) and (j) *Re*=3.44×10^4; (h) and (k) *Re*=5.41×10^4.

At position ψ=35°, the global propulsive force coefficient for the cases *Re*=3.44×10^4 and 5.41×10^4 is almost the same, but not anymore when the Reynolds number is 1.47×10^4. Consequently, the flow structures are displayed in figure 20. At this position, wake A has a high risk of colliding with the leading edge of blade B, especially at high *Re*. Simultaneously, wake B rolls up, resulting in the wake B-wake B interaction. Then, on the pressure side of blade A, a large-scale separation vortex is attached at *Re*=1.47×10^4, but it splits into two connecting vortices when *Re* increases. After the reattachment point, the pressure recovery is obvious at low *Re*. Simultaneously, the flow separation at the trailing edge on the suction side, has a great effect on the pressure, resulting in the large pressure difference at low *Re*. As a result, the large amplitude upward lift is generated on blade A, producing the negative propulsive force. For blade B, the upward lift towards the suction side creates a positive propulsive force, but the magnitude is relatively small at low *Re*, because of the blade loading (figure 20e). Finally, by the combination of two blades, it concludes that the total propulsive force obtained at *Re*=1.47×10^4 is the smallest, compared with that of two other cases.

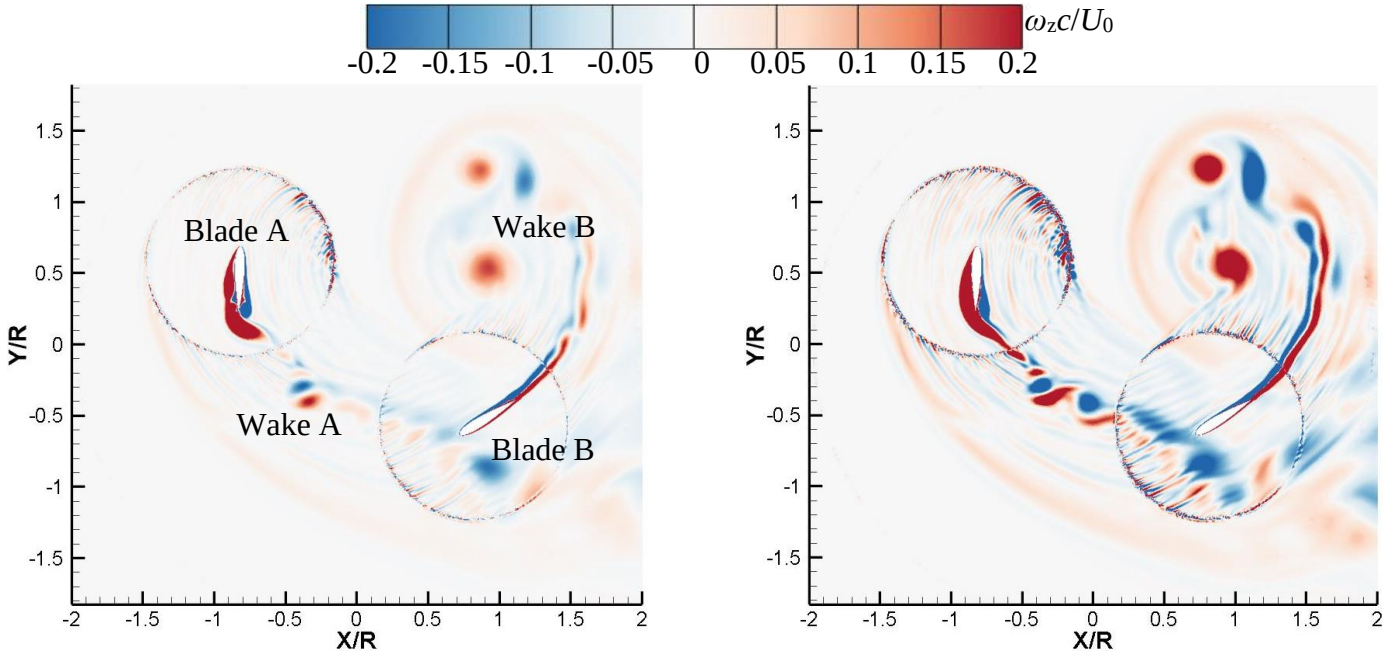
$\omega_z c/U_0$
-0.2 -0.15 -0.1 -0.05 0 0.05 0.1 0.15 0.2
Blade A
Wake B
Wake A
Blade B
Y/R
X/R

(a) (b)

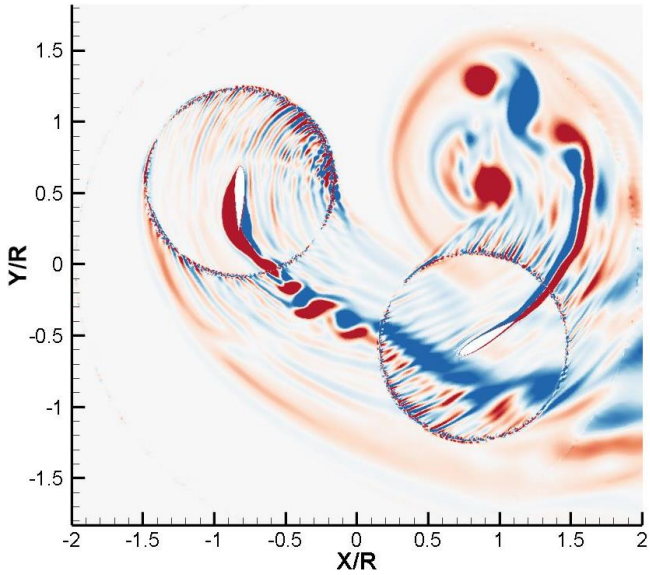
Y/R
X/R

(c)

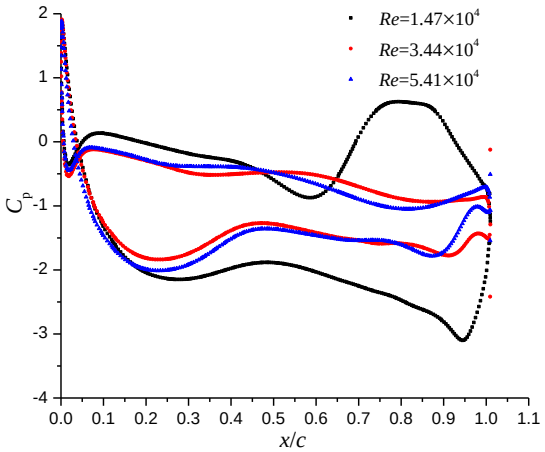
Re=1.47×10^4
Re=3.44×10^4
Re=5.41×10^4
C_p
x/c

(d)

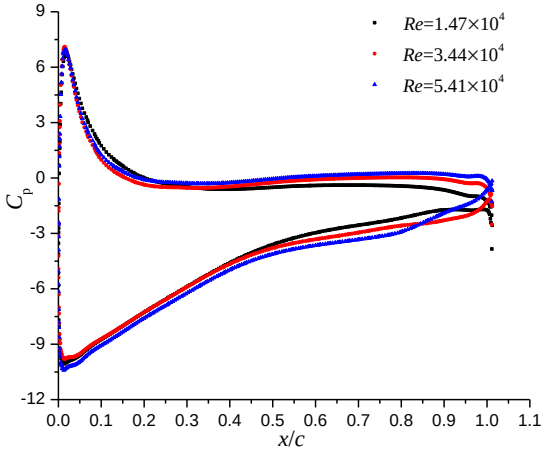
Re=1.47×10^4
Re=3.44×10^4
Re=5.41×10^4
C_p
x/c

(e)

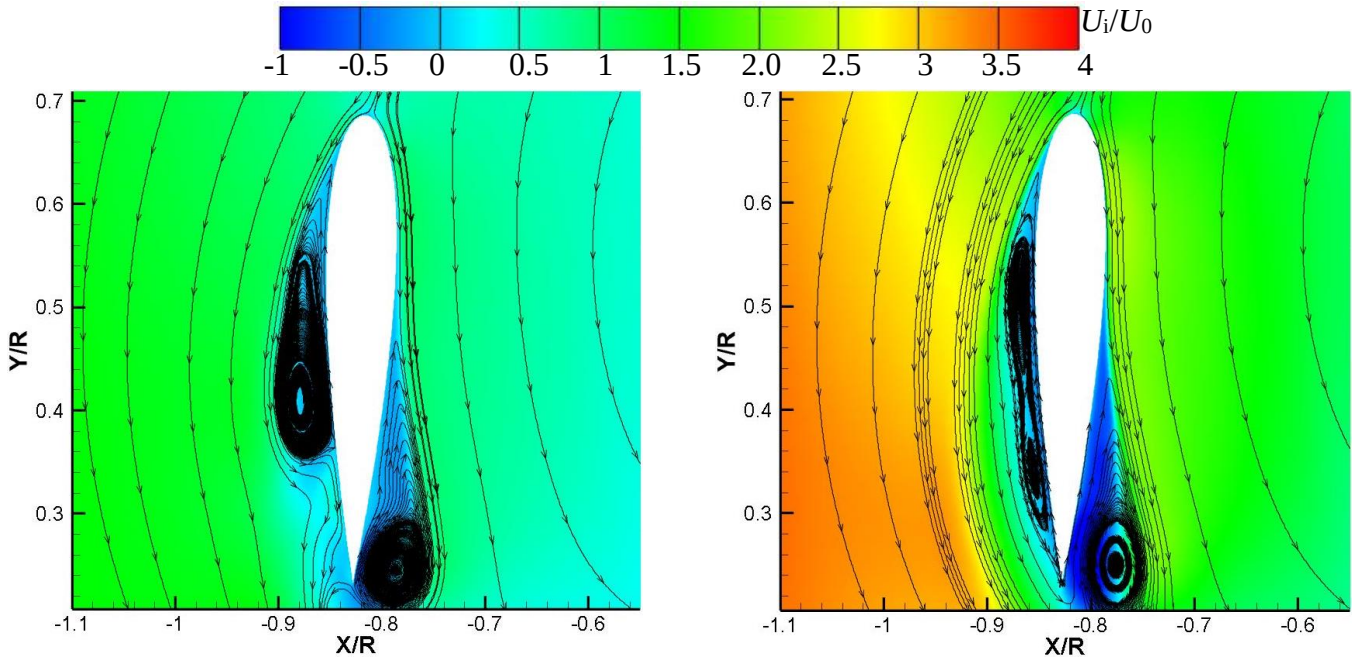
U_i/U_0
-1 -0.5 0 0.5 1 1.5 2.0 2.5 3 3.5 4
Y/R
X/R
0.7 0.6 0.5 0.4 0.3
-1.1 -1 -0.9 -0.8 -0.7 -0.6

(f) (g)

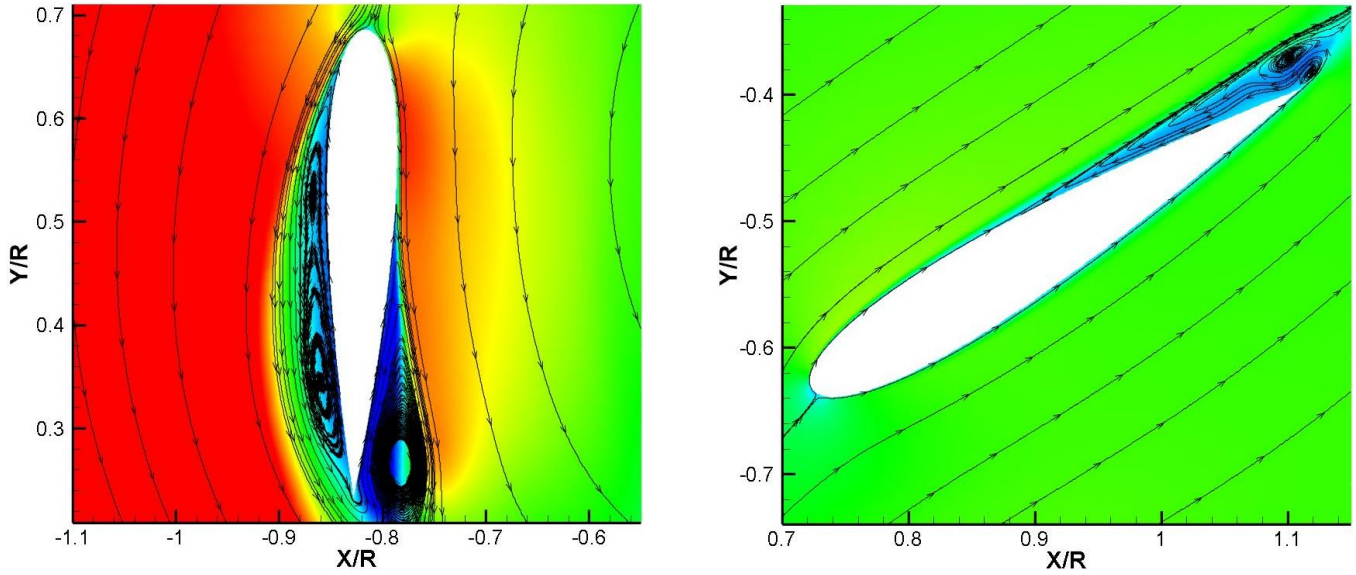
Y/R
X/R
0.7 0.6 0.5 0.4 0.3
-1.1 -1 -0.9 -0.8 -0.7 -0.6
-0.4 -0.5 -0.6 -0.7
0.7 0.8 0.9 1 1.1

(h) (i)

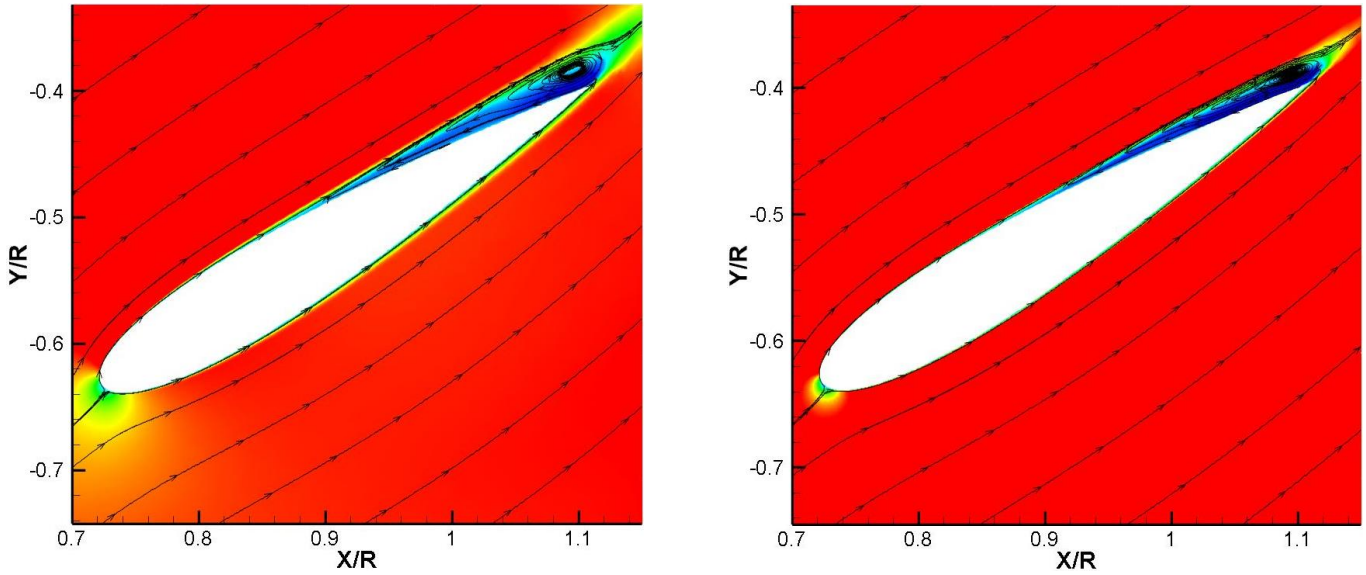

(j) (k)

Fig.20 Flow structures for various *Re* at ψ=35°. (a) Global flow structure at *Re*=1.47×10^4; (b) Global flow structure at *Re*=3.44×10^4; (c) Global flow structure at *Re*=5.41×10^4; (d) Pressure distribution of blade A; (e) Pressure distribution of blade B; (f) and (i) *Re*=1.47×10^4; (g) and (j) *Re*=3.44×10^4; (h) and (k) *Re*=5.41×10^4.

When approaching the position ψ=180°, the two blades change the initial position each other. The global propulsive force obtained with various Reynolds numbers has a positive peak, but it is the largest for *Re*=1.47×10^4. Therefore, the flow filed is shown in figure 21. At high Reynolds number, the flow is more disordered, characterized by the complex shedding in the wake of the two blades and wake A-blade A interaction. Although there is flow separation near the trailing edge on blade A at *Re*=1.47×10^4 and 3.44×10^4, the blade loadings are nearly the same for the three cases (figure 21d). Thus, the predicted propulsive force generated by blade A is quite the same at three *Re* in figure 18d. However, the flow pattern over the suction side of blade B is different in the three cases, especially at low *Re*, when three distinct vortex structures attach on the suction side, leading to the very low pressure, as shown in figure 21e. Hence, the downward lift generated by blade B is responsible for the large value of the positive propulsive force. Finally, the propulsive force of the rotating system is the largest at low *Re*.

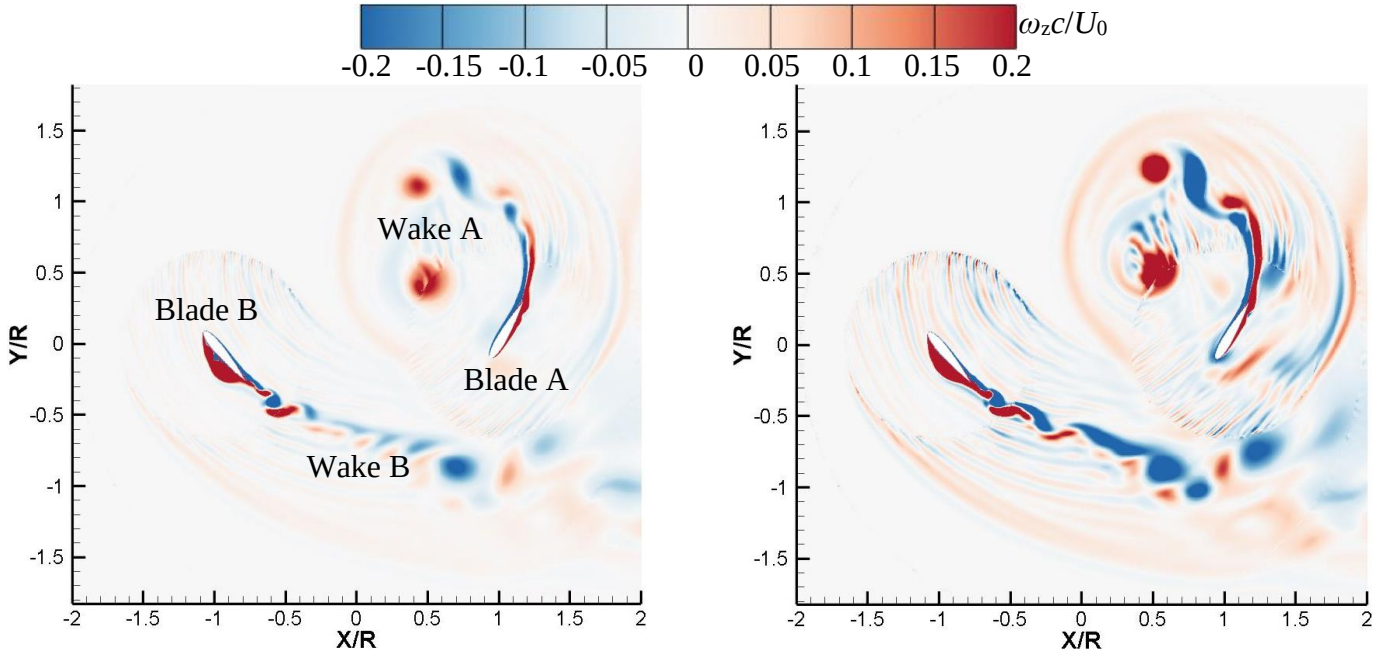
$\omega_z c/U_0$
-0.2 -0.15 -0.1 -0.05 0 0.05 0.1 0.15 0.2
Wake A
Blade B
Blade A
Wake B
Y/R
X/R

(a) (b)

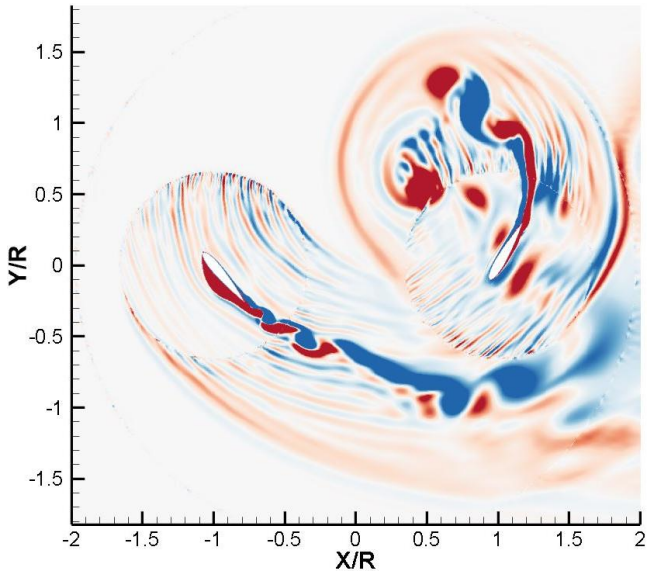
Y/R
X/R

(c)

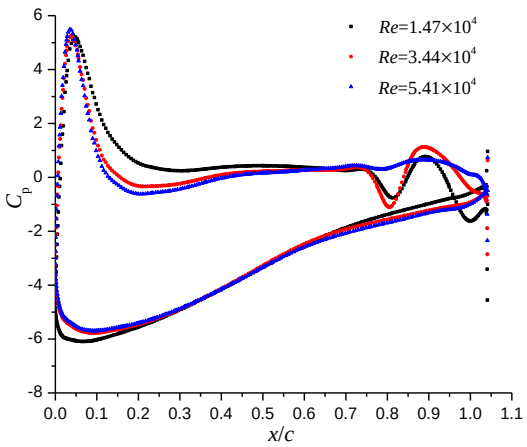
Re=1.47×10^4
Re=3.44×10^4
Re=5.41×10^4
C_p
x/c

(d)

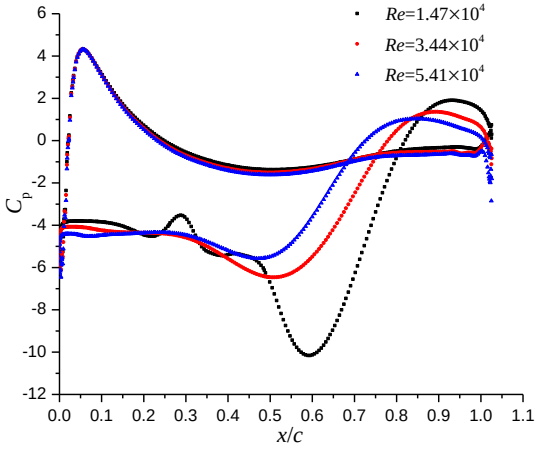
Re=1.47×10^4
Re=3.44×10^4
Re=5.41×10^4
C_p
x/c

(e)

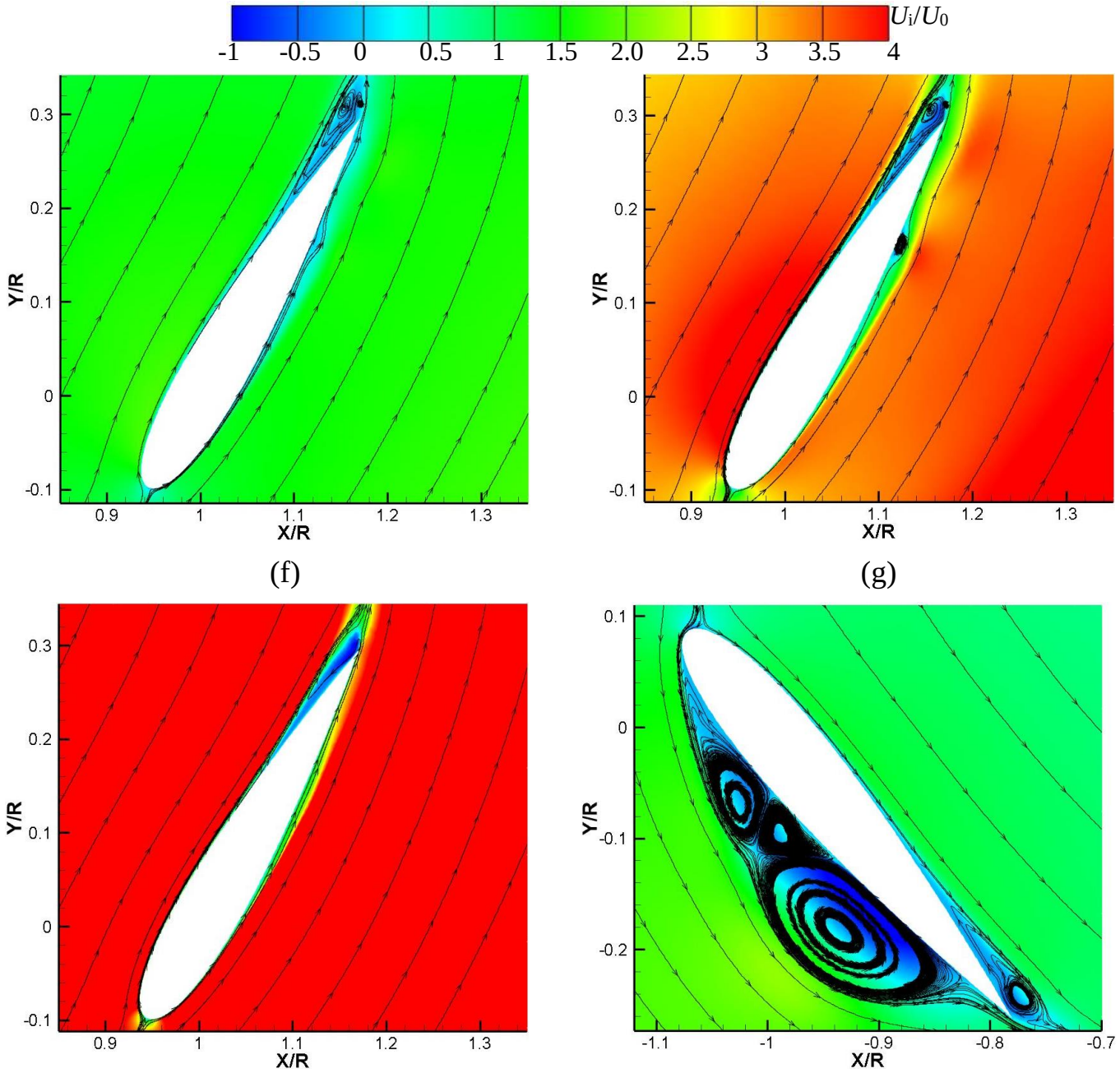
U_i/U_0
-1 -0.5 0 0.5 1 1.5 2.0 2.5 3 3.5 4
Y/R
X/R
0.3 0.2 0.1 0 -0.1
0.9 1 1.1 1.2 1.3
(f)
(g)
(h)
(i)
-1.1 -1 -0.9 -0.8 -0.7
-0.2

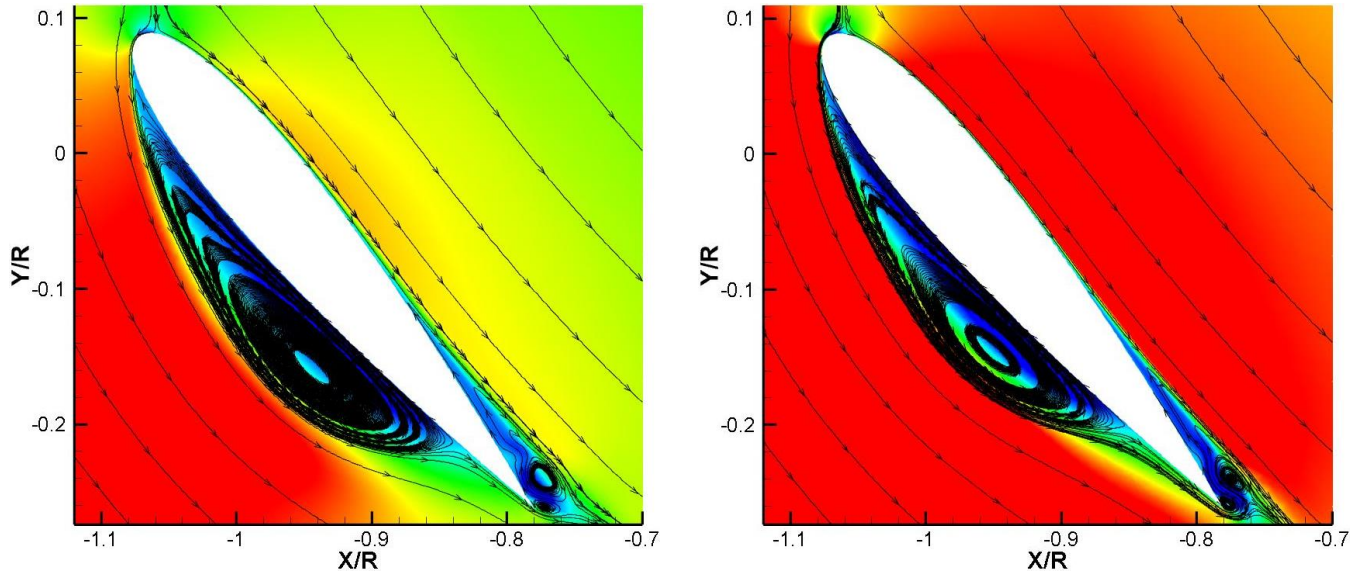

(j) (k)

Fig.21 Flow structures for various *Re* at ψ=180°. (a) Global flow structure at Re=1.47×10^4; (b) Global flow structure at Re=3.44×10^4; (c) Global flow structure at Re=5.41×10^4; (d) Pressure distribution of blade A; (e) Pressure distribution of blade B; (f) and (i) Re=1.47×10^4; (g) and (j) Re=3.44×10^4; (h) and (k) Re=5.41×10^4.

3.2.3 Influence of the advance coefficient λ

The influence of the advance coefficient λ on the performance and the flow structures for different c/R is discussed in the following section only by changing the rotating speed. The performance curves are plotted in figure 22. For a fixed c/R, the lift coefficient decreases with the increase of λ, while it increases with c/R at a constant λ. The propulsive force and power coefficients show the same trend, i.e. a decrease when λ increases, but it only slightly depends on c/R. The efficiency exhibits a slight increase initially and then decreases dramatically with the increase of λ, which indicates that the decrease rate of the propulsive force is larger than the power. Generally, it is observed that the best efficiency is achieved around λ=0.45 for the case c/R=0.45.

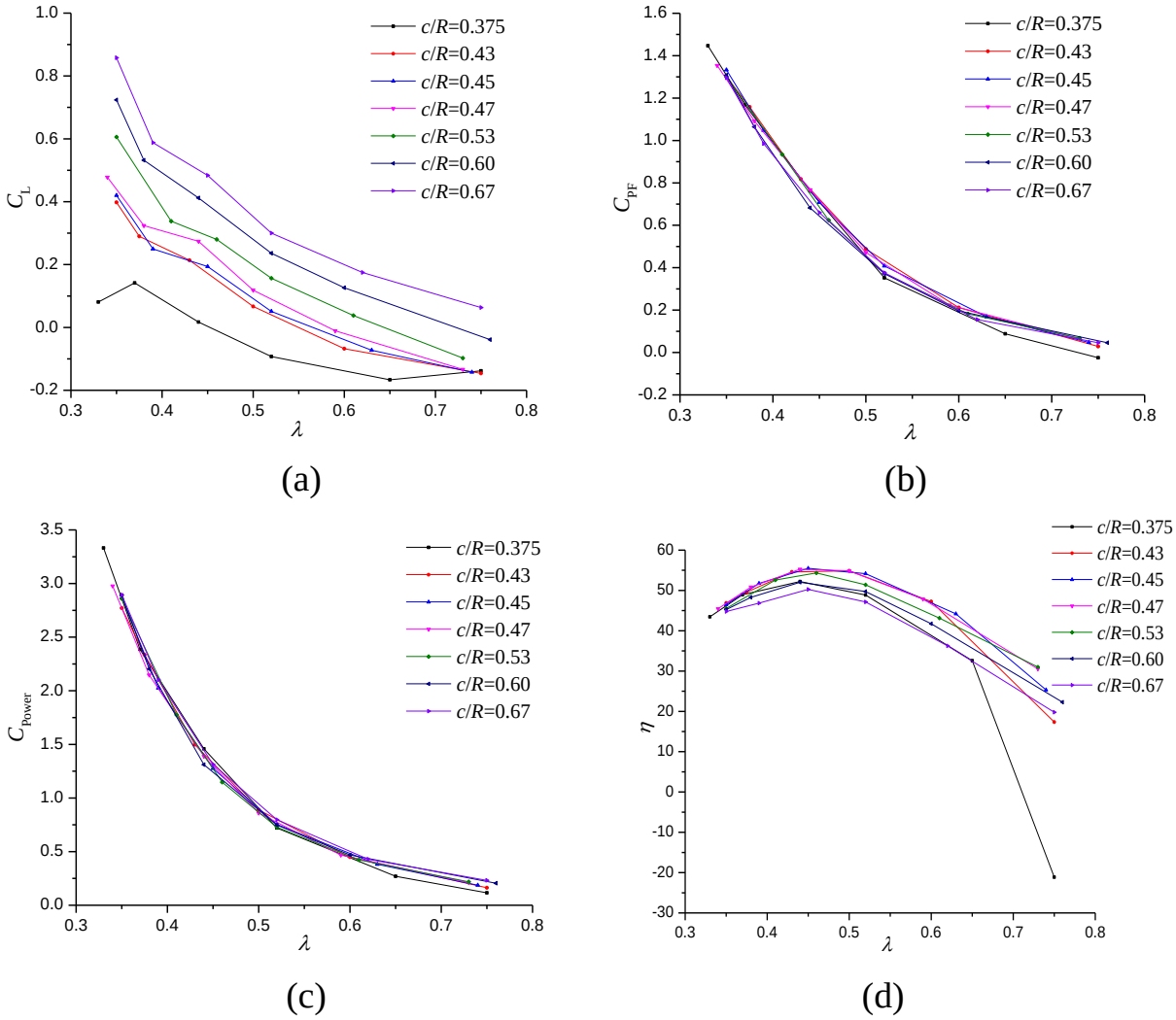

Fig.22 Performance curves at different λ. (a) Lift coefficient; (b) Propulsive force coefficient; (c) Power coefficient; (d) Efficiency.

The performance curves of both the rotating system and single blade are displayed in figure 23, to investigate their differences for three λ. Compared with the Reynolds number effect, it seems that the influence of λ is more obvious. Actually, both λ and *Re* depends on the rotating speed, based on the definition of *Re*. However, the influence of *Re* on the performance is very small, except when *Re* is smaller than 1.47×10^4, which is observed in section 3.2.2. The *Re* in the tested cases in this section is much larger than 1.47×10^4. Based on the following figures, it is observed that both the lift and propulsive force coefficients are much larger at low λ caused by the large rotating speed. Additionally, the performance curves of the rotating system and single blade vary considerably during a cycle. Thus, two positions, ψ=45° and 135°, are selected to study the flow structures when the lift coefficient has a positive and negative peak, respectively, while the azimuthal angle of 12° is used to clarify the difference of the propulsive force coefficient.

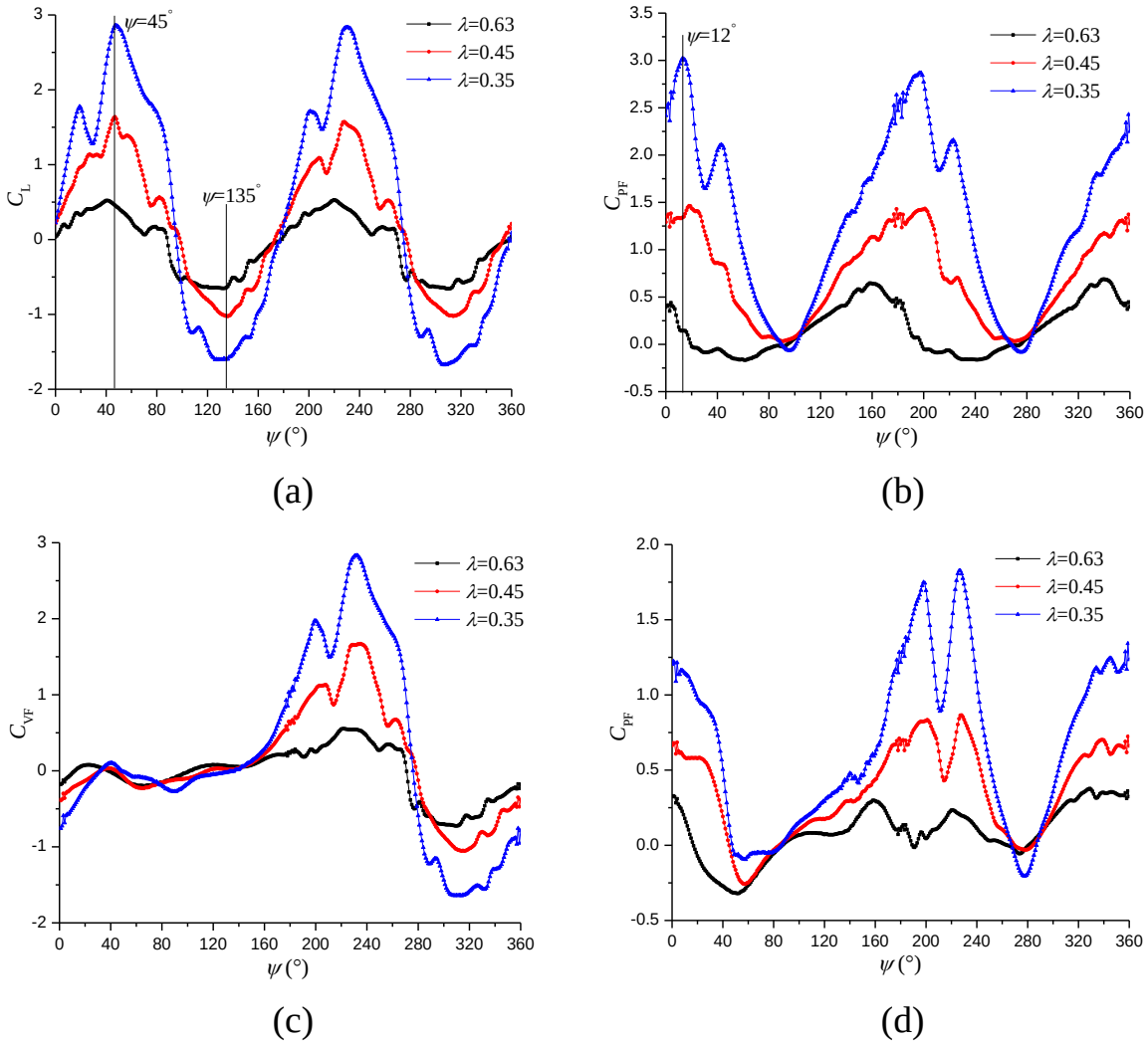

Fig.23 Performance curves at different λ in a revolution. (a) Lift coefficient of the rotating system; (b) Propulsive force coefficient of the rotating system; (c) Lift coefficient of single blade; (d) Propulsive force coefficient of single blade.

The flow structures and pressure distributions on the two blades are presented in figure 24 at three λ. At ψ=45°, the lift coefficient of the rotating system has a positive peak. At low λ, the flow field is more complex due to the large rotating speed and there is a clear wake A-blade B interaction. Besides, at high λ, the wake B also interacts with itself, because it has enough time to contact because of the low rotating speed. On the left side of blade A, there is a large flow separation vortex near the leading edge. After that, the flow reattaches and then a vortex structure appears near the trailing edge, which becomes weaker when λ decreases. Further decreasing the rotating speed makes the vortex structures nearly disappear. This phenomenon is mainly caused by the stagnation point location. For an instance, at high λ, the stagnation point is located on the left side, leading to the relatively smooth near-wall flows. Although the attached vortex flows at λ=0.35 modify the pressure obviously, as shown in figure 24d, the vertical force of blade A is almost the same for three

cases. This is due to the balance of the lift and drag components in the vertical direction and the small pressure difference produced by blade A.

On the suction side of blade B, at λ=0.35, a LSB is observed near the leading edge. Then, after the reattachment location, the flow separation occurs near the trailing edge, leading to the slight decrease of the pressure. With the increase of λ, the flow on the suction side of blade B becomes gradually smoother. From the distribution of pressure in figure 24e, combined with the velocity contours, it seems that the stagnation point location is the main source for the pressure distribution on both sides, which is due to the change of the relative velocity caused by the change of the rotating speed. The blade B can produce the upward lift, resulting in the generation of positive vertical force. And the drag can also create the positive vertical force, so the rotating system has the largest positive lift at λ=0.35. Finally, the conclusion is that blade B is responsible for the lift difference of the rotating system, mainly caused by the stagnation point location.

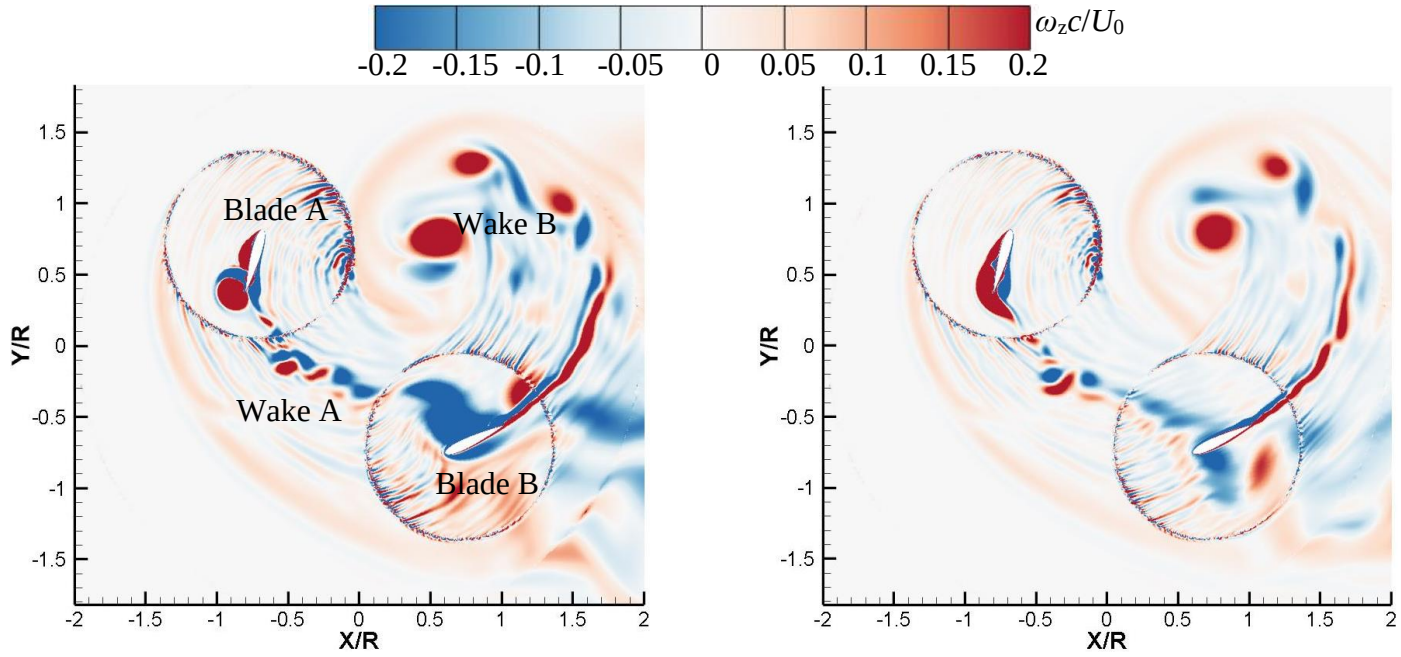

(a) (b)

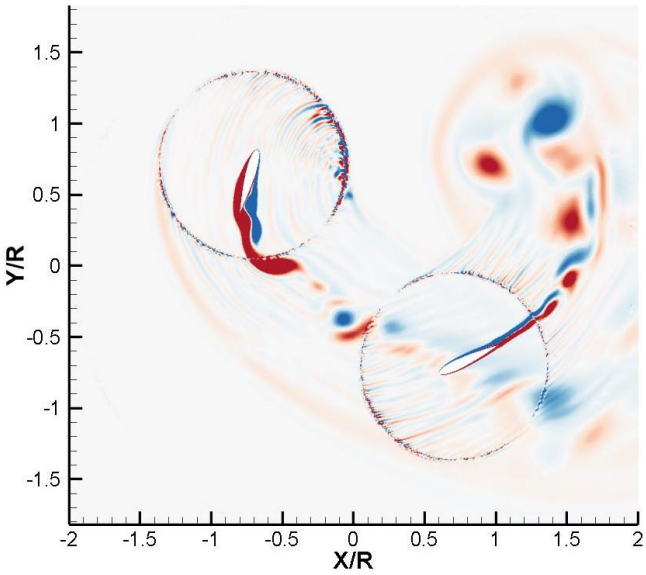

(c)

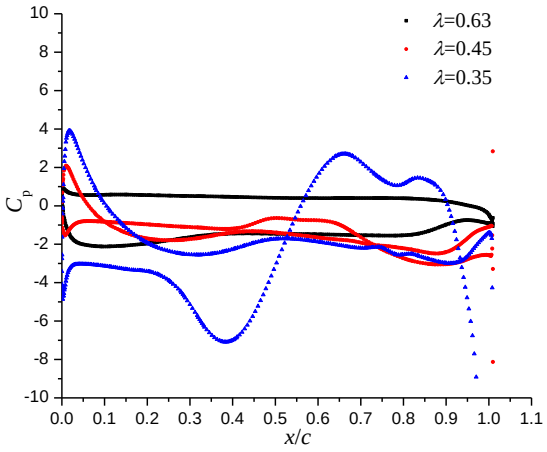

(d)

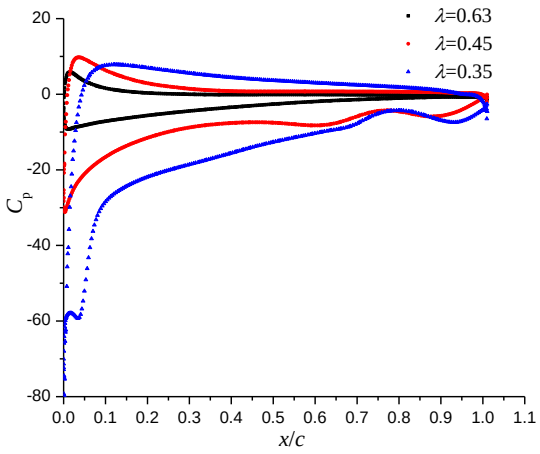

(e)

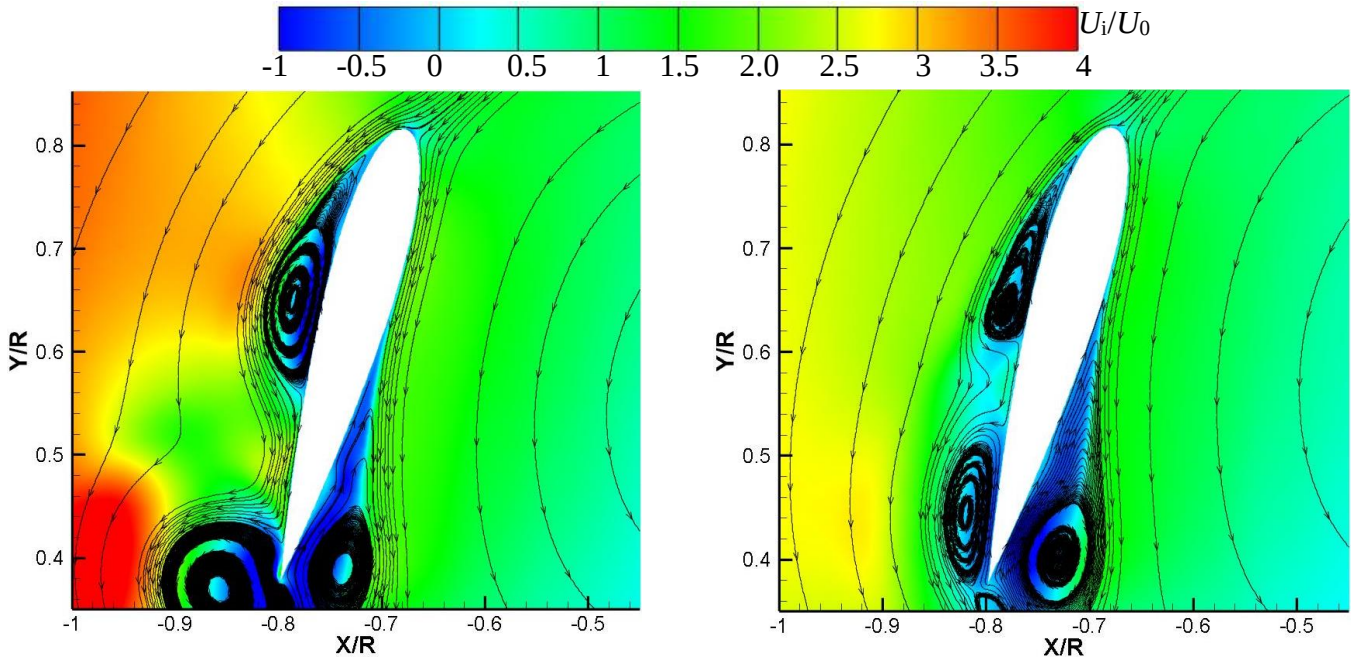

(f) (g)

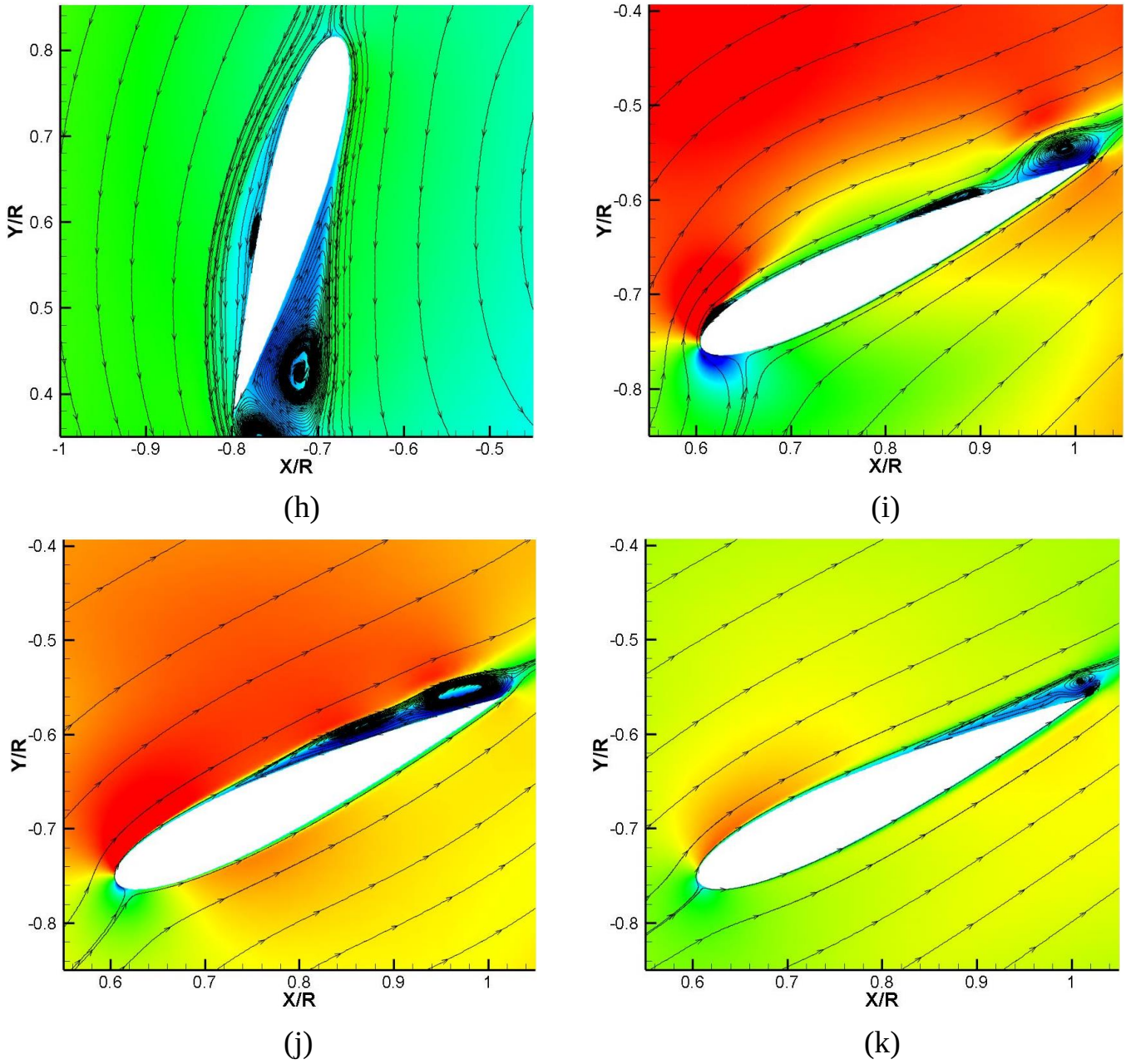

Fig.24 Flow structures for various λ at ψ=45°. (a) Global Flow structure at λ=0.35; (b) Global Flow structure at λ=0.45; (c) Global Flow structure at λ=0.63; (d) Pressure distribution of blade A; (e) Pressure distribution of blade B; (f) and (i) λ=0.35; (g) and (j) λ=0.45; (h) and (k) λ=0.63.

When the blade undergoes the retreating side, at ψ=135°, the lift coefficient of the rotating system has a negative peak, especially for the case at λ=0.35. The flow structures at this instant are presented in figure 25. Globally, it shows no obvious interaction, however, the flow is more complex at low λ. It detects that there are some small-scale vortices inside the boundary layer on the pressure side of blade A, leading to the pressure fluctuations in figure 25d. The blade A produces the downward lift, whose component is balanced by the drag component in the vertical direction, resulting in the lift of the rotating system close to zero, as shown in figure 23c. For blade B, the main feature is that the vortices appear on the suction side, especially at

λ=0.63, where the three vortex structures develop. The largest negative lift of the rotating system is obtained at λ=0.35, due to the downward lift generated by blade B and the large pressure difference (figure 25e).

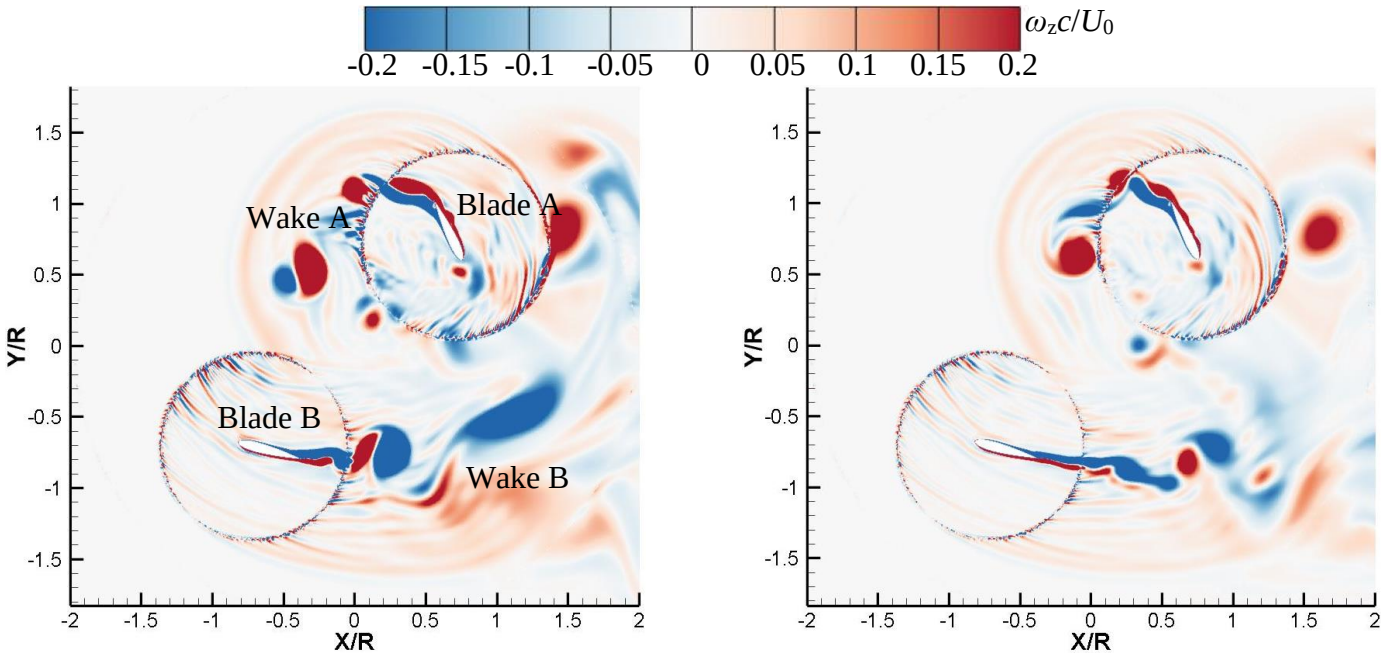

(a) (b)

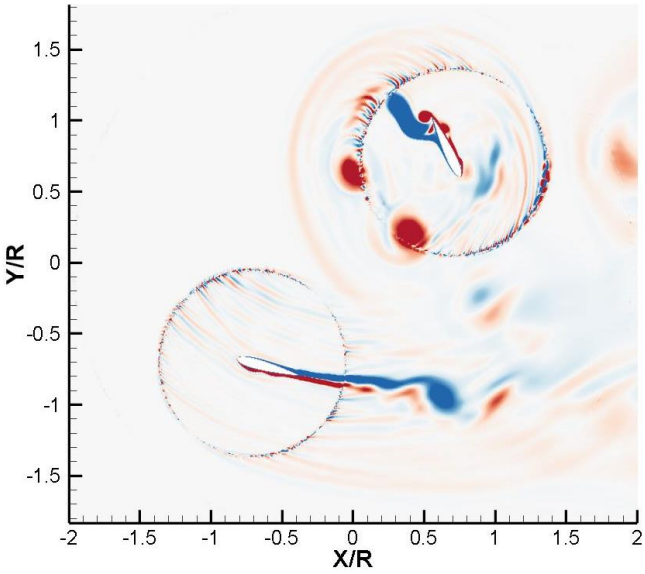

(c)

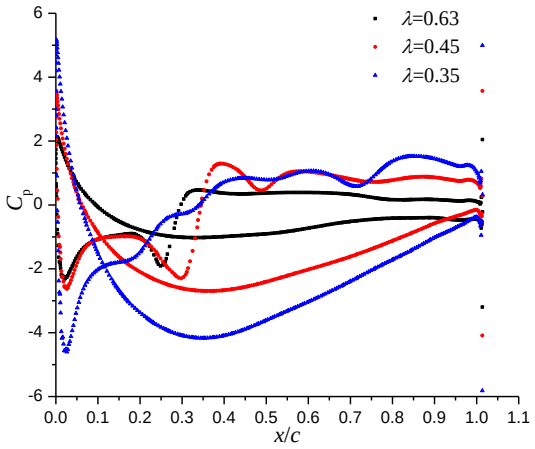
λ=0.63
λ=0.45
λ=0.35
C_p
x/c

(d)

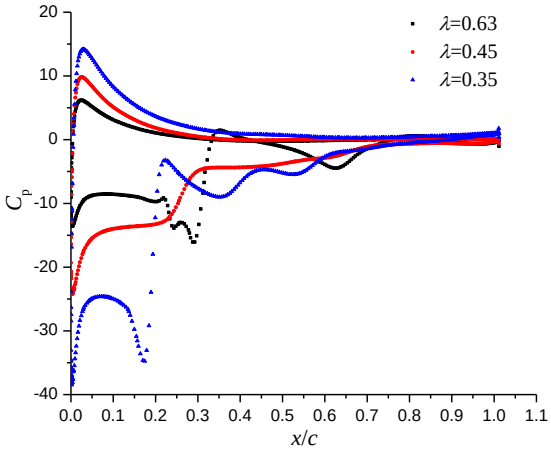
λ=0.63
λ=0.45
λ=0.35
C_p
x/c

(e)

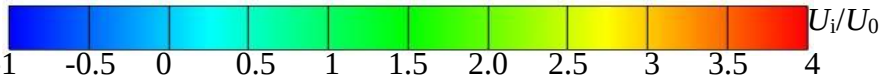
U_i/U_0
-1 -0.5 0 0.5 1 1.5 2.0 2.5 3 3.5 4

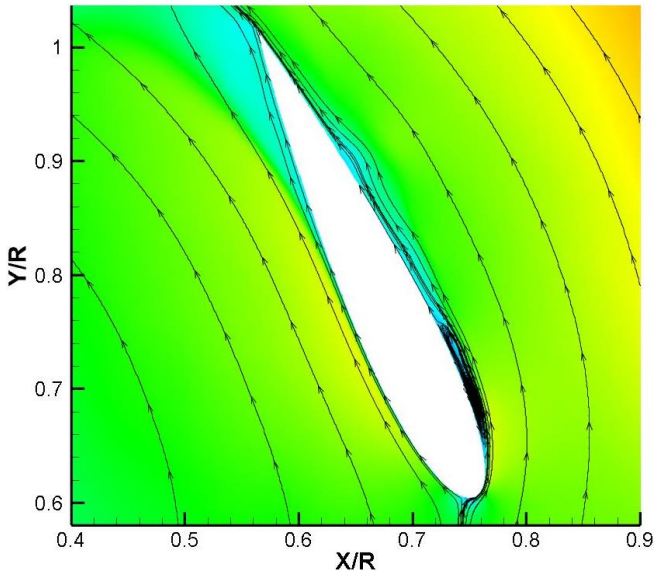
Y/R
X/R

(f)

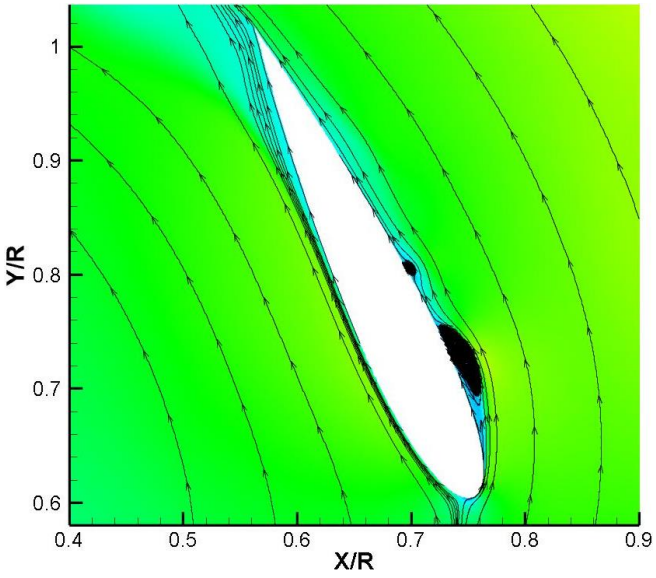
Y/R
X/R

(g)

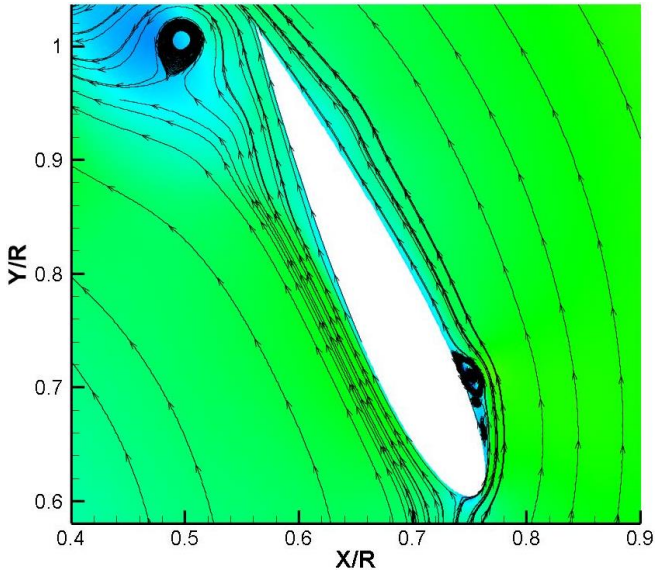
Y/R
X/R

(h)

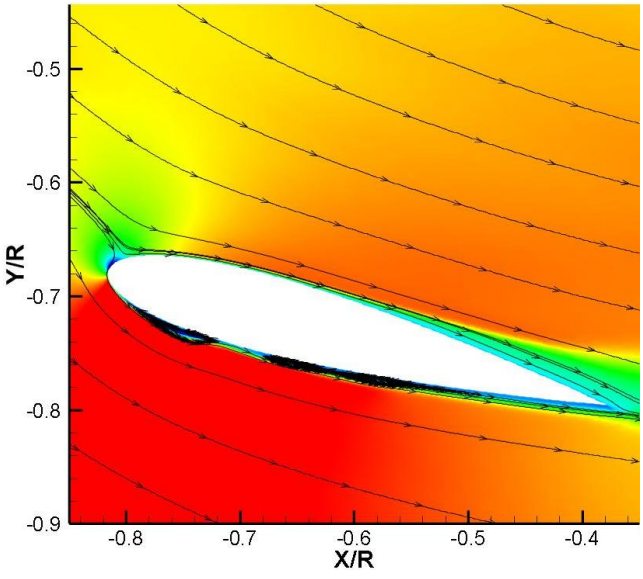
Y/R
X/R

(i)

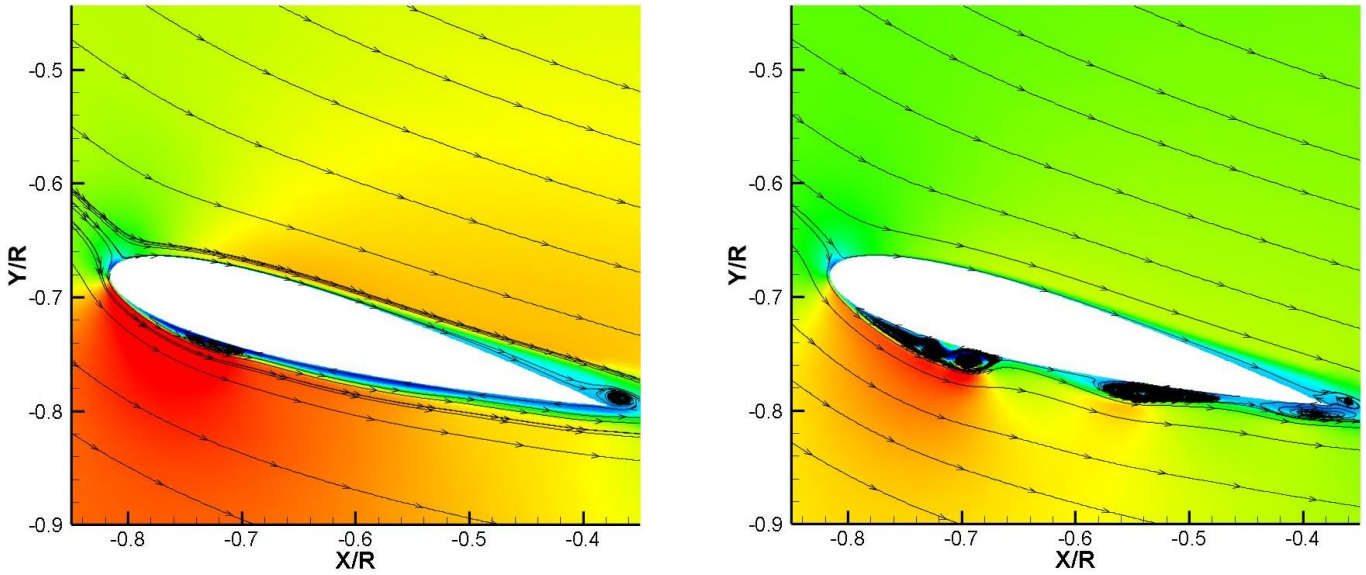

(g) (h)

Fig.25 Flow structures for various λ at ψ=135°. (a) Global Flow structure at λ=0.35; (b) Global Flow structure at λ=0.45; (c) Global Flow structure at λ=0.63; (d) Pressure distribution of blade A; (e) Pressure distribution of blade B; (f) and (i) λ=0.35; (g) and (j) λ=0.45; (h) and (k) λ=0.63.

Finally, the impact of λ on the propulsive force difference of the rotating system is clarified at ψ=12°, where it has a positive peak. At low λ, blade A is likely interacting with wake B, but this is not the case when λ increases. Moreover, at high λ, wake B has a strong interaction with itself because of the low rotation speed. When it comes to the single blade, the near-wall flow structure and blade loading are very different. The flow over blade A is relatively smooth and there is a flow separation only at the trailing edge on the suction side. However, due to the location of the stagnation point, the pressure on both two sides varies considerably according to λ. Because of the large blade loading at low λ, blade A can produce large upward lift, which is the main source of the large positive propulsive force of the rotating system. Then, on blade B, the flow is more complicated and many vortices are attached to the suction side. At low λ, the three-vortex-structure are obvious, nearly occupying the whole blade surface. With the increase of λ, the flow becomes relatively smooth and only a large-scale vortex appears on the suction side, which is attributed to the shift of the stagnation point towards the suction side. The existence of the vortex leads to a significant pressure drop, as shown in figure 26e, resulting in the large blade loading at low λ. The large downward lift creates a large positive propulsive force, which is beneficial to the large positive propulsive force of the rotating system, as shown in figure 23. Thus, the global propulsive force is determined by the two blades at this position.

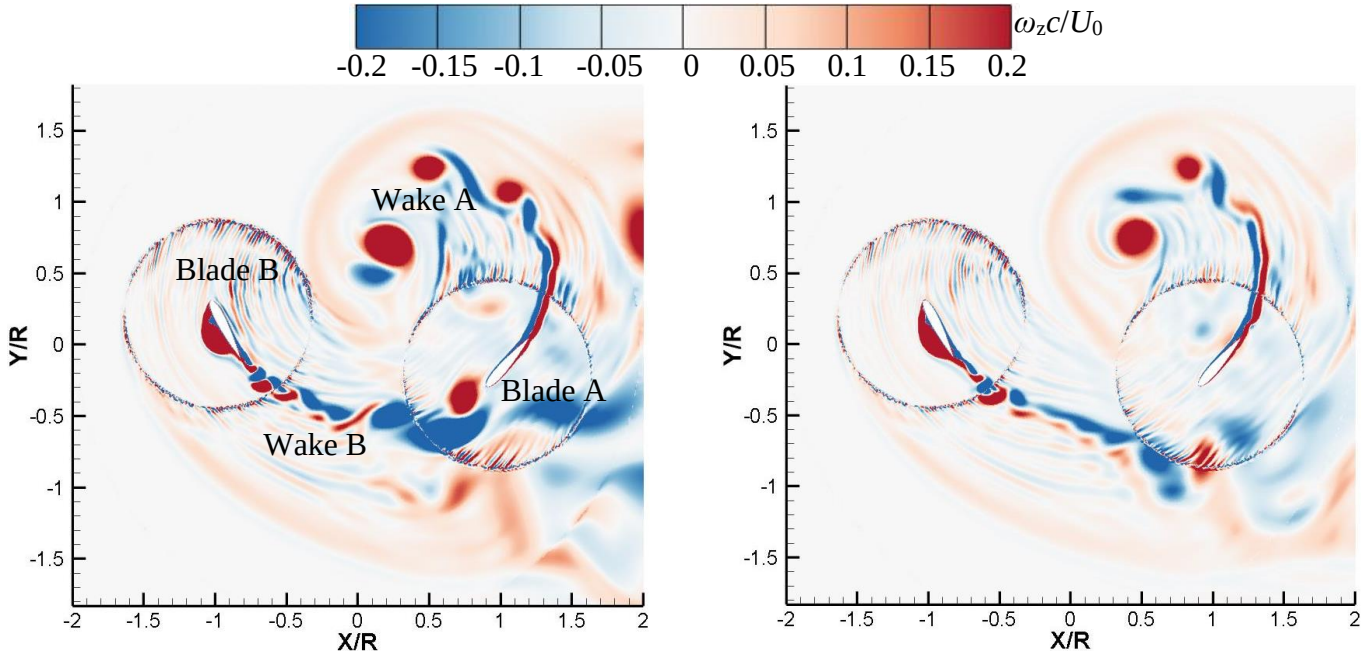
$\omega_z c/U_0$
-0.2 -0.15 -0.1 -0.05 0 0.05 0.1 0.15 0.2
Wake A
Blade B
Blade A
Wake B
Y/R
X/R

(a) (b)

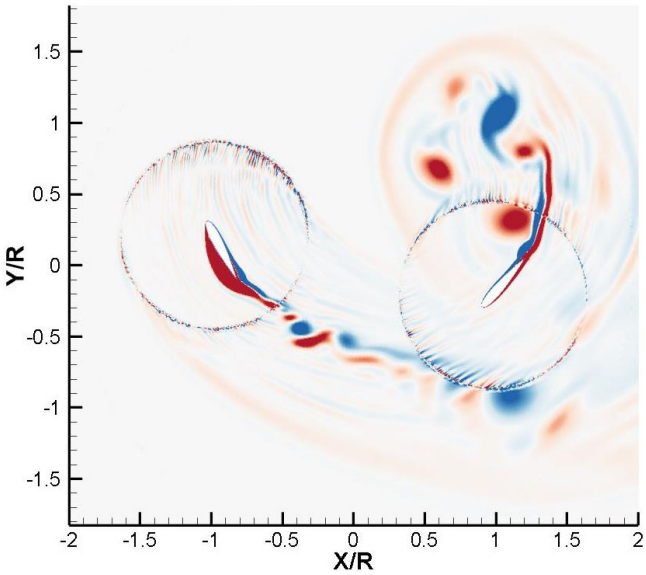
Y/R
X/R

(c)

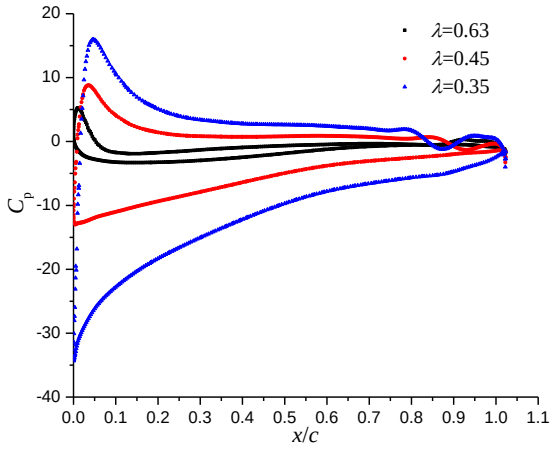
λ=0.63
λ=0.45
λ=0.35
C_p
x/c

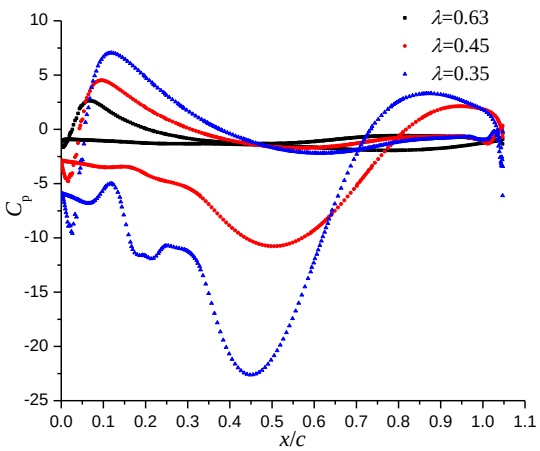
λ=0.63
λ=0.45
λ=0.35
C_p
x/c

(d) (e)

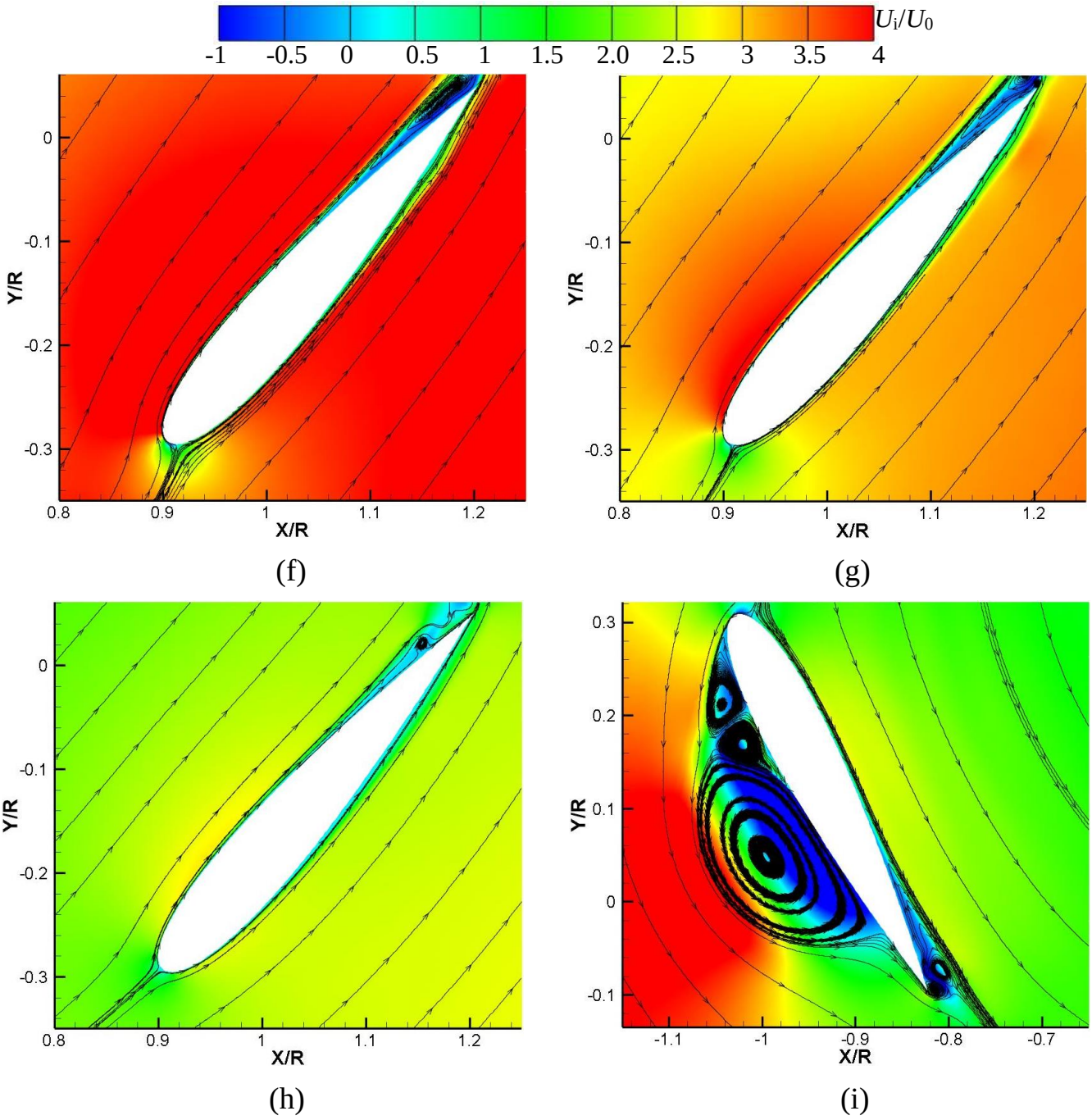
U_i/U_0
-1 -0.5 0 0.5 1 1.5 2.0 2.5 3 3.5 4
Y/R
X/R
0 -0.1 -0.2 -0.3
0.8 0.9 1 1.1 1.2
(f)
(g)
0.3 0.2 0.1 0 -0.1
-1.1 -1 -0.9 -0.8 -0.7
(h)
(i)

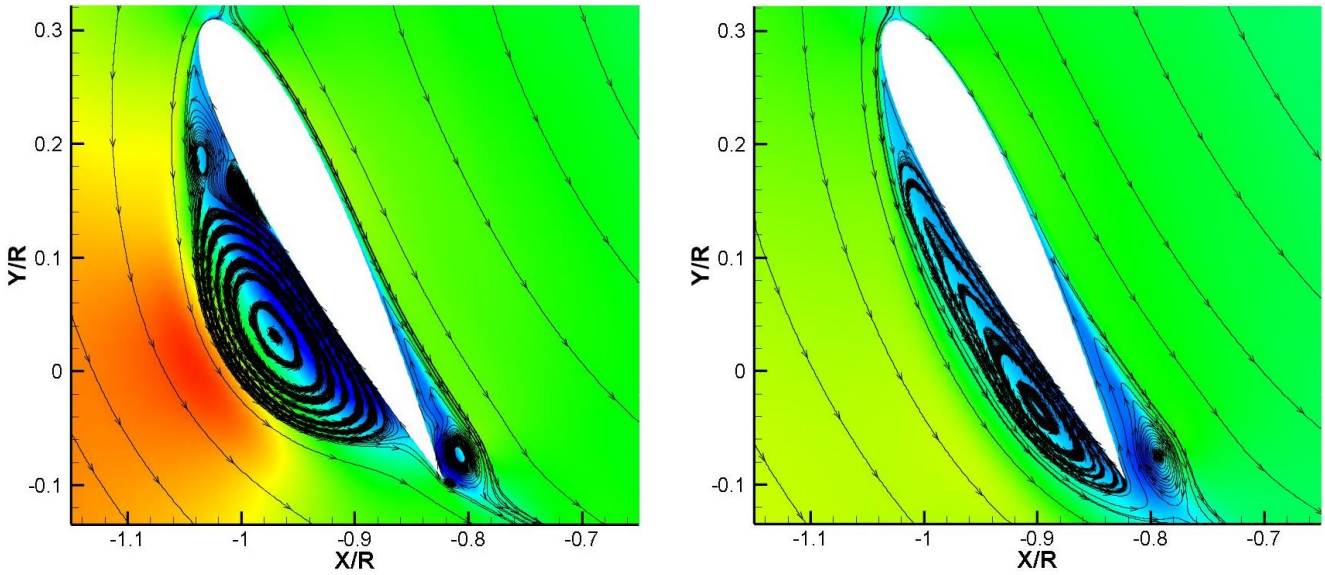

Fig.26 Flow structures for various λ at ψ=12°. (a) Global Flow structure at λ=0.35; (b) Global Flow structure at λ=0.45; (c) Global Flow structure at λ=0.63; (d) Pressure distribution of blade A; (e) Pressure distribution of blade B; (f) and (i) λ=0.35; (g) and (j) λ=0.45; (h) and (k) λ=0.63.

4. Concluding remarks

In this work, the SST $\gamma - \widetilde{Re}_{\theta t}$ transition model was applied to investigate the influence of the pitching kinematic and chord-to-radius ratio on the performance and flow structures of a two-bladed cycloidal rotor. The main conclusions are listed as follows:

(1) The asymmetrical pitching kinematic with a small positive mean pitch angle of 5° results in a highest efficiency of the cycloidal rotor, which results from the moderate propulsive force and low power. Conversely, although the symmetrical pitching with large amplitude and the asymmetrical pitching with large mean pitch angles generate a high propulsive force, the efficiency is quite low as a result of the complicated vortical flows leading to a higher power. Moreover, the asymmetrical pitching with a negative mean pitch angle produces the high lift coefficient with λ, but a decrease of the propulsive force coefficient.

(2) Generally, the performance of the single blade shows that the difference of the lift coefficient is mainly caused by blade B at advancing side, while it is induced by the two blades for the difference of the propulsive force coefficient. Near the airfoil surface, the flow structures are quite rich, including three vortex structures, roll-up vortices, flow separation vortex at the trailing edge, LSB, LEV and TEV, and the pattern of these vortices depends on the incidence importantly. When anlyzing the forces on the single blade, it is interesting that when the blade undergoes the left side of the advancing side (ψ=270°-360°), the lift direction is opposite for the asymmetrical pitching with negative mean pitch angles compared with that in other cases, as a

consequence of the stagnation point location caused by the different relative incidences.

(3) At given λ and *Re*, the cases with c/R=0.45 for different blade chord lengths achieve the best efficiency. Then, at large c/R, the global flow structure is more complicated and the performance is strongly impacted, due to the small distance between two adjacent blades.

(4) When it comes to the influence of *Re* and λ, it seems that the effect of *Re* on the performance is very small. However, at low *Re*, the propulsive force is significantly different from the one obtained at relatively high *Re*. The advance coefficient λ has a large impact on the flow structures and the global performance, especially at low λ, which is due to the large variation of the relative velocity induced by the change of the rotation speed. It seems that at high λ, the wake at right side of the retreating side (ψ=90°-180°) has a high risk in contacting with the blade, due to the low rotation speed. It is found that the cases with c/R=0.45 at various *Re* or λ obtain the best efficiency.

(5) Except for the near-wall flow, the stagnation point location associated with the boundary layer development is very critical to each blade loading. Changing the rotating speed only is more influential on the results, compared with the case by modifying the inlet velocity and rotation speed simultaneously, which is the main reason why the effect of λ is more obvious than *Re*.

Acknowledgement

The authors would like to show gratitude to China Scholarship Council (CSC) for the financial support. The authors acknowledge Advanced Research Computing at Virginia Tech for providing computational resources and technical support that have contributed to the results reported within this paper.

Author declarations

The authors have no conflicts to disclose.

Data availability

The data that support the findings of this study are available from the corresponding author upon reasonable request.

References

[1] Lind, A. H., Jarugumilli, T., Benedict, M., Lakshminarayan, V. K., Jones, A. R., & Chopra, I. (2014). Flow field studies on a micro-air-vehicle-scale cycloidal rotor in forward flight. *Experiments in Fluids*, *55*(12), 1-17.

[2] Benedict, M., Ramasamy, M., & Chopra, I. (2010). Improving the aerodynamic performance of micro-air-vehicle-scale cycloidal rotor: an experimental approach. *Journal of Aircraft*, *47*(4), 1117-1125.
[3] Jarugumilli, T., Benedict, M., & Chopra, I. (2011). Experimental optimization and performance analysis of a MAV scale cycloidal rotor. In *49th AIAA Aerospace Sciences Meeting Including the New Horizons Forum and Aerospace Exposition*, 4-7 January, Orlando, Florida, 821 (1-11).
[4] Benedict, M., Jarugumilli, T., Lakshminarayan, V., & Chopra, I. (2014). Effect of flow curvature on forward flight performance of a micro-air-vehicle-scale cycloidal-rotor. *AIAA Journal*, *52*(6), 1159-1169.
[5] Chen, B., Su, S., Viola, I. M., & Greated, C. A. (2018). Numerical investigation of vertical-axis tidal turbines with sinusoidal pitching blades. *Ocean Engineering*, *155*, 75-87.
[6] Roesler, B. T., Kawamura, M. L., Miller, E., Wilson, M., Brink-Roby, J., Clemmenson, E., Keller, M., & Epps, B. P. (2016). Experimental performance of a novel trochoidal propeller. *Journal of Ship Research*, *60*(1), 48-60.
[7] Benedict, M., Jarugumilli, T., & Chopra, I. (2013). Effect of rotor geometry and blade kinematics on cycloidal rotor hover performance. *Journal of Aircraft*, *50*(5), 1340-1352.
[8] Walther, C. M., Saemi, F., Benedict, M., & Lakshminarayan, V. (2019). Symmetric versus asymmetric pitching of a cycloidal rotor blade at ultra-low Reynolds numbers. *Journal of Aircraft*, *56*(3), 1179-1199.
[9] Benedict, M., Jarugumilli, T., & Chopra, I. (2016). Effects of asymmetric blade-pitching kinematics on forward-flight performance of a micro-air-vehicle-scale cycloidal-rotor. *Journal of Aircraft*, *53*(5), 1568-1573.
[10] Paillard, B., Astolfi, J. A., & Hauville, F. (2015). URANSE simulation of an active variable-pitch cross-flow Darrieus tidal turbine: Sinusoidal pitch function investigation. *International Journal of Marine Energy*, *11*, 9-26.
[11] Chen, B., Nagata, S., Murakami, T., & Ning, D. (2019). Improvement of sinusoidal pitch for vertical-axis hydrokinetic turbines and influence of rotational inertia. *Ocean Engineering*, *179*, 273-284.
[12] Hu, Y., & Zhang, H. L. (2015). The effect of the blade chord length on the aerodynamics of the MAV scale cycloidal propeller under hovering status. In *45th AIAA fluid dynamics conference*, 22-26 June, Dallas, TX, 3070 (1-13).
[13] Xisto, C. M., Páscoa, J. C., & Trancossi, M. (2016). Geometrical parameters influencing the aerodynamic efficiency of a small-scale self-pitch high-solidity VAWT. *Journal of Solar Energy Engineering*, *138*(3), 031006 (1-8).

[14] Menter, F. R., Kuntz, M., & Langtry, R. (2003). Ten years of industrial experience with the SST turbulence model. *Turbulence, Heat and Mass Transfer*, *4*(1), 625-632.
[15] Heschl, C., Inthavong, K., Sanz, W., & Tu, J. (2013). Evaluation and improvements of RANS turbulence models for linear diffuser flows. *Computers & Fluids*, *71*, 272-282.
[16] Menter, F. R., Langtry, R., & Völker, S. (2006). Transition modelling for general purpose CFD codes. *Flow, Turbulence and Combustion*, *77*(1-4), 277-303.
[17] Menter, F. R., Langtry, R. B., Likki, S. R., Suzen, Y. B., Huang, P. G., & Völker, S. (2006). A correlation-based transition model using local variables—part I: model formulation. *Journal of Turbomachinery*, *128*, 413-422.
[18] Langtry, R. B., Menter, F. R., Likki, S. R., Suzen, Y. B., Huang, P. G., & Völker, S. (2006). A correlation-based transition model using local variables—part II: test cases and industrial applications. *Journal of Turbomachinery*, *128*, 423-434.
[19] Lanzafame, R., Mauro, S., & Messina, M. (2013). Wind turbine CFD modeling using a correlation-based transitional model. *Renewable Energy*, *52*, 31-39.
[20] Baltazar, J., Rijpkema, D., & de Campos, J. F. (2018). On the use of the $\gamma - \widetilde{Re}_{\theta t}$ transition model for the prediction of the propeller performance at model-scale. *Ocean Engineering*, *170*, 6-19.
[21] Shi, L., Bayeul-Lainé, A. C., & Coutier-Delghosa, O. (2022). Numerical investigations on unsteady vortical flows and transition over a cycloidal rotor at low Reynolds number. Submitted.
[22] Choudhuri, P. G., & Knight, D. D. (1996). Effects of compressibility, pitch rate, and Reynolds number on unsteady incipient leading-edge boundary layer separation over a pitching airfoil. *Journal of Fluid Mechanics*, *308*, 195-217.
[23] Tseng, C. C., & Hu, H. A. (2016). Flow dynamics of a pitching foil by Eulerian and Lagrangian viewpoints. *AIAA Journal*, *54*(2), 712-727.
[24] Negi, P. S., Vinuesa, R., Hanifi, A., Schlatter, P., & Henningson, D. S. (2018). Unsteady aerodynamic effects in small-amplitude pitch oscillations of an airfoil. *International Journal of Heat and Fluid Flow*, *71*, 378-391.
[25] Kim, D. H., Chang, J. W., & Sohn, M. H. (2017). Unsteady aerodynamic characteristics depending on reduced frequency for a pitching NACA0012 airfoil at $Re_c = 2.3 \times 10^4$. *International Journal of Aeronautical and Space Sciences*, *18*(1), 8-16.